Mixed-Potential Integral Equation Technique for Hybrid Microstrip-Slotline Multi-layered Circuits with Horizontal and Vertical Shielding Walls

Marlize Schoeman

Thesis presented in partial fulfillment of the requirements for the degree of Master of Engineering at the University of Stellenbosch.

Supervisor: Prof. P. Meyer

December 2003

Declaration

I, the undersigned, hereby declare that the work contained in this thesis is my own original work and that I have not previously in its entirety or in part submitted it at any university for a degree.

M. Schoeman _____ Date _____

Abstract

Keywords—Method of Moments (MoM), Stratified Media, Green's Functions.

A complete mixed-potential integral equation formulation for the analysis of arbitrarily shaped scatterers in a planarly layered medium is presented. The integral equation is able to solve for simultaneous electric and magnetic surface currents using a Method of Moments (MoM) procedure.

The MoM formulation which was developed uses vector-valued basis functions defined over a triangular mesh and are used to model electric currents on conducting scatterers and magnetic currents on slotline structures. The Green's functions employed in the analysis were developed for a stratified medium using a Sommerfeld plane wave formulation.

The scheme used for filling the method of moments matrix was designed to simultaneously solve multiple problems that are stacked and separated by an infinite conducting ground plane. The filling algorithm also efficiently packs partially symmetric matrices, which are present when solving problems that support a combination of electric and magnetic currents.

Several examples are presented to illustrate and validate the analysis method. Numerical predictions of the scattering parameters (both magnitude and phase) show good correspondence with results from literature and measured data.

Opsomming

Sleutelwoorde—Metode van Momente (MoM), Gelaagde media, Green's Funksies.

'n Volledige gemengde potensiaal integraalvergelyking formulering vir die analise van stralers van arbitrêre vorm binne gelaagde strukture word aangebied. Die integraalvergelyking kan gelyktydige elektriese en magnetiese oppervlakstrome oplos deur die Metode van Momente (MoM) te gebruik.

Die MoM formulering gebruik vektor basis funksies wat oor 'n driehoekige diskretisering gedefinieer word om elektriese strome op geleidende stralers en magnetiese strome op gleuflyn strukture te modelleer. Die Green's funksies wat in die analise gebruik word, is ontwikkel vir gelaagde media deur gebruik te maak van Sommerfeld se platvlakgolf formulering.

Die metode wat gebruik word om the moment matriks te vul, is ontwerp om meervoudige gestapelde probleme wat deur oneindig geleidende grondvlakke geskei word, gelyktydig op te los. Gedeeltelik simmetriese matrikse word ook effektief gevul. Hierdie matrikse kom voor wanneer probleme 'n kombinasie van elektriese en magnetiese strome ondersteun.

Verskeie voorbeelde word gebruik om die analise metode te verifieer. Numeriese voorspellings van strooiparameters (beide grootte en hoek) vergelyk baie goed met resultate en gemete data wat in die literatuur gevind is.

Acknowledgements

I would like to express my sincere gratitude to everyone who has contributed to this thesis in any way. In particular, I would like to thank my promoter, Prof. P. Meyer, for his advice, guidance and moral support, and the financial support without which this work would not have been possible.

I also wish to thank Dr. J.J. van Tonder for useful comments and suggestions.

The financial assistance of the National Research Foundation (NRF) towards this research is hereby acknowledged. Opinions expressed and conclusions arrived at, are those of the author and are not necessarily to be attributed to the NRF.

To my friends, I express thanks for their patience, support and encouragement during times of difficulty.

Finally, I want to thank my heavenly Father who has given me ability and perseverance to fulfill this task.

Contents

List of Figures

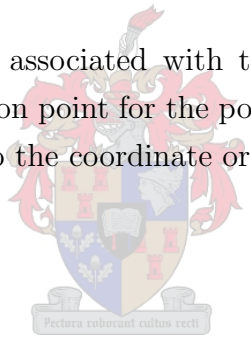

List of Tables

Chapter 1

Introduction

In the past several years, designers of microwave integrated circuits have come to depend heavily on computer-aided techniques to reduce design time and improve performance. Accurate full-wave electromagnetic models are now often required to account for effects such as dispersion, surface waves, radiation and coupling. Three numerical techniques, applicable to general electromagnetic problems, have attracted considerable interest: the Method of Moments (MoM) and its variants [1], the Finite Element Method (FEM) [2], and the Finite Difference Time Domain (FDTD) method [3]. Among these approaches, the MoM is widely regarded as one of the most popular techniques for the solution of the mixed-potential integral equation (MPIE) for printed geometries in planarly layered media [4], [5], [6].

While some Method of Moments procedures address specific geometries such as open circuits and gaps [7], others are intended for application to arbitrary configurations. In the latter category, the literature offers techniques based on MoM where the current on a conductor is expanded over rectangular subdomains in an approximate solution to the electric-field integral equation (EFIE) [8], [9] or the mixed-potential integral equation (MPIE) [10].

In 1982, Rao, Wilton and Glisson [11] introduced triangular subdomain basis functions to analyse general 3D structures in a homogeneous medium. These are widely used where the effect of the environment can be neglected, but does exclude many problems of practical interest where the proximity of the earth should be taken into account. This technique was extended in 1985 to inhomogeneous microstrip configurations to compute the surface current distribution and S-parameters of microstrip discontinuities [12], [13]. The triangular discretisation offers several advantages over rectangular subdomains—the triangles easily conform to any arbitrary geometry and offer greater flexibility in the use

of nonuniform discretisations.

The mixed-potential form of the electric field integral equation is favoured over the electric and magnetic field integral equation formulations because it requires only the potential forms of the Green's functions, which are less singular in comparison with the components of the electric field Green's dyadic. Also, the Sommerfeld integrals it requires converge faster than those present in any other form of the EFIE [6].

The pioneer study on electromagnetic wave propagation in stratified media was by Sommerfeld, who investigated the radiowave propagation above a lossy ground as early as 1909 [14]. Later, several authors extended these theories to arbitrary stratified media and applied this model to practical microstrip structures [15], [16]. An important advance in increasing analysis capabilities, was presented in 1990. The new procedure was able to analyse models consisting of predominantly planar structures and, the objects were permitted to penetrate one or more of the interfaces between dielectric layers [6], [17]. Michalski pointed out that the success of previous efforts is attributed to the fact that the structures could only support either horizontal or vertical components of current.

Circuits containing slots and conductors constitute the most general type of planar structures. Numerous investigators have presented approximate analytical techniques to characterise these structures with application to circuit elements [18], [19] and [20]. Numerical techniques supporting only electric currents, require that infinite ground planes be modelled as finite size conductors. Meshing of these ground planes requires unnecessary computational effort and memory. In comparison, analysis procedures that mesh slotline interfaces were introduced. As an example, a full-wave space-domain analysis of aperture coupled shielded microstrip lines was reported in [21]. The approach developed Green's functions in the form of waveguide modes. More recently, [22] contributed to the application of mixed meshes in MoM modelling. Both rectangular and triangular basis functions were employed to model electric and magnetic surface currents specifically applicable to microstrip-slotline multi-layered circuits. No provision is made for vertical conductors.

In this thesis a full-wave analysis of arbitrary objects embedded in multi-layered circuits is presented. The mixed-potential integral equation formulation for infinite open planar structures is extended to account for the effects of horizontal and vertical shielding structures and makes provision for simultaneous electric and magnetic currents. Electric surface currents are introduced on the surface of conducting apertures and magnetic surface currents are introduced at slotline interfaces. This approach eliminates the meshing of ground planes altogether. Vertical shielding walls are meshed and connected to horizontal conducting materials through half and multiple basis functions. A triangular mesh is used to model unknown currents. Finally, the formulation is tested and verified using

a diverse set of problems. The results obtained compare very well with measured and computed data available in the literature.

1.1 Overview of the thesis

The aim of this thesis is to develop a Method of Moments formulation that can solve for simultaneous electric and magnetic currents in multi-layered geometries.

Chapter 2 develops the Green's functions of a dipole in planarly layered media. The formulation presents a summary of work done by Chew [23], Van Tonder [24] and Michalski [6]. In Section 2.7 an analytic approach to evaluating the *curl* of the vector potential Green's functions is presented.

Chapter 3 describes the numerical evaluation of the Sommerfeld-type Green's functions developed in Chapter 2. The existence of numerical difficulties in the integrand is discussed and the proposed solution algorithms are described. Section 3.2 presents Mosig's Method of Averages which is used to evaluate the tail integrals, and Section 3.3 presents a technique to extract static parts from the integral kernels to increase convergence.

The Method of Moments formulation solving for a combination of electric and magnetic currents is developed in Chapter 4. Section 4.1 discusses boundary conditions and the equivalence principle utilised to solve the electric and magnetic fields as a function of the vector and scalar potentials, which are intermediate functions directly related to the sources. A summary of the work done by Rao, Wilton and Glisson [11], on the moment method formulation using a triangular discretisation in free space, is included in Section 4.2. Also presented in this section is a definition of additional half and extra basis functions. In Section 4.4 a partitioned matrix equation was defined. This system of simultaneous linear equations is solved for the unknown electric and magnetic current distributions. Finally, Section 4.7 presents the technique used for extracting scattering parameters.

The proposed formulation is verified in Chapter 5 by applying the method to examples of varying complexity, each aimed at the evaluation of a different numerical property. Results are compared with measured and computed results available in the literature.

Finally, Chapter 6 ends with general conclusions. Section 6.1 contains a critical evaluation of the code developed with recommendations to future development.

Chapter 2

Green's Functions of a Dipole in Layered Media

In this Chapter the Green's functions of a dipole embedded in a multi-layered medium are considered. Using the formulation of Chew [23] and van Tonder [24] and [25], the Green's functions for the vector and scalar potentials are developed in the frequency domain. The formulation is presented for an electric dipole source, the principle of duality is discussed and appropriate results for a magnetic source are listed. The Green's functions will be used in the method of moments formulation of Chapter 4 to compute surface current densities and scattering parameters. Throughout, familiarity with Chew [23] will be assumed.

2.1 Statement of the Problem

Consider the geometry shown in Fig. 2.1. The medium consists of N dielectric layers separated by $N-1$ planar interfaces parallel to the xy plane of a Cartesian coordinate system. Each layer extends to infinity in the transverse directions and consists of an isotropic, homogeneous material. The medium of the i^{th} layer is characterised by permeability μ_i and permittivity ϵ_i, which may be complex if the medium is lossy. Regions 1 and N are half-spaces and extend to $\pm\infty$ in the z direction. An electric impedance wall may be introduced at any interface $z = -d_1$ to $z = -d_{N-1}$.

The source is sinusoidally time-varying. It is located in Region m at $(x, y, z) = (0, 0, z')$ and can be an electric or magnetic dipole directed horizontally along the x-axis, or vertically along the z-axis. The observation point is inside the n^{th} layer.

The analysis will be presented by first solving for the fields of an electric dipole in free

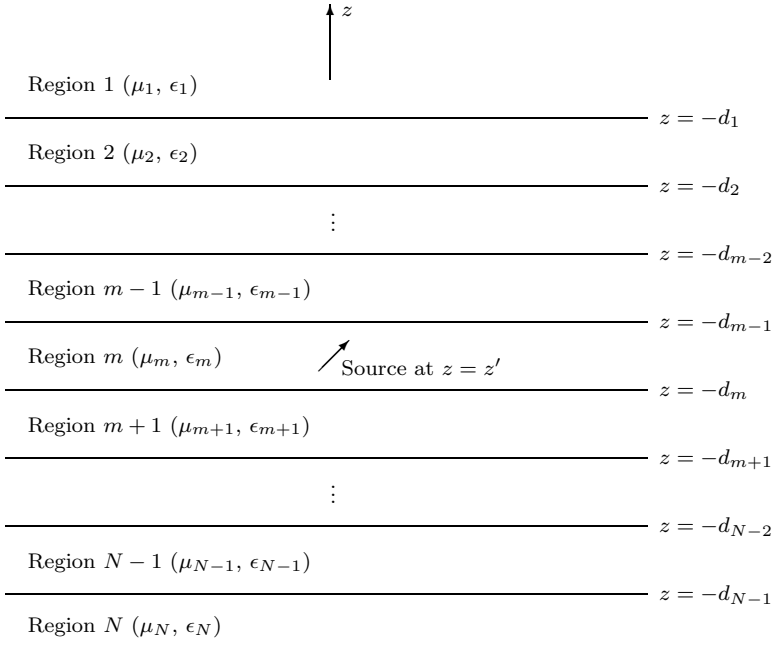

Figure 2.1: Multi-layered medium with Hertzian dipole point source in the m^{th} layer.

space. This formulation will be extended to calculate the fields of a dipole embedded in a layered medium by matching boundary conditions across the discontinuities at the planar interfaces. Using Sommerfeld's identity, the free-space solution is transformed to a summation of TM- and TE-type plane waves in the z direction. These are characteristic of stratified media and present a convenient form to easily match boundary conditions relating incident and reflected plane waves at the layer interfaces. Finally, the Green's functions for the normal components of field are related to the Green's functions for the vector and scalar potentials. These relations will be derived and interpreted using a spectral domain approach.

2.2 Electric Dipole Fields in Free Space

The fields in a homogeneous, isotropic and unbounded medium due to a point current source directed in the $\hat{\boldsymbol{\alpha}}$ direction, can be derived using a dyadic Green's function approach.

Maxwell's equations for the sinusoidally time-harmonic case, with the fictitious magnetic

current density $\mathbf{M}$ assumed to be zero, can be written as[1]

$$\begin{aligned} \nabla \times \mathbf{E} &= -j\omega\mu\mathbf{H} \\ \nabla \times \mathbf{H} &= j\omega\epsilon\mathbf{E} + \mathbf{J}. \end{aligned} \tag{2.1}$$

The general form of the vector wave equation following from Eqn. 2.1, is

$$\nabla \times \nabla \times \mathbf{E}(\mathbf{r}) - k^2\mathbf{E}(\mathbf{r}) = -j\omega\mu\mathbf{J}(\mathbf{r}). \tag{2.2}$$

By using the identity $\nabla \times \nabla \times \mathbf{E} = -\nabla^2\mathbf{E} + \nabla\nabla \cdot \mathbf{E}$ and $\nabla \cdot \mathbf{E} = \rho/\epsilon = -\nabla \cdot \mathbf{J}/j\omega\epsilon$, which follows from the continuity equation, Eqn. 2.2 can be written as

$$(\nabla^2 + k^2)\mathbf{E}(\mathbf{r}) = j\omega\mu\Big(\bar{\bar{\mathbf{I}}} + \frac{\nabla\nabla}{k^2}\Big) \cdot \mathbf{J}(\mathbf{r}) \tag{2.3}$$

where $\bar{\bar{\mathbf{I}}}$ is the unit dyadic. Note that there are three scalar wave equations embedded in the above vector equation.

The Green's function of a wave equation represents the response of a physical system in space due to a point source excitation. Using the Green's function, the linearity of the wave equation, and the principle of superposition, the solution due to a general source can be found. Consequently, to obtain the solution to Eqn. 2.3, we first seek the Green's function that satisfies the scalar wave equation

$$(\nabla^2 + k^2)g(\mathbf{r}, \mathbf{r}') = -\delta(\mathbf{r} - \mathbf{r}'). \tag{2.4}$$

Eqn. 2.4 alone is insufficient to determine the Green's function uniquely, and therefore $g(\mathbf{r}, \mathbf{r}')$ must satisfy additional radiation and boundary conditions. Ishimaru [26] presents a complete analysis on finding the closed form solution for unbounded space to Eqn. 2.4,

$$g(\mathbf{r}, \mathbf{r}') = g(\mathbf{r} - \mathbf{r}') = \frac{e^{-jk|\mathbf{r}-\mathbf{r}'|}}{4\pi|\mathbf{r} - \mathbf{r}'|}. \tag{2.5}$$

Eqn. 2.5 is known as the free-space Green's function for homogeneous media. Notice that $g(\mathbf{r}, \mathbf{r}')$ depends only on $|\mathbf{r} - \mathbf{r}'|$, implying translational invariance.

To find the dyadic Green's function for the vector wave equation of Eqn. 2.3, an integral linear superposition of the solution of Eqn. 2.4 is used. Consequently,

$$\mathbf{E}(\mathbf{r}) = -j\omega\mu \int_V g(\mathbf{r} - \mathbf{r}')\Big(\bar{\bar{\mathbf{I}}} + \frac{\nabla'\nabla'}{k^2}\Big) \cdot \mathbf{J}(\mathbf{r}')dv'. \tag{2.6}$$

[1] A harmonic time convention of $e^{j\omega t}$ is assumed and suppressed throughout the text. This is the same as van Tonder [24], while Chew [23] uses the $e^{-i\omega t}$ time convention. The one can be deduced from the other by replacing $\omega \leftrightarrow -\omega$ in all equations.

Alternatively, using vector identities and reciprocity, Eqn. 2.6 can be written as

$$\mathbf{E}(\mathbf{r}) = -j\omega\mu \int_V \bar{\bar{\mathbf{G}}}_{EJ}(\mathbf{r}, \mathbf{r}') \cdot \mathbf{J}(\mathbf{r}')dv' \tag{2.7}$$

where

$$\bar{\bar{\mathbf{G}}}_{EJ}(\mathbf{r}, \mathbf{r}') = \left(\bar{\bar{\mathbf{I}}} + \frac{\nabla\nabla}{k^2}\right)\frac{e^{-jk|\mathbf{r}-\mathbf{r}'|}}{4\pi|\mathbf{r}-\mathbf{r}'|}. \tag{2.8}$$

For an electric dipole source at the origin and directed in the $\hat{\boldsymbol{\alpha}}$ direction, $\mathbf{J}(\mathbf{r}) = \hat{\boldsymbol{\alpha}} I\ell\delta(\mathbf{r})$, and the electric field is given by

$$\mathbf{E}(\mathbf{r}) = -j\omega\mu\left(\bar{\bar{\mathbf{I}}} + \frac{\nabla\nabla}{k^2}\right) \cdot \hat{\boldsymbol{\alpha}} I\ell \frac{e^{-jkr}}{4\pi r} \tag{2.9}$$

with $I\ell$ the current moment and $k = \omega\sqrt{\mu\epsilon}$ the wave number of the homogeneous medium. Furthermore, from Maxwell's equation $\nabla \times \mathbf{E} = -j\omega\mu\mathbf{H}$, the magnetic field due to a Hertzian dipole is

$$\mathbf{H}(\mathbf{r}) = \nabla \times \hat{\boldsymbol{\alpha}} I\ell \frac{e^{-jkr}}{4\pi r}. \tag{2.10}$$

2.3 Electric Dipole Fields in a Layered Medium

Coherent, time-harmonic electromagnetic waves propagating in a planarly layered, isotropic medium can be decomposed into transverse magnetic (TM) and transverse electric (TE) waves. The problem of an electric Hertzian source embedded in a layered medium is equivalent to a one-dimensional problem and the propagation of the TM and TE waves are completely decoupled from each other—they are only coupled at the source.

A unique solution is found by first solving the problem for each piecewise constant region and then matching boundary conditions across the discontinuities at the interfaces. These conditions require that $\hat{\mathbf{n}} \times \mathbf{E}$ and $\hat{\mathbf{n}} \times \mathbf{H}$ be continuous in a source free region.

Using the Sommerfeld identity

$$\int_C J_0(k_\rho\rho)\frac{k_\rho}{jk_z}e^{-jk_z|z|}dk_\rho = \frac{e^{-jkr}}{r}, \tag{2.11}$$

where C is a path from 0 to ∞, and changing the order of integration and differentiation, Eqns. 2.9 and 2.10 can be rewritten as

$$\mathbf{E}(\mathbf{r}) = -j\omega\mu\frac{I\ell}{4\pi}\int_0^\infty \left(\bar{\bar{\mathbf{I}}} + \frac{\nabla\nabla}{k^2}\right) \cdot \hat{\boldsymbol{\alpha}} J_0(k_\rho\rho)\frac{k_\rho}{jk_z}e^{-jk_z|z|}dk_\rho \tag{2.12}$$

and

$$\mathbf{H}(\mathbf{r}) = \frac{I\ell}{4\pi}\int_0^\infty \nabla \times \hat{\boldsymbol{\alpha}} J_0(k_\rho\rho)\frac{k_\rho}{jk_z}e^{-jk_z|z|}dk_\rho. \tag{2.13}$$

By realising that the field Green's function is the field response for a point source, Eqns. 2.12 and 2.13 may be directly interpreted as the Green's functions for the electric and magnetic fields respectively. The Green's functions describing the normal components of field E_z and H_z are evaluated for individually x and z directed sources. These are sufficient to calculate all transverse field components.

For a horizontal electric dipole (HED) located in medium m and pointing in the x direction, $\hat{\boldsymbol{\alpha}} = \hat{\mathbf{x}}$. Hence, the Green's functions characterising the orthogonal wave components in medium n are

$$\begin{aligned} G^{zx}_{EJ,n} &= \frac{I\ell}{4\pi}\frac{j}{\omega\epsilon_n}\cos\phi\int_0^\infty J_1(k_\rho\rho)k_\rho^2 F^{HED}_{E_z}dk_\rho \\ G^{zx}_{HJ,n} &= \frac{I\ell}{4\pi}\sin\phi\int_0^\infty J_1(k_\rho\rho)\frac{k_\rho^2}{jk_{mz}}F^{HED}_{H_z}\frac{\mu_m}{\mu_n}dk_\rho. \end{aligned} \tag{2.14}$$

In the notation for the Green's function G, the subscripts indicate the field (**E** or **H**) due to a specific source type (**J** or **M**). The two superscripts give the corresponding component of the Green's function and of the source, for example G^{zx} is the z component of the Green's function at point $\mathbf{r}$ due to an x directed point current source located at $\mathbf{r}'$. The functions $F^{HED}_{E_z}$ and $F^{HED}_{H_z}$ are the z-dependent solutions of wave propagation for a horizontal electric dipole source embedded in a multi-layered substrate.

A vertical electric dipole (VED) has $\hat{\boldsymbol{\alpha}} = \hat{\mathbf{z}}$. For the source located in medium m, Eqns. 2.12 and 2.13 give the Green's functions for the normal components of field in layer n as

$$\begin{aligned} G^{zz}_{EJ,n} &= -\frac{I\ell}{4\pi}\frac{j}{\omega\epsilon_n}\int_0^\infty J_0(k_\rho\rho)\frac{k_\rho^3}{jk_{mz}}F^{VED}_{E_z}dk_\rho \\ G^{zz}_{HJ,n} &= 0, \end{aligned} \tag{2.15}$$

implying the absence of a normal field component for TE wave propagation.

The physical interpretation of Eqns. 2.14 and 2.15 are that the z component of the field can be expanded as an integral summation of cylindrical waves in the ρ direction and a plane wave in the z direction over all wave numbers k_ρ. Since cylindrical waves may be represented as linear superpositions of plane waves, the integrands in fact consist of a superposition of TM- or TE-type plane waves [23].

For the i^{th} medium, k_{iz} represents the wave number in the z direction in the same sense that k_ρ is the wave number in the ρ direction. The relation $k_{iz}^2 = k_i^2 - k_\rho^2$ holds where the square roots defining k_{iz} and k_i are to be taken with negative imaginary parts.

Following the formulation of Chew [23] for planarly layered media, the terms $F^{HED}_{E_z}$, $F^{HED}_{H_z}$ and $F^{VED}_{E_z}$ can be computed depending on the source and observation layers.

Observation point and source in the same layer, $n = m$

The solution for a finite thickness layer with the source inside, is the sum of the particular and homogeneous solutions.

The particular solution corresponds to the source embedded and radiating in an unbounded homogeneous medium of the same characteristics as the m^{th} layer. In the spectral domain z-dependency of the solution is of the form $e^{-jk_{mz}|z-z'|}$.[2]

Inside the m^{th} layer the z variation of the solution is augmented by a downgoing wave plus an upgoing wave. For the HED and the VED

$$\begin{aligned} F_{E_z}^{HED} &= \mp e^{-jk_{mz}|z-z'|} + B_m^{TM,HED} e^{jk_{mz}z} + D_m^{TM,HED} e^{-jk_{mz}z} \\ F_{H_z}^{HED} &= e^{-jk_{mz}|z-z'|} + B_m^{TE,HED} e^{jk_{mz}z} + D_m^{TE,HED} e^{-jk_{mz}z} \\ F_{E_z}^{VED} &= e^{-jk_{mz}|z-z'|} + B_m^{TM,VED} e^{jk_{mz}z} + D_m^{TM,VED} e^{-jk_{mz}z}. \end{aligned} \tag{2.16}$$

The last two terms are due to reflected waves at the region boundaries. The amplitude coefficients B_m and D_m are found by deriving transmission line constraint conditions for the waves at $z = -d_{m-1}$ and $z = -d_m$. The downgoing wave for $z > z'$ is a consequence of the reflection of the upgoing wave for $z > z'$ at $z = -d_{m-1}$. Similarly, for $z < z'$, the upgoing and downgoing waves at $z = -d_m$ are related. The amplitude coefficients are given by the simultaneous solution to the expressed relations, i.e.,

$$\begin{aligned} B_m^{TM,HED} &= \tilde{R}_{m,m-1}^{TM}\left[-e^{-jk_{mz}|d_{m-1}+z'|} + e^{-jk_{mz}(d_m-d_{m-1})}\tilde{R}_{m,m+1}^{TM} e^{-jk_{mz}|d_m+z'|}\right]\tilde{M}_m^{TM} e^{jk_{mz}d_{m-1}} \\ D_m^{TM,HED} &= \tilde{R}_{m,m+1}^{TM}\left[+e^{-jk_{mz}|d_m+z'|} - e^{-jk_{mz}(d_m-d_{m-1})}\tilde{R}_{m,m-1}^{TM} e^{-jk_{mz}|d_{m-1}+z'|}\right]\tilde{M}_m^{TM} e^{-jk_{mz}d_m} \\ B_m^{TE,HED} &= \tilde{R}_{m,m-1}^{TE}\left[+e^{-jk_{mz}|d_{m-1}+z'|} + e^{-jk_{mz}(d_m-d_{m-1})}\tilde{R}_{m,m+1}^{TE} e^{-jk_{mz}|d_m+z'|}\right]\tilde{M}_m^{TE} e^{jk_{mz}d_{m-1}} \\ D_m^{TE,HED} &= \tilde{R}_{m,m+1}^{TE}\left[+e^{-jk_{mz}|d_m+z'|} + e^{-jk_{mz}(d_m-d_{m-1})}\tilde{R}_{m,m-1}^{TE} e^{-jk_{mz}|d_{m-1}+z'|}\right]\tilde{M}_m^{TE} e^{-jk_{mz}d_m} \\ B_m^{TM,VED} &= \tilde{R}_{m,m-1}^{TM}\left[+e^{-jk_{mz}|d_{m-1}+z'|} + e^{-jk_{mz}(d_m-d_{m-1})}\tilde{R}_{m,m+1}^{TM} e^{-jk_{mz}|d_m+z'|}\right]\tilde{M}_m^{TM} e^{jk_{mz}d_{m-1}} \\ D_m^{TM,VED} &= \tilde{R}_{m,m+1}^{TM}\left[+e^{-jk_{mz}|d_m+z'|} + e^{-jk_{mz}(d_m-d_{m-1})}\tilde{R}_{m,m-1}^{TM} e^{-jk_{mz}|d_{m-1}+z'|}\right]\tilde{M}_m^{TM} e^{-jk_{mz}d_m} \end{aligned} \tag{2.17}$$

and

$$\begin{aligned} \tilde{M}_m^{TM} &= [1 - \tilde{R}_{m,m-1}^{TM}\tilde{R}_{m,m+1}^{TM} e^{-2jk_{mz}(d_m-d_{m-1})}]^{-1} \\ \tilde{M}_m^{TE} &= [1 - \tilde{R}_{m,m-1}^{TE}\tilde{R}_{m,m+1}^{TE} e^{-2jk_{mz}(d_m-d_{m-1})}]^{-1}. \end{aligned} \tag{2.18}$$

$\tilde{R}_{i,i-1}$ and $\tilde{R}_{i,i+1}$ are the generalised reflection coefficients that relate the amplitude of the reflected wave to the amplitude of the incident wave. These include the effect of

[2]Some sources generate a field that is odd-symmetric about z' in a homogeneous medium, of the form $\mp e^{-jk_{mz}|z-z'|}$.

subsurface reflection and can be written as

$$\begin{aligned}\tilde{R}_{i,i-1} &= \frac{R_{i,i-1} + \tilde{R}_{i-1,i-2}e^{-2jk_{i-1,z}(d_{i-1}-d_{i-2})}}{1 + R_{i,i-1}\tilde{R}_{i-1,i-2}e^{-2jk_{i-1,z}(d_{i-1}-d_{i-2})}} \\ \tilde{R}_{i,i+1} &= \frac{R_{i,i+1} + \tilde{R}_{i+1,i+2}e^{-2jk_{i+1,z}(d_{i+1}-d_{i})}}{1 + R_{i,i+1}\tilde{R}_{i+1,i+2}e^{-2jk_{i+1,z}(d_{i+1}-d_{i})}}\end{aligned} \tag{2.19}$$

with $R_{i,i-1}$ and $R_{i,i+1}$ the Fresnel coefficients

$$\begin{aligned}R^{TM}_{i,i-1} &= \frac{\epsilon_{i-1}k_{iz} - \epsilon_i k_{i-1,z}}{\epsilon_{i-1}k_{iz} + \epsilon_i k_{i-1,z}} \\ R^{TE}_{i,i-1} &= \frac{\mu_{i-1}k_{iz} - \mu_i k_{i-1,z}}{\mu_{i-1}k_{iz} + \mu_i k_{i-1,z}}\end{aligned} \tag{2.20}$$

and

$$\begin{aligned}R^{TM}_{i,i+1} &= \frac{\epsilon_{i+1}k_{iz} - \epsilon_i k_{i+1,z}}{\epsilon_{i+1}k_{iz} + \epsilon_i k_{i+1,z}} \\ R^{TE}_{i,i+1} &= \frac{\mu_{i+1}k_{iz} - \mu_i k_{i+1,z}}{\mu_{i+1}k_{iz} + \mu_i k_{i+1,z}}.\end{aligned} \tag{2.21}$$

It is important to note that R^{TM} is the reflection coefficient associated with either $H_{\text{tangential}}$ or $\epsilon E_{\text{normal}}$, while R^{TE} is the reflection coefficient associated with $E_{\text{tangential}}$ or μH_{normal}.

Eqn. 2.19 can be solved recursively for $\tilde{R}_{i,i-1}$ or $\tilde{R}_{i,i+1}$ in all layers knowing the termination of Regions 1 and N. With Region N extending to $-\infty$, $\tilde{R}_{N,N+1} = 0$. When a perfect electric conductor (PEC) is present at $z = -d_{N-1}$ however, boundary conditions for the total normal field components are $E_{\text{normal}} = 2E_{\text{incident}}$ and $H_{\text{normal}} = 0$ (or for the total tangential field components $E_{\text{tangential}} = 0$ and $H_{\text{tangential}} = 2H_{\text{incident}}$). Thus $\tilde{R}^{TE}_{N-1,N} = -1$ and $\tilde{R}^{TM}_{N-1,N} = 1$. Similar results hold when Region 1 is a half-space or the plane at $z = -d_1$ is a perfect electric conductor.

Note that in Eqn. 2.16, the direct term for an HED shows opposite signs for the downgoing and upgoing waves. This is because E_z for an HED is odd about $z = z'$ and may be proved using the Sommerfeld identity Eqn. 2.11, and taking the derivative in Eqn. 2.9.

Observation point in layer $n < m$

Using the recursive method of [23][3], the z-dependence of the field in Region n can be written as

$$\begin{aligned} F_{E_z}^{HED} &= A_n^{TM,HED+}\left[e^{-jk_{nz}z} + \tilde{R}_{n,n-1}^{TM} e^{2jk_{nz}d_{n-1}+jk_{nz}z}\right] \\ F_{H_z}^{HED} &= A_n^{TE,HED+}\left[e^{-jk_{nz}z} + \tilde{R}_{n,n-1}^{TE} e^{2jk_{nz}d_{n-1}+jk_{nz}z}\right] \\ F_{E_z}^{VED} &= A_n^{TM,VED+}\left[e^{-jk_{nz}z} + \tilde{R}_{n,n-1}^{TM} e^{2jk_{nz}d_{n-1}+jk_{nz}z}\right], \end{aligned} \tag{2.22}$$

with A_n^+ the amplitude of the upgoing wave, given by

$$A_n^+ e^{jk_{nz}d_n} = A_m^+ e^{jk_{mz}d_m} \prod_{i=n}^{m-1} \left(e^{-jk_{i+1,z}(d_{i+1}-d_i)} S_{i+1,i}^+\right) \tag{2.23}$$

and

$$S_{i+1,i}^+ = \frac{T_{i+1,i}}{1 - R_{i,i+1}\tilde{R}_{i,i-1}e^{-2jk_{iz}(d_i-d_{i-1})}}. \tag{2.24}$$

To calculate A_m^+, substitute Eqn. 2.17 back into Eqn. 2.16 and write all terms with a common denominator. The resulting equation clearly separates into an upgoing and a downgoing wave, one of which resembles a form similar to Eqn. 2.22. The amplitude of the upgoing wave in the source layer can be logically deduced and the expressions are given by

$$\begin{aligned} A_m^{TM,HED+} &= \left[-e^{jk_{mz}z'} + e^{-jk_{mz}(2d_m+z')}\tilde{R}_{m,m+1}^{TM}\right]\tilde{M}_m^{TM} \\ A_m^{TE,HED+} &= \left[+e^{jk_{mz}z'} + e^{-jk_{mz}(2d_m+z')}\tilde{R}_{m,m+1}^{TE}\right]\tilde{M}_m^{TE} \\ A_m^{TM,VED+} &= \left[+e^{jk_{mz}z'} + e^{-jk_{mz}(2d_m+z')}\tilde{R}_{m,m+1}^{TM}\right]\tilde{M}_m^{TM}. \end{aligned} \tag{2.25}$$

Note that the transmission coefficient $T_{i+1,i}$ of Eqn. 2.24 is connected to the reflection coefficient $R_{i+1,i}$ through the relation $T_{i+1,i} = 1 + R_{i+1,i}$.

Observation point in layer $n > m$

Similar to the calculation of the upgoing wave in a layer $n < m$, the z-dependence of the field in Region n, with $n > m$, can be found[4]

$$\begin{aligned} F_{E_z}^{HED} &= A_n^{TM,HED-}\left[e^{jk_{nz}z} + \tilde{R}_{n,n+1}^{TM} e^{-2jk_{nz}d_n-jk_{nz}z}\right] \\ F_{H_z}^{HED} &= A_n^{TE,HED-}\left[e^{jk_{nz}z} + \tilde{R}_{n,n+1}^{TE} e^{-2jk_{nz}d_n-jk_{nz}z}\right] \\ F_{E_z}^{VED} &= A_n^{TM,VED-}\left[e^{jk_{nz}z} + \tilde{R}_{n,n+1}^{TM} e^{-2jk_{nz}d_n-jk_{nz}z}\right], \end{aligned} \tag{2.26}$$

[3][23, Eqns. 2.4.8 and 2.4.9] are erroneous

[4][23, Eqns. 2.4.11 and 2.4.12] are erroneous

with A_n^- the amplitude of the downgoing wave, given by

$$A_n^- e^{-jk_{nz}d_{n-1}} = A_m^- e^{-jk_{mz}d_{m-1}} \prod_{i=m}^{n-1} \left(e^{-jk_{iz}(d_i - d_{i-1})} S_{i,i+1}^- \right) \tag{2.27}$$

and

$$S_{i,i+1}^- = \frac{T_{i,i+1}}{1 - R_{i+1,i}\tilde{R}_{i+1,i+2}e^{-2jk_{i+1,z}(d_{i+1}-d_i)}}. \tag{2.28}$$

To calculate the amplitude of the downgoing wave in the source layer A_m^-, the same procedure as was used to calculate the amplitude of the upgoing wave is applied, giving

$$\begin{aligned} A_m^{TM,HED-} &= \left[+e^{-jk_{mz}z'} - e^{jk_{mz}(2d_{m-1}+z')}\tilde{R}_{m,m-1}^{TM} \right] \tilde{M}_m^{TM} \\ A_m^{TE,HED-} &= \left[+e^{-jk_{mz}z'} + e^{jk_{mz}(2d_{m-1}+z')}\tilde{R}_{m,m-1}^{TE} \right] \tilde{M}_m^{TE} \\ A_m^{TM,VED-} &= \left[+e^{-jk_{mz}z'} + e^{jk_{mz}(2d_{m-1}+z')}\tilde{R}_{m,m-1}^{TM} \right] \tilde{M}_m^{TM}. \end{aligned} \tag{2.29}$$

2.4 Duality Principle and Magnetic Dipole Fields

No magnetic charge has yet been found to exist in nature [27]. In practice, however, it is often convenient to use the concept of fictitious magnetic currents and charges to introduce symmetry in Maxwell's equations. By making use of the simple but important principle of duality, a given solution may be transformed to other useful ones leaving Maxwell's curl equations invariant. The following replacements will be used throughout this thesis

$$\begin{array}{cccc} \mathbf{E} \to \mathbf{H} & \mathbf{J} \to \mathbf{M} & \rho \to \rho_m & \mu \to \epsilon \\ \mathbf{H} \to -\mathbf{E} & \mathbf{M} \to -\mathbf{J} & \rho_m \to -\rho & \epsilon \to \mu \quad . \end{array} \tag{2.30}$$

The principle of duality may be utilised to save work in finding the solution to the fields in a homogeneous medium due to a magnetic point current source directed in the $\hat{\boldsymbol{\alpha}}$ direction.

A magnetic dipole can be simulated by a small electric current loop. The field it generates is dual to that of an electric Hertzian dipole. Ramo et al. [28] showed that a current loop of area A and current I has a magnetic dipole moment $m = IA$, and this gives the same form of magnetic field as the electric field given by an electric dipole with moment $p = q\ell$. For an electric Hertzian dipole, $I\ell = \ell dq/dt = j\omega p$. Hence, replacing p by μIA and making duality interchanges, the fields of a magnetic dipole are found.

With $\mathbf{M}(\mathbf{r}) = \hat{\boldsymbol{\alpha}} j\omega\mu IA\delta(\mathbf{r})$ the resulting field equations are

$$\begin{aligned} \mathbf{E}(\mathbf{r}) &= -j\omega\mu\nabla \times \hat{\boldsymbol{\alpha}} IA \frac{e^{-jkr}}{4\pi r} \\ \mathbf{H}(\mathbf{r}) &= k^2 \left(\bar{\bar{\mathbf{I}}} + \frac{\nabla\nabla}{k^2} \right) \cdot \hat{\boldsymbol{\alpha}} IA \frac{e^{-jkr}}{4\pi r}. \end{aligned} \tag{2.31}$$

Using the above relations the normal Green's function expansions for TM and TE wave propagation for a magnetic dipole embedded in a layered medium follow.

For a horizontal magnetic dipole (HMD) located in medium m and pointing in the x direction, the respective Green's functions for the normal field component wave propagation in medium n are

$$\begin{aligned} G^{zx}_{EM,n} &= -j\omega\mu_m \frac{IA}{4\pi}\sin\phi \int_0^\infty J_1(k_\rho\rho)\frac{k_\rho^2}{jk_{mz}} F^{HMD}_{E_z}\frac{\epsilon_m}{\epsilon_n}dk_\rho \\ G^{zx}_{HM,n} &= -\frac{IA}{4\pi}\cos\phi \int_0^\infty J_1(k_\rho\rho)k_\rho^2 F^{HMD}_{H_z}\frac{\mu_m}{\mu_n}dk_\rho. \end{aligned} \tag{2.32}$$

A vertical magnetic dipole (VMD) located in medium m has a zero E_z component, therefore no TM wave. Using Eqn. 2.31, the Green's function expansion of the normal field component for TE wave propagation in medium n is

$$G^{zz}_{HM,n} = \frac{IA}{4\pi}\int_0^\infty J_0(k_\rho\rho)\frac{k_\rho^3}{jk_{mz}} F^{VMD}_{H_z}\frac{\mu_m}{\mu_n}dk_\rho. \tag{2.33}$$

The expressions for $F^{HMD}_{E_z}$, $F^{HMD}_{H_z}$ and $F^{VMD}_{H_z}$ may be computed using Eqns. 2.16, 2.22 and 2.26 (dependent on the respective source and observation layers) and the duality interchange $\epsilon \leftrightarrow \mu$. For a complete analysis refer to Appendix E.

2.5 Vector and Scalar Potential Green's Functions

The Green's functions in layered media comprise Sommerfeld-type integrals, which are extremely laborious to evaluate. The Method of Moments (MoM) procedure of Chapter 4 is based on a mixed-potential form of the electric field integral equation (EFIE)—so named, because it involves both vector and scalar potentials. The former is expressed in terms of the induced current, and the latter in terms of the induced charge. The mixed-potential EFIE (MPIE) is preferable to several other variants of the EFIE because it requires only the potential forms of the Green's functions. In layered media, this has a pronounced advantage—the Sommerfeld integrals it requires are less singular and converge faster than the field forms present in any other form of the EFIE [6].

Time-varying electromagnetic fields are related to each other and to the charge and current sources through Maxwell's equations. Vector and scalar potentials are intermediate functions which are directly related to the sources, and from which the electric and magnetic fields may be derived as

$$\begin{aligned} \mathbf{E} &= -j\omega\mathbf{A} - \nabla\Phi - \frac{1}{\epsilon}\nabla\times\mathbf{F} \\ \mathbf{H} &= -j\omega\mathbf{F} - \nabla\Psi + \frac{1}{\mu}\nabla\times\mathbf{A} \end{aligned} \tag{2.34}$$

with $\mathbf{A}$ and Φ the magnetic vector and electric scalar potentials respectively; and $\mathbf{F}$ and Ψ the dual electric vector and magnetic scalar potentials.

Now consider two arbitrary dipoles with moments $Id\boldsymbol{\ell}$ and $Id\mathbf{A}$ located at $\mathbf{r}'$. The vector potentials at the point $\mathbf{r}$ due to these dipoles are

$$\mathbf{A}(\mathbf{r}) = \bar{\bar{\mathbf{G}}}_A(\mathbf{r}|\mathbf{r}') \cdot Id\boldsymbol{\ell} \qquad \mathbf{F}(\mathbf{r}) = \bar{\bar{\mathbf{G}}}_F(\mathbf{r}|\mathbf{r}') \cdot Id\mathbf{A} \tag{2.35}$$

where $\bar{\bar{\mathbf{G}}}_A$ and $\bar{\bar{\mathbf{G}}}_F$ are three-dimensional dyadic Green's functions. The notation G_A^{xy} gives the x component of the magnetic vector potential at point $\mathbf{r}$ created by a unity moment y directed electric dipole at point $\mathbf{r}'$. G_F^{xy} is the dual electric vector potential element due to a magnetic dipole. Also, it is assumed that $Id\ell = IdA = 1$. The vector potentials for the unity moment dipoles pointing in an arbitrary direction $\hat{\boldsymbol{\alpha}}$, are therefore

$$\mathbf{A}(\mathbf{r}) = \bar{\bar{\mathbf{G}}}_A(\mathbf{r}|\mathbf{r}') \cdot \hat{\boldsymbol{\alpha}} \qquad \mathbf{F}(\mathbf{r}) = \bar{\bar{\mathbf{G}}}_F(\mathbf{r}|\mathbf{r}') \cdot \hat{\boldsymbol{\alpha}}. \tag{2.36}$$

By introducing the magnetic vector potential in the Lorenz gauge $j\omega\mu\epsilon\Phi + \nabla \cdot \mathbf{A} = 0$, the scalar potential associated with the directed electric dipole can be written as

$$j\omega\mu\epsilon\Phi = -\nabla \cdot \bar{\bar{\mathbf{G}}}_A(\mathbf{r}|\mathbf{r}') \cdot \hat{\boldsymbol{\alpha}}. \tag{2.37}$$

It is also known that the scalar potential G_Φ of a unit point charge is related to the scalar potential Φ of a time-harmonic dipole pointing in the $\hat{\boldsymbol{\alpha}}$ direction. The relation is given by [29]

$$\Phi = -\frac{1}{j\omega}\nabla G_\Phi(\mathbf{r}|\mathbf{r}') \cdot \hat{\boldsymbol{\alpha}} = \frac{1}{j\omega}\nabla' G_\Phi(\mathbf{r}|\mathbf{r}') \cdot \hat{\boldsymbol{\alpha}}. \tag{2.38}$$

A comparison of Eqns. 2.37 and 2.38 establishes the connection between $\bar{\bar{\mathbf{G}}}_A$ and G_Φ, namely that

$$\frac{j\omega}{k^2}\nabla \cdot \bar{\bar{\mathbf{G}}}_A(\mathbf{r}|\mathbf{r}') = -\frac{1}{j\omega}\nabla G_\Phi(\mathbf{r}|\mathbf{r}') = \frac{1}{j\omega}\nabla' G_\Phi(\mathbf{r}|\mathbf{r}'). \tag{2.39}$$

From Eqn. 2.35 it follows that the magnetic vector potential for a given surface current distribution is

$$\mathbf{A}(\mathbf{r}) = \int_S \bar{\bar{\mathbf{G}}}_A(\mathbf{r}|\mathbf{r}') \cdot \mathbf{J}_s(\mathbf{r}')dS'. \tag{2.40}$$

This surface current density $\mathbf{J}_s$ causes a surface charge q_s according to the continuity or charge conservation rule $\nabla \cdot \mathbf{J}_s + j\omega q_s = 0$. The electric scalar potential associated with the surface charge is given by

$$\Phi(\mathbf{r}) = \int_S G_\Phi(\mathbf{r}|\mathbf{r}')q_s(\mathbf{r}')dS' \tag{2.41}$$

where G_Φ is subject to satisfying the relationship between the vector and scalar potential Green's functions of Eqn. 2.39.

Similar results hold for the electric potentials, i.e.,

$$\begin{aligned} \mathbf{F}(\mathbf{r}) &= \int_S \bar{\bar{\mathbf{G}}}_F(\mathbf{r}|\mathbf{r}') \cdot \mathbf{M}_s(\mathbf{r}') dS' \\ \Psi(\mathbf{r}) &= \int_S G_\Psi(\mathbf{r}|\mathbf{r}') q_{ms}(\mathbf{r}') dS' \end{aligned} \tag{2.42}$$

with $\bar{\bar{\mathbf{G}}}_F$ and G_Ψ the electric vector and magnetic scalar potential Green's functions, and q_{ms} the magnetic surface charge caused by the magnetic surface current density $\mathbf{M}_s$.

2.6 Magnetic Potential Green's Functions

The dyadic for the vector potential $\bar{\bar{\mathbf{G}}}_A$, can be expressed as

$$\bar{\bar{\mathbf{G}}}_A = (\hat{\mathbf{x}} G_A^{xx} + \hat{\mathbf{z}} G_A^{zx})\hat{\mathbf{x}} + (\hat{\mathbf{y}} G_A^{yy} + \hat{\mathbf{z}} G_A^{zy})\hat{\mathbf{y}} + \hat{\mathbf{z}} G_A^{zz} \hat{\mathbf{z}}. \tag{2.43}$$

This form of the Green's function results from the traditional Sommerfeld approach [14], which postulates that a horizontal, say, x directed dipole, generates a z component in addition to the x component of the vector potential. This is to satisfy the boundary conditions at the interfaces between dielectric layers. However, one may as well take the y component of the vector potential to accompany the primary x component. This leads to an alternative form of the dyadic Green's function

$$\bar{\bar{\mathbf{G}}}_A = (\hat{\mathbf{x}} G_A^{xx} + \hat{\mathbf{y}} G_A^{yx})\hat{\mathbf{x}} + (\hat{\mathbf{x}} G_A^{xy} + \hat{\mathbf{y}} G_A^{yy})\hat{\mathbf{y}} + \hat{\mathbf{z}} G_A^{zz} \hat{\mathbf{z}}. \tag{2.44}$$

Note that except for G_A^{zz}, the corresponding components in Eqns. 2.43 and 2.44 are different, even though the same notation is used.

Several researchers have previously recognised the advantages of the MPIE formulation in solving antenna problems in layered media. According to Michalski and Zheng [6], the success of these efforts can be attributed to the fact that the structures considered could only support either vertical or horizontal components of current. It was also assumed that the antenna or scatterer was confined to a single layer.

When the medium is stratified, G_Φ satisfying Eqn. 2.39 does not in general exist. Unlike in free space, the vector and scalar potentials are not unique and the scalar potentials of point charges associated with horizontal and vertical dipoles are not, in general, identical. It now becomes a nontrivial task to formulate a mixed-potential integral equation (MPIE) for objects of arbitrary shape in a layered medium.

Michalski and Zheng [6, 17] formulated an electric field MPIE that extended an existing solution technique developed for objects in free space. The solution employs the method

of moment procedures originated by Rao, Wilton and Glisson [11] for an arbitrary surface penetrating one or more interfaces.

The proposed solution introduces a scalar function K_Φ and vector function $\mathbf{P}$ according to

$$\frac{j\omega}{k^2}\nabla\cdot\bar{\bar{\mathbf{G}}}_A = \frac{1}{j\omega}\nabla' K_\Phi + j\omega\mathbf{P}. \tag{2.45}$$

Note that Eqn. 2.45 would have the desired form of Eqn. 2.39 if it were not for the "correction term" comprising $\mathbf{P}$. Michalski and Zheng have shown that this term may be incorporated into a new vector potential kernel $\bar{\bar{\mathbf{K}}}_A$, via

$$\bar{\bar{\mathbf{K}}}_A = \bar{\bar{\mathbf{G}}}_A + \nabla\mathbf{P}. \tag{2.46}$$

Also, the choice of K_Φ and $\mathbf{P}$ in Eqn. 2.45 is not unique. Three particularly useful choices were discussed and the so-called Formulation C was shown to be simpler than the others in the case where the object penetrates one or more layers. Note that both Formulations A and B use the alternative form of the dyadic Green's function given in Eqn. 2.44, while Formulation C employs the traditional Sommerfeld form of $\bar{\bar{\mathbf{G}}}_A$ given in Eqn. 2.43.

Following from Eqn. 2.45 with $P_x = P_y = 0$ in Formulation C, the relationship between the vector and the scalar potential is

$$\begin{aligned}
\frac{j\omega}{k^2}\Big(\frac{\partial}{\partial x}G_A^{xx} + \frac{\partial}{\partial z}G_A^{zx}\Big) &= \frac{1}{j\omega}\frac{\partial}{\partial x'}K_\Phi \\
\frac{j\omega}{k^2}\Big(\frac{\partial}{\partial y}G_A^{yy} + \frac{\partial}{\partial z}G_A^{zy}\Big) &= \frac{1}{j\omega}\frac{\partial}{\partial y'}K_\Phi \\
\frac{j\omega}{k^2}\frac{\partial}{\partial z}G_A^{zz} &= \frac{1}{j\omega}\frac{\partial}{\partial z'}K_\Phi + j\omega P_z.
\end{aligned} \tag{2.47}$$

The distinguishing feature of each formulation is the choice of the scalar potential kernel K_Φ, which also specifies the vector $\mathbf{P}$ according to Eqn. 2.45. In Formulation C, K_Φ can be interpreted as the scalar potential of a point charge associated with a horizontal dipole, i.e., $K_\Phi = G_\Phi$.

From Eqn. 2.46 it follows that Formulation C introduces two new entries, not present in $\bar{\bar{\mathbf{G}}}_A$, to the dyadic kernel

$$\begin{aligned}
K_A^{xz} &= \frac{\partial}{\partial x}P_z, \\
K_A^{yz} &= \frac{\partial}{\partial y}P_z
\end{aligned} \tag{2.48}$$

and adds an extra term to G_A^{zz}

$$K_A^{zz} = G_A^{zz} + \frac{\partial}{\partial z}P_z \tag{2.49}$$

where P_z is computed using Eqn. 2.47.

Hence, the dyadic kernel for the vector potential $\bar{\bar{\mathbf{K}}}_A$, using Formulation C of Michalski et al. [6, Eqn. 48] is given by

$$\bar{\bar{\mathbf{K}}}_A = (\hat{\mathbf{x}}\hat{\mathbf{x}} + \hat{\mathbf{y}}\hat{\mathbf{y}})G_A^{xx} + \hat{\mathbf{x}}\hat{\mathbf{z}}K_A^{xz} + \hat{\mathbf{y}}\hat{\mathbf{z}}K_A^{yz} + \hat{\mathbf{z}}\hat{\mathbf{x}}G_A^{zx} + \hat{\mathbf{z}}\hat{\mathbf{y}}G_A^{zy} + \hat{\mathbf{z}}\hat{\mathbf{z}}K_A^{zz}. \tag{2.50}$$

Formulation C enjoys a clear advantage over other formulations—undesirable contour integrals cancel, which means that the scalar potential kernel is continuous with respect to z'; and K_Φ is continuous at the interfaces with respect to z, which results in considerable simplification in the numerical procedure when the source object penetrates one or more interfaces [6].

To derive the Green's functions, we write the potentials in the spectral domain in terms of the normal components for the fields [24], [30]. Appendix B gives a detailed discussion on deriving these relations

$$\begin{aligned}
\tilde{G}_A^{xx} &= -\frac{\mu}{jk_y}\tilde{G}_{HJ}^{zx} \\
\tilde{G}_A^{yy} &= \frac{\mu}{jk_x}\tilde{G}_{HJ}^{zy} \\
k_\rho^2\tilde{G}_A^{zx} &= j\omega\mu\epsilon\tilde{G}_{EJ}^{zx} + \frac{k_x\mu}{k_y}\frac{\partial}{\partial z}\tilde{G}_{HJ}^{zx} \\
k_\rho^2\tilde{G}_A^{zy} &= j\omega\mu\epsilon\tilde{G}_{EJ}^{zy} - \frac{k_y\mu}{k_x}\frac{\partial}{\partial z}\tilde{G}_{HJ}^{zy} \\
k_\rho^2\tilde{G}_A^{zz} &= j\omega\mu\epsilon\tilde{G}_{EJ}^{zz} \\
\tilde{G}_\Phi &= \frac{j\omega}{k_\rho^2 jk_x}\frac{\partial}{\partial z}\tilde{G}_{EJ}^{zx} - \left(\frac{k}{k_\rho}\right)^2\frac{1}{jk_y\epsilon}\tilde{G}_{HJ}^{zx}.
\end{aligned} \tag{2.51}$$

Furthermore, the three additional components in the vector potential kernel are

$$\begin{aligned}
\tilde{K}_A^{xz} &= \frac{jk_x}{k^2}\frac{\partial}{\partial z}\tilde{G}_A^{zz} + \frac{jk_x}{\omega^2}\frac{\partial}{\partial z'}\tilde{G}_\Phi \\
\tilde{K}_A^{yz} &= \frac{jk_x}{k^2}\frac{\partial}{\partial z}\tilde{G}_A^{zz} + \frac{jk_y}{\omega^2}\frac{\partial}{\partial z'}\tilde{G}_\Phi \\
\tilde{K}_A^{zz} &= \left(\frac{k_\rho}{k}\right)^2\tilde{G}_A^{zz} + \frac{1}{\omega^2}\frac{\partial^2}{\partial z'\partial z}\tilde{G}_\Phi.
\end{aligned} \tag{2.52}$$

Now, Eqns. 2.14 and 2.15 give the Green's functions for the normal field components E_z and H_z. Using these relations, define—in the spectral domain—in terms of dyadic Green's functions

$$\begin{aligned}
\tilde{G}_{EJ}^{zx} &= \frac{I\ell}{4\pi\omega\epsilon_n}F_{E_z}^{HED} \\
\tilde{G}_{HJ}^{zx} &= -\frac{I\ell}{4\pi}\frac{F_{H_z}^{HED}}{k_{mz}}\frac{\mu_m}{\mu_n}
\end{aligned} \tag{2.53}$$

and

$$\tilde{G}_{EJ}^{zz} = -\frac{I\ell}{4\pi\omega\epsilon_n}\frac{k_\rho^2}{k_{mz}}F_{E_z}^{VED}. \tag{2.54}$$

Before computing the spatial domain Green's functions, the k_x and k_y dependence of the amplitudes in the spectral domain dyadic Green's functions (Eqns. 2.53 and 2.54) must be explicitly known. Realising that

$$G_{EJ}^{zx} = -j\mathcal{F}^{-1}\{jk_x\tilde{G}_{EJ}^{zx}\}$$
$$G_{HJ}^{zx} = -j\mathcal{F}^{-1}\{jk_y\tilde{G}_{HJ}^{zx}\}$$

and

$$G_{EJ}^{zz} = \mathcal{F}^{-1}\{\tilde{G}_{EJ}^{zz}\}, \tag{2.55}$$

it follows that by means of a constant amplitude extraction and substitution into Eqn. 2.51, the scalar potential Green's function can be calculated from

$$\tilde{G}_\Phi = \frac{\omega}{k_\rho^2}\frac{\partial}{\partial z}\tilde{G}_{EJ}^{zx} - \Big(\frac{k}{k_\rho}\Big)^2\frac{1}{j\epsilon}\tilde{G}_{HJ}^{zx} \tag{2.56}$$

and the elements for the dyadic vector potential from

$$\begin{aligned}
\tilde{G}_A^{xx} &= -\frac{\mu}{j}\tilde{G}_{HJ}^{zx}\\
\tilde{G}_A^{yy} &= \frac{\mu}{j}\tilde{G}_{HJ}^{zy} = -\frac{\mu}{j}\tilde{G}_{HJ}^{zx}\\
k_\rho^2\tilde{G}_A^{zx} &= j\omega\mu\epsilon k_x\tilde{G}_{EJ}^{zx} + k_x\mu\frac{\partial}{\partial z}\tilde{G}_{HJ}^{zx}\\
k_\rho^2\tilde{G}_A^{zy} &= j\omega\mu\epsilon k_y\tilde{G}_{EJ}^{zy} - k_y\mu\frac{\partial}{\partial z}\tilde{G}_{HJ}^{zy}\\
&= j\omega\mu\epsilon k_y\tilde{G}_{EJ}^{zx} + k_y\mu\frac{\partial}{\partial z}\tilde{G}_{HJ}^{zx}\\
k_\rho^2\tilde{G}_A^{zz} &= j\omega\mu\epsilon\tilde{G}_{EJ}^{zz}.
\end{aligned} \tag{2.57}$$

Note that the subtlety $G_A^{xx} = G_A^{yy}$, first used in Eqn. 2.50, becomes apparent in the above relations. Also, it suffices to evaluate for G_Φ, G_A^{xx}, G_A^{zx} and from Eqn. 2.52 K_A^{xz} and K_A^{zz}.

By using Eqns. 2.52, 2.56 and 2.57, and applying the inverse Fourier identities of Eqn. A.5, the Green's functions in the frequency domain are obtained. For the scalar potential associated with an HED, the Sommerfeld integral can be written as

$$G_\Phi = \frac{I\ell}{4\pi\epsilon_n}\int_0^\infty J_0(k_\rho\rho)\Big(\frac{1}{k_\rho}\frac{\partial}{\partial z}F_{E_z}^{HED} + \frac{k_n^2}{jk_{mz}k_\rho}F_{H_z}^{HED}\frac{\mu_m}{\mu_n}\Big)dk_\rho. \tag{2.58}$$

Similarly, the Green's function potentials for G_A^{xx} and G_A^{zx} are given by

$$G_A^{xx} = \frac{\mu_n I\ell}{4\pi}\int_0^\infty J_0(k_\rho\rho)\frac{k_\rho}{jk_{mz}}F_{H_z}^{HED}\frac{\mu_m}{\mu_n}dk_\rho \tag{2.59}$$

and

$$G_A^{zx} = \frac{\mu_n I\ell}{4\pi}\cos\phi\int_0^\infty J_1(k_\rho\rho)\Big(-F_{E_z}^{HED} + \frac{1}{jk_{mz}}\frac{\partial}{\partial z}F_{H_z}^{HED}\frac{\mu_m}{\mu_n}\Big)dk_\rho. \tag{2.60}$$

When calculating the additional components K_A^{xz} and K_A^{zz} in the vector potential kernel, the equality

$$\frac{\partial}{\partial z'}F_{E_z}^{HED} = -jk_{mz}F_{E_z}^{VED} \tag{2.61}$$

holds. Using this relation and substituting appropriate results from Eqn. 2.57 into Eqn. 2.52, the Green's function for K_A^{xz} is given by

$$K_A^{xz} = \frac{\mu_n I\ell}{4\pi}\cos\phi\int_0^\infty J_1(k_\rho\rho)\frac{j}{k_{mz}}\Big(\frac{k_m^2}{k_n^2}\frac{\partial}{\partial z}F_{E_z}^{VED} + \frac{\partial}{\partial z'}F_{H_z}^{HED}\frac{\mu_m}{\mu_n}\Big)dk_\rho \tag{2.62}$$

and the Green's function for K_A^{zz} is

$$K_A^{zz} = -\frac{\mu_n I\ell}{4\pi}\int_0^\infty J_0(k_\rho\rho)\Big[j\Big(\frac{k_\rho}{k_{mz}}\frac{k_m^2}{k_n^2} - \frac{k_{mz}}{k_\rho}\Big)F_{E_z}^{VED} + \frac{j}{k_{mz}k_\rho}\frac{\partial^2}{\partial z'\partial z}F_{H_z}^{HED}\frac{\mu_m}{\mu_n}\Big]dk_\rho. \tag{2.63}$$

Note that Eqns. 2.58 to 2.63 are used when the source and observation points are in different non-adjacent layers and hence, $F_{E_z}^{HED}$, $F_{H_z}^{HED}$ and $F_{E_z}^{VED}$ are given by either Eqn. 2.22 or 2.26. The numerical evaluation and convergence properties of the Sommerfeld integrals will be discussed in Chapter 3. The integrand is slowly convergent and the possibility of extracting static terms to increase convergence is considered when the observer and source points are in the same, or adjacent layers.

To find the solution for the electric vector and scalar potential Green's functions $\bar{\bar{\mathbf{K}}}_F$ and G_Ψ, the principle of duality is again utilised. For a comprehensive analysis refer to Appendix F. Also, to put the potential Green's function analysis into perspective, the total field Green's functions for planar media were also developed and are presented in Appendix G.

Finally, on substituting $\bar{\bar{\mathbf{G}}}$ with $\bar{\bar{\mathbf{K}}}$ in Eqns. 2.40 to 2.42, the magnetic vector and electric scalar potentials may be redefined as

$$\begin{aligned}\mathbf{A}(\mathbf{r}) &= \int_S \bar{\bar{\mathbf{K}}}_A(\mathbf{r}|\mathbf{r}')\cdot\mathbf{J}_s(\mathbf{r}')dS'\\ \Phi(\mathbf{r}) &= \int_S G_\Phi(\mathbf{r}|\mathbf{r}')q_s(\mathbf{r}')dS'\end{aligned} \tag{2.64}$$

and the dual potentials as

$$\begin{aligned}\mathbf{F}(\mathbf{r}) &= \int_S \bar{\bar{\mathbf{K}}}_F(\mathbf{r}|\mathbf{r}')\cdot\mathbf{M}_s(\mathbf{r}')dS'\\ \Psi(\mathbf{r}) &= \int_S G_\Psi(\mathbf{r}|\mathbf{r}')q_{ms}(\mathbf{r}')dS'.\end{aligned} \tag{2.65}$$

2.7 Derivation of $\nabla \times \bar{\bar{\mathbf{K}}}_F$ and $\nabla \times \bar{\bar{\mathbf{K}}}_A$

It follows from Eqn. 2.34, and the definitions for the potentials given in Eqns. 2.64 and 2.65, that, by taking the *curl* of the vector potentials $\mathbf{F}$ and $\mathbf{A}$, the terms $\nabla \times \bar{\bar{\mathbf{K}}}_F$ and $\nabla \times \bar{\bar{\mathbf{K}}}_A$ should be implicitly evaluated. An analytic solution for determining the *curl* of the dyadic Green's function kernels was employed.

Using the definition for differential operators in Cartesian coordinates, $\nabla \times \bar{\bar{\mathbf{K}}}$ evaluate to

$$\begin{aligned}
&(\frac{\partial}{\partial y}K^{zx} - \frac{\partial}{\partial z}K^{yx})\hat{\mathbf{x}}\hat{\mathbf{x}} + (\frac{\partial}{\partial y}K^{zy} - \frac{\partial}{\partial z}K^{yy})\hat{\mathbf{x}}\hat{\mathbf{y}} + (\frac{\partial}{\partial y}K^{zz} - \frac{\partial}{\partial z}K^{yz})\hat{\mathbf{x}}\hat{\mathbf{z}} \\
+ &(\frac{\partial}{\partial z}K^{xx} - \frac{\partial}{\partial x}K^{zx})\hat{\mathbf{y}}\hat{\mathbf{x}} + (\frac{\partial}{\partial z}K^{xy} - \frac{\partial}{\partial x}K^{zy})\hat{\mathbf{y}}\hat{\mathbf{y}} + (\frac{\partial}{\partial z}K^{xz} - \frac{\partial}{\partial x}K^{zz})\hat{\mathbf{y}}\hat{\mathbf{z}} \\
+ &(\frac{\partial}{\partial x}K^{yx} - \frac{\partial}{\partial y}K^{xx})\hat{\mathbf{z}}\hat{\mathbf{x}} + (\frac{\partial}{\partial x}K^{yy} - \frac{\partial}{\partial y}K^{xy})\hat{\mathbf{z}}\hat{\mathbf{y}} + (\frac{\partial}{\partial x}K^{yz} - \frac{\partial}{\partial y}K^{xz})\hat{\mathbf{z}}\hat{\mathbf{z}}.
\end{aligned} \tag{2.66}$$

For the particular choice where $\bar{\bar{\mathbf{K}}}$ assumes the form for the dyadic Green's function using Formulation C of Michalski et al. [6], a few simplifications can be made.

The terms K^{xy} and K^{yx} are both zero, and thus

$$\frac{\partial}{\partial z}K^{xy} = \frac{\partial}{\partial z}K^{yx} = \frac{\partial}{\partial y}K^{xy} = \frac{\partial}{\partial x}K^{yx} = 0. \tag{2.67}$$

From the definition for $\sin(\phi)$ and $\cos(\phi)$,

$$\cos(\phi) = \frac{x - x'}{\rho} \quad \text{and} \quad \sin(\phi) = \frac{y - y'}{\rho}, \tag{2.68}$$

it follows that K^{zx} and K^{zy} are equivalent, except for an interchange of the x and y variables. This is also true for the terms K^{xz} and K^{yz}. Also, with $K^{xx} = K^{yy}$, the following relations hold

$$\begin{aligned}
\frac{\partial}{\partial y}K^{zx} &= \frac{\partial}{\partial x}K^{zy} \\
\frac{\partial}{\partial y}K^{xz} &= \frac{\partial}{\partial x}K^{yz} \\
\frac{\partial}{\partial z}K^{xx} &= \frac{\partial}{\partial z}K^{yy} \\
\frac{\partial}{\partial z}K^{xz} &= \frac{\sin(\phi)}{\cos(\phi)}\frac{\partial}{\partial z}K^{yz}.
\end{aligned} \tag{2.69}$$

Finally, two useful identities for differentiating Bessel functions of the first kind are

$$\begin{aligned}
\frac{\partial}{\partial \rho}J_0(k_\rho \rho) &= -J_1(k_\rho \rho)k_\rho \\
\frac{\partial}{\partial \rho}J_1(k_\rho \rho) &= J_0(k_\rho \rho)k_\rho - \frac{1}{\rho}J_1(k_\rho \rho).
\end{aligned} \tag{2.70}$$

Using Eqns. 2.59 to 2.63 and utilising the above-mentioned simplifications, it is sufficient to differentiate only 6 of the 18 terms to completely describe Eqn. 2.66. To conclude this analysis, the three derivatives of G_A^{xx} (Eqn. 2.59) are listed to give an idea of the complexity involved when differentiating individual terms

$$\begin{aligned}
\frac{\partial}{\partial x}G_A^{xx} &= -\frac{\mu_n I\ell}{4\pi}\int_0^\infty J_1(k_\rho\rho)\frac{x-x'}{\rho}\frac{k_\rho^2}{jk_{mz}}F_{H_z}^{HED}\frac{\mu_m}{\mu_n}dk_\rho \\
\frac{\partial}{\partial y}G_A^{xx} &= -\frac{\mu_n I\ell}{4\pi}\int_0^\infty J_1(k_\rho\rho)\frac{y-y'}{\rho}\frac{k_\rho^2}{jk_{mz}}F_{H_z}^{HED}\frac{\mu_m}{\mu_n}dk_\rho \\
\frac{\partial}{\partial z}G_A^{xx} &= \frac{\mu_n I\ell}{4\pi}\int_0^\infty J_0(k_\rho\rho)\frac{k_\rho}{jk_{mz}}\frac{\partial}{\partial z}F_{H_z}^{HED}\frac{\mu_m}{\mu_n}dk_\rho.
\end{aligned} \tag{2.71}$$

2.8 Conclusion

The Green's functions of a time-harmonic electric dipole source, embedded either horizontally or vertically in a multi-layered medium, have been derived. The analysis focuses on a formulation presented by Chew [23] and Van Tonder [24]. Section 2.4 explained the duality principle, which was used to highlight important results appropriate to a magnetic dipole source. Finally, Sections 2.5 and 2.6 discussed the derivation of the Green's functions for the magnetic vector and scalar potentials suitable to Formulation C of Michalski and Zheng [6]. These are to be be used in the method of moment analysis (Chapter 4) to obtain the surface current distribution on electric and magnetic scatterers.

Chapter 3

Integration of the Green's Functions

The numerical evaluation of the Sommerfeld integrations involved in the Green's functions of a horizontal electric dipole has been investigated by many authors, for example [31, 4, 32, 16, 33, 34, 35, 5] and [36]. The Green's functions are usually solved at a conductor surface where the method of moments is applied to obtain a distribution of the surface current density. In Section 3.1 a general approach is used to introduce techniques for avoiding possible numerical problems that may arise when evaluating Sommerfeld-type integrals. Sections 3.2 and 3.3 give a comprehensive analysis of the techniques employed.

3.1 Evaluation of Sommerfeld Integrals

Green's functions and integral equations that arise in layered media problems comprise Sommerfeld-type integrals of the form

$$I = \int_0^\infty \tilde{G}(z, z'; k_\rho) J_\nu(k_\rho \rho) k_\rho dk_\rho, \qquad \nu = 0, 1 \tag{3.1}$$

where $\tilde{G}$ is a spectral domain Green's function of the layered medium, J_ν is a Bessel function of the first type and order ν, ρ is the horizontal distance between the field and source points, and z and z' are the vertical coordinates of those points. These integrals have been extensively investigated and are difficult to evaluate.

From a numerical perspective, two main problems arise when evaluating Sommerfeld-type integrals:

- The possible existence of a singularity in the integrand near the integration path.
- The presence of an oscillatory and slowly convergent integrand, which often diverges

for increasing values of the argument, and which has to be considered over an infinite interval.

By adequately dividing the integration interval, it is always possible to treat the two problems separately.

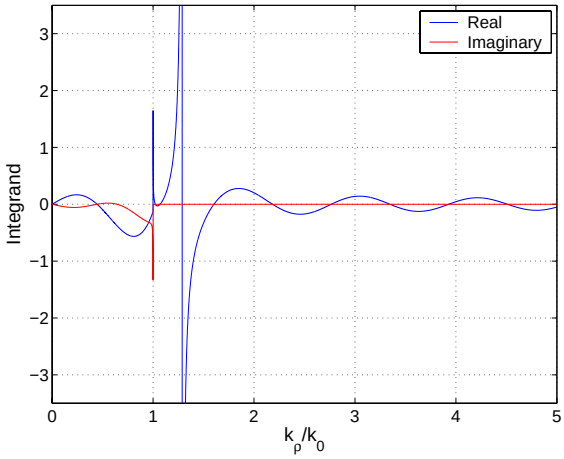

Figure 3.1: The real and imaginary parts of a typical Sommerfeld integrand versus k_ρ/k_0 on the real axis.

As an example, Fig. 3.1 depicts the complex integrand of the Green's function G_Φ for a typical microstrip structure when $z = z' = 0$, $k_\rho\rho = 5.4$, $\mu_r = 1$, $\epsilon_r = 5$ and $k_0 h = 0.2\pi$ where h is the substrate thickness. It can be seen that a discontinuity in the derivative arises in the branch point at $k_\rho = k_0$, and a pole is located at $k_\rho = 1.289k_0$. It is known [5, 23, 24, 33] that for lossless media a number of poles can exist on the real axis between

$$k_0 < k_{\rho,\text{pole}} < k_0\sqrt{\epsilon'_{r,\max}}\,, \tag{3.2}$$

where $\epsilon'_{r,\max}$ is the maximum of the real part of the permittivity of the layers. As the losses increase, the poles migrate away from the real axis into the bottom half of the complex k_ρ plane[1]. In addition, branch cuts can be defined along the loci defined by $\Re(k_z) = 0$. These are shown in Fig. 3.2.

Mosig [16], [33] proposed some techniques for the efficient numerical integration near the poles and branch point. The integration path stays on the real axis for the entire integration process and the poles are extracted numerically. The pole-extraction technique works well for special applications, but in general the number of poles is unknown, and thus the extraction of the poles becomes difficult.

[1]For the $e^{-i\omega t}$ time convention, the Sommerfeld integrals have poles located above (and for lossless media also on) the real axis.

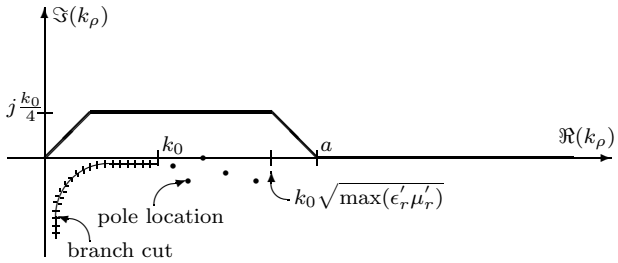

Figure 3.2: Integration path in the complex k_ρ plane.

The approach used more often is to split the infinite interval into two parts $[0, a]$ and $[a, \infty)$. The first path segment is deformed into the first quadrant of the complex plane and the integral is computed using standard quadrature formulas. The value of a is selected to ensure that on the remaining tail segment the integrand is well behaved. Various authors [24, 34, 36] proposed a path that follows a semicircle to avoid the poles and branch points of the integrand. The integration path shown in Fig. 3.2 was suggested by [31]. The integral is computed along 0 to $0.25k_0 + j0.25k_0$, to $k_0\sqrt{\max(\epsilon_r'\mu_r')} + j0.25k_0$, to $k_0\sqrt{\max(\epsilon_r'\mu_r')} + 0.25k_0$, avoiding the singularities in the integrand. Bunger and Arndt [31] state that this path works well even if parallel-plate poles must be considered. As an advantage to the semicircle approach, the distance integrated into the complex plane is reduced. It is difficult to evaluate Bessel functions with large complex arguments [37].

For the subsequent real-axis integration up to infinity, Mosig's method of averages [32] is considered to be the best choice. Since a significant fraction of the overall computational effort is typically spent on the tail integral, it is essential that this integration be done as efficiently as possible. The path stays on the real axis, especially for large values of k_ρ, avoiding the numerical difficulties associated with Bessel functions with large complex arguments. To further increase the rate of convergence, static parts are extracted from the Sommerfeld integral integrands. These two techniques are developed in Sections 3.2 and 3.3 respectively.

It is thus possible to effectively treat the two mentioned problems that arise when evaluating Sommerfeld integrals. To illustrate the effects, Fig. 3.3a shows that, by deforming the integration path into the complex plane, the singularities of Fig. 3.1 have been successfully removed; and Fig. 3.3b highlights the effect of extracting static terms from the oscillatory integrands to increase the rate of convergence.

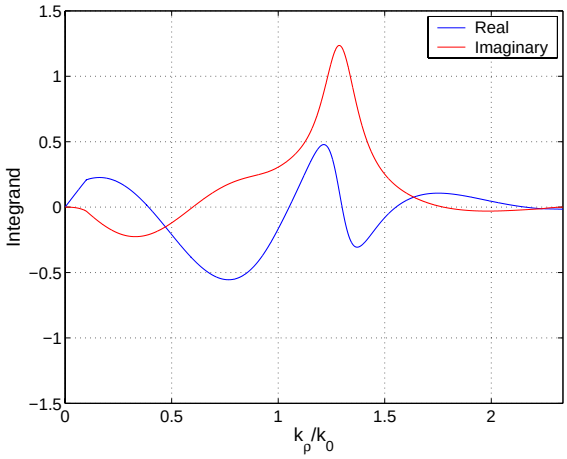

(a) Integration path $[0, a]$ is deformed to avoid poles and branch points of the integrand.

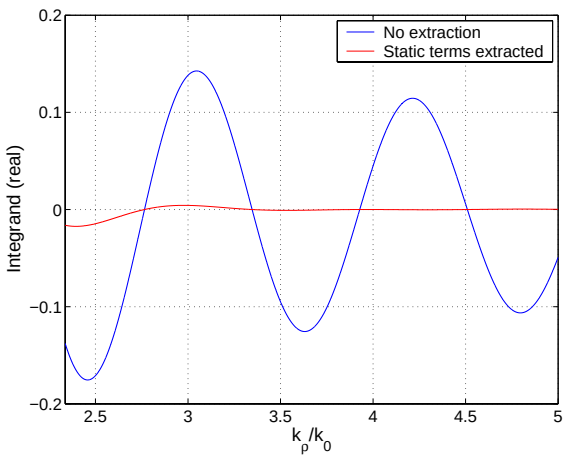

(b) To increase the rate of convergence, static parts are extracted from the integrands.

Figure 3.3: The first path segment $[0, a]$ is deformed into the complex k_ρ plane and the integral is computed using standard quadrature formulas. For the real axis integration up to infinity, static parts are extracted from the integral integrands and Mosig's method of averages is used for an efficient evaluation.

3.2 Method of Averages

The problem of an oscillating integrand over an infinite interval has been extensively investigated and different extrapolation methods for accelerating convergence have been considered [34]. Many approaches, although more efficient than standard numerical integrations, still require too many evaluations of the integrand to obtain adequate convergence. Problems also arise when the integrand itself diverges. A method specifically developed to deal with Sommerfeld integrals is Mosig's method of weighted-averages. The technique will be outlined here with a more complete description given in [32] and [16].

Consider casting integral I in the form

$$I = \int_a^\infty g(\xi\rho) f(\xi) d\xi \tag{3.3}$$

where $g(\xi\rho)$ is a real oscillating function behaving asymptotically as the product of a periodic function and a monotonic function, and $f(\xi)$ is a complex continuous function, which behaves asymptotically as $O(\xi^\alpha)$. When $\alpha > 0$, the function $f(\xi)$ may diverge at infinity and the integral I must be considered in terms of distributions and numerically be evaluated in the mean sense.

In practice, the infinite integration interval must obviously be bounded. Partial values I_m^1

can then be calculated numerically with

$$I_m^1 = \int_a^{\xi_m} \sqrt{\frac{2}{\pi\xi\rho}} \cos(\xi\rho - \nu\pi/2 - \pi/4) f(\xi) d\xi, \qquad m = 1, 2, ..., M. \tag{3.4}$$

Here, $g(\xi\rho)$ is the asymptotic expansion of the Bessel function $J_\nu(\xi\rho)$. The simplest choice of break points are the equidistant points

$$\xi_m = b + mq, \qquad m \geq 0 \tag{3.5}$$

where $q = \pi/\rho$ is the asymptotic half-period of the Bessel function and b denotes the first extremum point of the Bessel function greater than a. In the special case of $\rho = 0$, the subinterval length must be chosen based on the exponential behaviour of the Green's function rather than the oscillations of the Bessel function.

Mosig [32] explains that the sequence of M values I_m^1 oscillates back and forth around the value I, its convergence being determined by the function $f(\xi)$. A new sequence $I_m^2 (m = 1, 2, ..., M-1)$ is then defined by taking a weighted average of two consecutive values of the sequence I_m^1. This new sequence also has an oscillatory behaviour around I, its convergence depending this time on the first derivative $f'(\xi)$. Subsequent averaging produces new sequences I_m^ℓ. Taking into account the asymptotic behaviour of $f(\xi)$, the sequence I_m^ℓ with $\ell > \alpha+1$ is the first one that will converge to the true value I. Successive sequences converge faster, with the last sequence reducing to a single value I_1^M, which will be closer to I than any value I_m^1 in spite of the fact that no new evaluations of the integrand have been required.

For accelerated convergence, the general expression is

$$I_m^{\ell+1} = (w_m^\ell I_m^\ell + w_{m+1}^\ell I_{m+1}^\ell)/(w_m^\ell + w_{m+1}^\ell), \qquad \begin{matrix} \ell = 1, ..., M-1, \\ m = 1, ..., M-\ell \end{matrix} \tag{3.6}$$

in which more weight is given to the values of I_m^1 closest to I. With the optimal value given by

$$w_m^\ell = (\xi_1/\xi_m)^{\alpha+1-\ell}, \tag{3.7}$$

the method of averages is a very efficient technique.

3.3 Static Parts of the Green's Functions

When the source and observation points are located in the same layer or in different, but neighbouring layers, static parts of the Green's functions in the spectral domain

can be extracted. These correspond to the asymptotic terms for $k_\rho \to \infty$, where k_ρ is the spectral variable. In the space domain, the static parts are the singular parts of the Green's functions. The extraction of the static parts from the Sommerfeld integral integrands increases the convergence of the integrals and yields regular results in the space domain [31].

When the source and observation points are located in the same layer, $m = n$, the first three largest asymptotic terms are extracted in the spectral domain. In the space domain, these static terms represent the direct part, and two images at the upper and lower interfaces. When the source and observation points are located in adjacent layers, $|n - m| = 1$, only the largest asymptotic terms are extracted. In this case there are no image terms. The extracted static parts in the spectral domain are transformed into the space domain analytically by using the Sommerfeld identity (Eqn. 2.11)

$$\int_C J_0(k_\rho \rho) \frac{k_\rho}{jk_z} e^{-jk_z|z|} dk_\rho = \frac{e^{-jkr}}{r}, \tag{3.8}$$

where C is a path from 0 to ∞, and the relation

$$\int_0^\infty J_1(k_\rho \rho) e^{-jk_z|z|} dk_\rho = \frac{1}{\rho} e^{-jk|z|} - \frac{|z|}{\rho r} e^{-jkr}. \tag{3.9}$$

which may be derived by integration by parts[2].

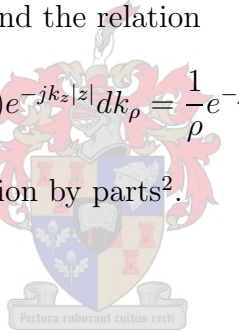

Evaluation of G_Φ

When $|n - m| > 1$, the observation and source points are located in different, non-neighbouring layers and no static terms are extracted. For the scalar potential associated with an HED, the Sommerfeld integral is that given in Eqn. 2.58.

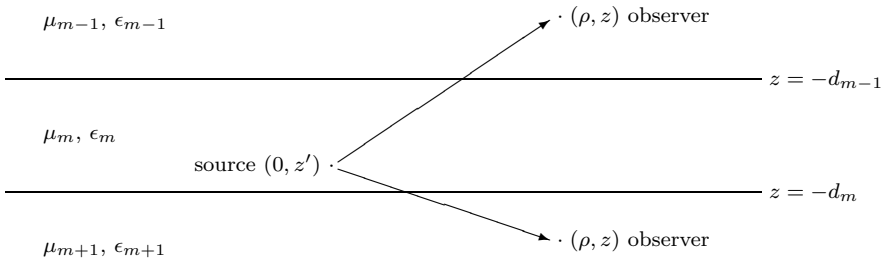

Figure 3.4: Source and observer in adjacent layers.

[2]There is a typing error in [31, Eqn. 21]

When $|n-m|=1$, the observer and source points are located in adjacent layers. To reduce the computational effort in the Sommerfeld integral, the largest asymptotic term can be extracted [31]. As is shown in Fig. 3.4, this represents the direct part in the space domain.

From Eqn. 2.58, extract the static term that corresponds to the direct transmitted wave

$$\begin{aligned} G_\Phi = \frac{I\ell}{4\pi\epsilon_n}\Bigg[\int_0^\infty J_0(k_\rho\rho)\Big[\frac{1}{k_\rho}\frac{\partial}{\partial z}F_{E_z}^{HED} + \frac{k_n^2}{jk_{mz}k_\rho}F_{H_z}^{HED}\frac{\mu_m}{\mu_n} \\ - \lim_{k_\rho\to\infty}\Big(\frac{1}{k_\rho}T_J^{TM,\infty}(\mp jk_{iz})(\mp e^{-jk_{iz}|z-z'|}) + \frac{k_n^2}{jk_{iz}k_\rho}T_J^{TE,\infty}e^{-jk_{iz}|z-z'|}\Big) \\ + \lim_{k_\rho\to\infty}\Big(\frac{1}{k_\rho}T_J^{TM,\infty}(\mp jk_{iz})(\mp e^{-jk_{iz}|z-z'|}) + \frac{k_n^2}{jk_{iz}k_\rho}T_J^{TE,\infty}e^{-jk_{iz}|z-z'|}\Big)\Big]dk_\rho\Bigg]. \end{aligned} \tag{3.10}$$

In the above equation, k_i can be interpreted as the propagation constant of an equivalent homogeneous medium that has the same asymptotic behaviour as the two-layered medium Green's function in concern. In the relation $k_{iz}^2 = k_i^2 - k_\rho^2$, k_i has the value

$$k_i = 0.5[\Re(k_m)+\Re(k_n)] + j\min[\Im(k_m),\Im(k_n)].^3 \tag{3.11}$$

Also, in the limit $k_\rho\to\infty$, the transmission coefficients are defined as

$$\begin{aligned} T_J^{TM,\infty} &= \frac{2\epsilon_n}{\epsilon_n+\epsilon_m} \\ T_J^{TE,\infty} &= \frac{2\mu_m}{\mu_n+\mu_m}. \end{aligned} \tag{3.12}$$

When applying boundary conditions for a PEC between layers m and n, the transmission coefficients evaluate to $T_J^{TM,\infty}=2$ and $T_J^{TE,\infty}=0$. Note that even though $T_J^{TM,\infty}=2$ on the interface, all fields in a conductor are subject to an exponential decay resulting in a zero field just beyond the PEC.

Now, the static parts of the Green's function in the spectral domain are the asymptotic terms for $k_\rho\to\infty$. In the limit,

$$\lim_{k_\rho\to\infty}\frac{k_{iz}}{k_\rho} = \lim_{k_\rho\to\infty}\frac{k_\rho}{k_{iz}}\Big(\frac{k_i^2-k_\rho^2}{k_\rho^2}\Big) = -\frac{k_\rho}{k_{iz}} \tag{3.13}$$

and

$$\lim_{k_\rho\to\infty}\frac{k_n^2}{k_{iz}k_\rho} = 0. \tag{3.14}$$

Thus, the integral in Eqn. 3.10 can be simplified and written as

$$\begin{aligned} G_\Phi = \frac{I\ell}{4\pi\epsilon_n}\Bigg[T_J^{TM,\infty}\frac{e^{-jk_ir}}{r} + \int_0^\infty J_0(k_\rho\rho)\Big(\frac{1}{k_\rho}\frac{\partial}{\partial z}F_{E_z}^{HED} \\ + \frac{k_n^2}{jk_{mz}k_\rho}F_{H_z}^{HED}\frac{\mu_m}{\mu_n} - T_J^{TM,\infty}e^{-jk_{iz}|z-z'|}\frac{k_\rho}{jk_{iz}}\Big)dk_\rho\Bigg]. \end{aligned} \tag{3.15}$$

[3] For the $e^{-i\omega t}$ time convention $k_i = 0.5[\Re(k_m)+\Re(k_n)] + j\max[\Im(k_m),\Im(k_n)]$

In the last step the extracted static part in the spectral domain was transformed into the space domain analytically by using the Sommerfeld identity Eqn. 3.8. $F_{E_z}^{HED}$ and $F_{H_z}^{HED}$ are given by Eqn. 2.22 when $n < m$ and by Eqn. 2.26 when $n > m$.

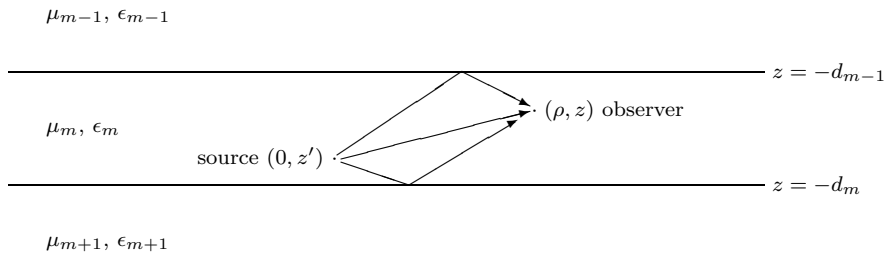

Figure 3.5: Source and observer in the same layer.

When the observation and source layers are the same, or $n = m$, the first three largest asymptotic terms are extracted in the spectral domain. These terms represent the direct part, and two images at the upper and lower interfaces. This is shown in Fig. 3.5.

The extracted static term corresponding to the direct part of the Green's function in the spatial domain can be expressed in closed form. This is done by substitution of the direct terms of Eqn. 2.16 into Eqn. 2.58, and applying the Sommerfeld transform identity. This gives the direct term as

$$\begin{aligned} G_\Phi^D &= \frac{I\ell}{4\pi\epsilon_m} \lim_{k_\rho \to \infty} \int_0^\infty J_0(k_\rho \rho) \Big(\frac{jk_{mz}}{k_\rho} + \frac{k_m^2}{jk_{mz}k_\rho} \Big) e^{-jk_{mz}|z-z'|} dk_\rho \\ &= \frac{I\ell}{4\pi\epsilon_m} \int_0^\infty J_0(k_\rho \rho) \frac{k_\rho}{jk_{mz}} e^{-jk_{mz}|z-z'|} dk_\rho \\ &= \frac{I\ell}{4\pi\epsilon_m} \frac{e^{-jk_m r}}{r}. \end{aligned} \tag{3.16}$$

To include the contribution from the top and bottom layers, i.e., the images of the source in the plane $z = -d_{m-1}$ and the plane $z = -d_m$, define the origin of the z-axis in Fig. 2.1 as $z = -d_1 = 0$ and

$$\begin{aligned} r &= \sqrt{\rho^2 + (z - z')^2} \\ r_1 &= \sqrt{\rho^2 + s_1^2} \qquad & s_1 &= -2d_{m-1} - (z + z') \\ r_2 &= \sqrt{\rho^2 + s_2^2} \qquad & s_2 &= 2d_m + (z + z'). \end{aligned} \tag{3.17}$$

Also, the reflection coefficients associated with the image parts can be written as

$$\begin{aligned} R_{m,m-1}^{TE,\infty} &= \frac{\mu_{m-1} - \mu_m}{\mu_{m-1} + \mu_m} \qquad & R_{m,m+1}^{TE,\infty} &= \frac{\mu_{m+1} - \mu_m}{\mu_{m+1} + \mu_m} \\ R_{m,m-1}^{TM,\infty} &= \frac{\epsilon_{m-1} - \epsilon_m}{\epsilon_{m-1} + \epsilon_m} \qquad & R_{m,m+1}^{TM,\infty} &= \frac{\epsilon_{m+1} - \epsilon_m}{\epsilon_{m+1} + \epsilon_m} \end{aligned} . \tag{3.18}$$

Note that these should not be mistaken for the Fresnel coefficients of Eqns. 2.20 and 2.21. In the limit $k_\rho \to \infty$ the Fresnel coefficient reduce to those associated with the image terms. When a PEC is bounding the layer in concern, the reflection coefficients are $R^{TE,\infty} = -1$ and $R^{TM,\infty} = 1$.

Hence, the solution for the Green's function of the scalar potential is

$$\begin{aligned} G_\Phi = \frac{I\ell}{4\pi\epsilon_m}\Bigg[&\frac{e^{-jk_m r}}{r} - R^{TM,\infty}_{m,m-1}\frac{e^{-jk_m r_1}}{r_1} - R^{TM,\infty}_{m,m+1}\frac{e^{-jk_m r_2}}{r_2} \\ &+ \int_0^\infty J_0(k_\rho\rho)\Big(\frac{1}{k_\rho}\frac{\partial}{\partial z}F^{HED}_{E_z} + \frac{k_m^2}{jk_{mz}k_\rho}F^{HED}_{H_z} \\ &+ R^{TM,\infty}_{m,m-1}e^{-jk_{mz}s_1}\frac{k_\rho}{jk_{mz}} + R^{TM,\infty}_{m,m+1}e^{-jk_{mz}s_2}\frac{k_\rho}{jk_{mz}}\Big)dk_\rho\Bigg]. \end{aligned} \tag{3.19}$$

Note the presence of the singularity in the analytic direct and image parts of the Green's function. Also, similar to the situation where the observation and source points were located in contiguous layers, the TE form of the asymptotic terms reduced to zero. Finally, $F^{HED}_{E_z}$ and $F^{HED}_{H_z}$ are given by Eqn. 2.16 (without the direct terms),

$$\begin{aligned} F^{HED}_{E_z} &= B^{TM,HED}_m e^{jk_{mz}z} + D^{TM,HED}_m e^{-jk_{mz}z} \\ F^{HED}_{H_z} &= B^{TE,HED}_m e^{jk_{mz}z} + D^{TE,HED}_m e^{-jk_{mz}z}. \end{aligned} \tag{3.20}$$

Extracting the static parts of the Green's functions in the spectral domain increases convergence of the Sommerfeld integral tails and yield very smooth results in the space domain.

Evaluation of G^{xx}_A

With the observation and source points separated by one or more layers, $|n-m| > 1$, the spatial domain Green's function is given by Eqn. 2.59.

When the observer and source are in adjacent layers, $|n-m| = 1$, as shown in Fig. 3.4, the integral can be written as

$$G^{xx}_A = \frac{\mu_n I\ell}{4\pi}\left[T^{TE,\infty}_J\frac{e^{-jk_i r}}{r} + \int_0^\infty J_0(k_\rho\rho)k_\rho\Big(\frac{F^{HED}_{H_z}}{jk_{mz}}\frac{\mu_m}{\mu_n} - \frac{T^{TE,\infty}_J}{jk_{iz}}e^{-jk_{iz}|z-z'|}\Big)dk_\rho\right], \tag{3.21}$$

where $F^{HED}_{H_z}$ is given by either Eqn. 2.22 or 2.26. The first term in the above equation corresponds to the direct transmitted space domain wave solution.

With $m = n$, the source and observation points are in the same layer. This is shown in Fig. 3.5. Substituting the direct term, $e^{-jk_{mz}|z-z'|}$, of Eqn. 2.16 into Eqn. 2.59 and using

the Sommerfeld identity, the analytical form of the space domain direct term is

$$G_A^{xx,D} = \frac{\mu_m I\ell}{4\pi}\int_0^\infty J_0(k_\rho\rho)\frac{k_\rho}{jk_{mz}}e^{-jk_{mz}|z-z'|}dk_\rho = \frac{\mu_m I\ell}{4\pi}\frac{e^{-jk_m r}}{r}. \tag{3.22}$$

Including the contribution of the two images at the upper and lower interfaces, G_A^{xx} is finally given by

$$\begin{aligned} G_A^{xx} = \frac{\mu_m I\ell}{4\pi}\Bigg[&\frac{e^{-jk_m r}}{r} + R_{m,m-1}^{TE,\infty}\frac{e^{-jk_m r_1}}{r_1} + R_{m,m+1}^{TE,\infty}\frac{e^{-jk_m r_2}}{r_2} \\ &+ \int_0^\infty J_0(k_\rho\rho)\frac{k_\rho}{jk_{mz}}\Big(F_{H_z}^{HED} - R_{m,m-1}^{TE,\infty}e^{-jk_{mz}s_1} - R_{m,m+1}^{TE,\infty}e^{-jk_{mz}s_2}\Big)dk_\rho\Bigg]. \end{aligned} \tag{3.23}$$

Here $F_{H_z}^{HED}$ is given by Eqn. 2.16, but without the direct term.

Evaluation of G_A^{zx}

When the observation and source layers satisfy the relation $|n-m| > 1$, the Green's function is given by Eqn. 2.60.

When the observer and source are in adjacent layers, $|n-m| = 1$, the integral can be written as

$$\begin{aligned} G_A^{zx} = \frac{\mu_n I\ell}{4\pi}\cos\phi\Bigg[&-\text{sign}(z-z')(T_J^{TE,\infty} - T_J^{TM,\infty})\Big(\frac{1}{\rho}e^{-jk_i|z-z'|} - \frac{|z-z'|}{\rho r}e^{-jk_i r}\Big) \\ &+ \int_0^\infty J_1(k_\rho\rho)\Big(-F_{E_z}^{HED} + \frac{1}{jk_{mz}}\frac{\partial}{\partial z}F_{H_z}^{HED}\frac{\mu_m}{\mu_n} \\ &+ \text{sign}(z-z')(T_J^{TE,\infty} - T_J^{TM,\infty})e^{-jk_{iz}|z-z'|}\Big)dk_\rho\Bigg]. \end{aligned} \tag{3.24}$$

In the above the extracted static parts in the spectral domain are transformed into the space domain by using the analytical solution of Eqn. 3.9. $F_{E_z}^{HED}$ and $F_{H_z}^{HED}$ are given by either Eqn. 2.22 or 2.26.

With $n = m$, as shown in Fig. 3.5, and substituting the direct term of Eqn. 2.16 into Eqn. 2.60 gives

$$G_A^{zx,D} = \pm\frac{\mu_m I\ell}{4\pi}\cos\phi\int_0^\infty J_1(k_\rho\rho)\Big(1 + \frac{j}{k_{mz}}jk_{mz}\Big)e^{-jk_{mz}|z-z'|}dk_\rho = 0. \tag{3.25}$$

This means that the largest static term representing the direct part is zero. Extracting

the asymptotic terms contributed from the upper and lower layers,

$$\begin{aligned} G_A^{zx} = \frac{\mu_m I\ell}{4\pi}\cos\phi\Bigg[&(R_{m,m-1}^{TM,\infty}+R_{m,m-1}^{TE,\infty})\Big(\frac{1}{\rho}e^{-jk_m s_1}-\frac{s_1}{\rho r_1}e^{-jk_m r_1}\Big)\\ &-(R_{m,m+1}^{TM,\infty}+R_{m,m+1}^{TE,\infty})\Big(\frac{1}{\rho}e^{-jk_m s_2}-\frac{s_2}{\rho r_2}e^{-jk_m r_2}\Big)\\ &+\int_0^\infty J_1(k_\rho\rho)\Big(-F_{E_z}^{HED}+\frac{1}{jk_{mz}}\frac{\partial}{\partial z}F_{H_z}^{HED}-(R_{m,m-1}^{TM,\infty}+R_{m,m-1}^{TE,\infty})e^{-jk_{mz}s_1}\\ &+(R_{m,m+1}^{TM,\infty}+R_{m,m+1}^{TE,\infty})e^{-jk_{mz}s_2}\Big)dk_\rho\Bigg]. \end{aligned} \tag{3.26}$$

$F_{E_z}^{HED}$ and $F_{H_z}^{HED}$ are given by Eqn. 2.16, but without the direct terms, i.e.,

$$\begin{aligned} F_{E_z}^{HED} &= B_m^{TM,HED}e^{jk_{mz}z}+D_m^{TM,HED}e^{-jk_{mz}z}\\ F_{H_z}^{HED} &= B_m^{TE,HED}e^{jk_{mz}z}+D_m^{TE,HED}e^{-jk_{mz}z}. \end{aligned} \tag{3.27}$$

Evaluation of K_A^{xz}

Eqn. 2.62 was developed in Section 2.6 to describe the Green's function of K_A^{xz} when the observation and source points are located in different non-adjacent layers, $|n-m|>1$.

For the observer and source in neighbouring layers, $|n-m|=1$,

$$\begin{aligned} K_A^{xz} = \frac{\mu_n I\ell}{4\pi}\cos\phi\Bigg[&-\mathrm{sign}(z-z')(T_J^{TE,\infty}-\frac{k_m^2}{k_n^2}T_J^{TM,\infty})\Big(\frac{1}{\rho}e^{-jk_i|z-z'|}-\frac{|z-z'|}{\rho r}e^{-jk_i r}\Big)\\ &+\int_0^\infty J_1(k_\rho\rho)\Big(\frac{j}{k_{mz}}\frac{k_m^2}{k_n^2}\frac{\partial}{\partial z}F_{E_z}^{VED}+\frac{j}{k_{mz}}\frac{\partial}{\partial z'}F_{H_z}^{HED}\frac{\mu_m}{\mu_n}\\ &+\mathrm{sign}(z-z')(T_J^{TE,\infty}-\frac{k_m^2}{k_n^2}T_J^{TM,\infty})e^{-jk_{iz}|z-z'|}\Big)dk_\rho\Bigg]. \end{aligned} \tag{3.28}$$

Extraction of the static term corresponding to the direct wave in the spatial domain, result in $K_A^{xz,D}=0$. For the source and observer in the same layer, $m=n$, and including the contribution from the image of the source in the planes $z=-d_{m-1}$ and $z=-d_m$, K_A^{xz} is finally given by

$$\begin{aligned} K_A^{xz} = \frac{\mu_m I\ell}{4\pi}\cos\phi\Bigg[&-(R_{m,m-1}^{TM,\infty}+R_{m,m-1}^{TE,\infty})\Big(\frac{1}{\rho}e^{-jk_m s_1}-\frac{s_1}{\rho r_1}e^{-jk_m r_1}\Big)\\ &+(R_{m,m+1}^{TM,\infty}+R_{m,m+1}^{TE,\infty})\Big(\frac{1}{\rho}e^{-jk_m s_2}-\frac{s_2}{\rho r_2}e^{-jk_m r_2}\Big)\\ &+\int_0^\infty J_1(k_\rho\rho)\Big(\frac{j}{k_{mz}}\frac{\partial}{\partial z}F_{E_z}^{VED}+\frac{j}{k_{mz}}\frac{\partial}{\partial z'}F_{H_z}^{HED}\\ &+(R_{m,m-1}^{TM,\infty}+R_{m,m-1}^{TE,\infty})e^{-jk_{mz}s_1}-(R_{m,m+1}^{TM,\infty}+R_{m,m+1}^{TE,\infty})e^{-jk_{mz}s_2}\Big)dk_\rho\Bigg]. \end{aligned} \tag{3.29}$$

$F_{E_z}^{VED}$ and $F_{H_z}^{HED}$ are given by Eqn. 2.16, once again without the direct term, $e^{-jk_{mz}|z-z'|}$.

Evaluation of K_A^{zz}

When the observation and source layers are separated by at least one other medium, $|n-m|>1$, K_A^{zz} is given by Eqn. 2.63.

When the observer and source are in adjacent layers, $|n-m|=1$,

$$\begin{aligned} K_A^{zz} = \frac{\mu_n I\ell}{4\pi}\Bigg[& -\Big(T_J^{TE,\infty} - (\frac{k_m^2}{k_n^2}+1)T_J^{TM,\infty}\Big)\frac{e^{-jk_i r}}{r} \\ & - \int_0^\infty J_0(k_\rho\rho)\Big[j\Big(\frac{k_\rho}{k_{mz}}\frac{k_m^2}{k_n^2} - \frac{k_{mz}}{k_\rho}\Big)F_{E_z}^{VED} + \frac{j}{k_{mz}k_\rho}\frac{\partial^2}{\partial z'\partial z}F_{H_z}^{HED}\frac{\mu_m}{\mu_n} \\ & + \Big(T_J^{TE,\infty} - (\frac{k_m^2}{k_n^2}+1)T_J^{TM,\infty}\Big)e^{-jk_{iz}|z-z'|}\frac{jk_\rho}{k_{iz}}\Big]dk_\rho\Bigg], \end{aligned} \tag{3.30}$$

where $F_{E_z}^{VED}$ and $F_{H_z}^{HED}$ are given by Eqn. 2.22 or 2.26.

With the observation and source points in the same layer, $n=m$, the extraction of the three largest asymptotic terms in the spectral domain, gives

$$\begin{aligned} K_A^{zz} = \frac{\mu_m I\ell}{4\pi}\Bigg[& \frac{e^{-jk_m r}}{r} + \Big(R_{m,m-1}^{TE,\infty} + 2R_{m,m-1}^{TM,\infty}\Big)\frac{e^{-jk_m r_1}}{r_1} \\ & + \Big(R_{m,m+1}^{TE,\infty} + 2R_{m,m+1}^{TM,\infty}\Big)\frac{e^{-jk_m r_2}}{r_2} \\ & - \int_0^\infty J_0(k_\rho\rho)\Big[j\Big(\frac{k_\rho}{k_{mz}} - \frac{k_{mz}}{k_\rho}\Big)F_{E_z}^{VED} + \frac{j}{k_{mz}k_\rho}\frac{\partial^2}{\partial z'\partial z}F_{H_z}^{HED} \\ & - \Big(R_{m,m-1}^{TE,\infty} + 2R_{m,m-1}^{TM,\infty}\Big)e^{-jk_{mz}s_1}\frac{jk_\rho}{k_{mz}} \\ & - \Big(R_{m,m+1}^{TE,\infty} + 2R_{m,m+1}^{TM,\infty}\Big)e^{-jk_{mz}s_2}\frac{jk_\rho}{k_{mz}}\Big]dk_\rho\Bigg]. \end{aligned} \tag{3.31}$$

As before, $F_{E_z}^{VED}$ and $F_{H_z}^{HED}$ are given by Eqn. 2.16, but without the direct term.

The principles used in extracting static terms were explained in developing the Green's function components for the scalar and dyadic vector potentials G_Φ and $\bar{\bar{\mathbf{K}}}_A$. Green's functions for the electric potentials may be obtained using duality and results are included in Appendix F.

3.4 Conclusion

In this chapter the Green's functions for an arbitrary directed dipole embedded in multi-layered media were evaluated. In Section 3.1 possible numerical integration paths were considered. The path selected to compute the Green's functions, is that suggested by [31]

and was chosen specifically to avoid the singularities in the integrand. In Section 3.2 an extrapolation method of the Sommerfeld integral tails was investigated. Mosig's method of averages was found to be efficient and fast in convergence. Finally, Section 3.3 discussed the treatment of extracting static terms from Sommerfeld integral integrands to further increase convergence.

Chapter 4

Method of Moments

This Chapter develops a Method of Moments (MoM) technique to analyse arbitrary shaped objects, buried in multi-layered media. The objects are modelled using planar triangular surface patches that are not allowed to cross the interface between adjacent layers. Triangular basis functions have the ability to conform readily to arbitrary geometries, giving an accurate discretisation. The MoM formulation extends the one originally described by Rao, Wilton and Glisson [11]. This particular formulation has been investigated by many authors and is well documented in the literature. Examples are [24], [13], [38], [39], [40] and [41].

The Rao, Wilton and Glisson formulation uses the well-known free-space Green's function. Section 4.5 extends this scalar formulation to its dyadic counterpart and includes Green's functions of an arbitrary directed electric and magnetic dipole located in a multi-layered medium. These Green's functions were derived in Chapters 2 and 3. The scheme used for packing the $\bar{\bar{Z}}$ matrix is similar to the one introduced by Van Tonder [24], but with the difference that multiple problems, stacked and separated by a PEC, can be solved simultaneously. The filling algorithm also efficiently packs partially symmetric matrices, which are present when solving problems that support a combination of electric and magnetic currents. When the source and observer points coincide, the Green's functions are singular. The analytical integration procedure handling this case, is described in Appendix D.

The Method of Moments (MoM) is a solution procedure for approximating an integral equation, such as

$$\mathbf{E}(\mathbf{r}) = \int_S \bar{\bar{\mathbf{G}}}(\mathbf{r}, \mathbf{r}') \cdot \mathbf{J}_s(\mathbf{r}') dS', \tag{4.1}$$

with a system of simultaneous linear algebraic equations in terms of the unknown current

distribution $\mathbf{J}_s$, which may be approximated with a series of basis functions $\mathbf{f}_n$

$$\mathbf{J}_s(\mathbf{r}') = \sum_{n=1}^{N} I_n \mathbf{f}_n(\mathbf{r}'). \tag{4.2}$$

On substituting Eqn. 4.2 into Eqn. 4.1, a single equation with N unknowns is obtained

$$\mathbf{E}(\mathbf{r}) = \int_S \bar{\bar{\mathbf{G}}}(\mathbf{r},\mathbf{r}') \cdot \sum_{n=1}^{N} I_n \mathbf{f}_n(\mathbf{r}') dS' = \sum_{n=1}^{N} I_n \int_S \bar{\bar{\mathbf{G}}}(\mathbf{r},\mathbf{r}') \cdot \mathbf{f}_n(\mathbf{r}') dS'. \tag{4.3}$$

To obtain a set of N independent equations, a method of weighted residuals is enforced to give

$$\int_S \mathbf{E}(\mathbf{r}) \cdot \mathbf{g}_m(\mathbf{r}) dS = \sum_{n=1}^{N} I_n \Big(\int_S \int_S \bar{\bar{\mathbf{G}}}(\mathbf{r},\mathbf{r}') \cdot \mathbf{f}_n(\mathbf{r}') \cdot \mathbf{g}_m(\mathbf{r}) dS' dS \Big), \qquad m = 1, 2, ..., N, \tag{4.4}$$

where $\mathbf{g}_m$ is called the weighting/testing function. This set of N linear equations yield the standard MoM system equation

$$[Z_{mn}][I_n] = [V_m]. \tag{4.5}$$

4.1 Problems involving both Electric and Magnetic Sources

In the standard MoM formulation, the presence of a slot in an infinite electrical conductor would require discretisation of a finite size ground plane that surrounds the gap. In the MoM formulation presented in this chapter, both electric and magnetic sources are supported. This allows discretisation of the slot interface only.

Consider Fig. 4.1. Let S_1 and S_2 denote the surface of open or closed perfectly conducting scatterers with unit normal $\hat{\mathbf{n}}$. Similarly, S_3 consists of a finite aperture in an infinite electrical ground plane. An electric field $\mathbf{E}_1^i$ and a magnetic field $\mathbf{H}_1^i$, defined to be the fields due to an impressed source in the absence of the electric scatterer and the dielectric interface, are incident on and induce surface currents $\mathbf{J}_{s_1}$ on S_1 and $\mathbf{M}_s$ on S_3. Similarly, $\mathbf{E}_2^i$ and $\mathbf{H}_2^i$ induce surface currents $\mathbf{J}_{s_2}$ on S_2 and $\mathbf{M}_s$ on S_3.

The scattered electric field $\mathbf{E}^s$ can be computed from the potentials by

$$\mathbf{E}^s = -j\omega\mathbf{A} - \nabla\Phi - \frac{1}{\epsilon}\nabla \times \mathbf{F}. \tag{4.6}$$

Similarly, by using the duality principle, the scattered magnetic field $\mathbf{H}^s$ is given by

$$\mathbf{H}^s = -j\omega\mathbf{F} - \nabla\Psi + \frac{1}{\mu}\nabla \times \mathbf{A}. \tag{4.7}$$

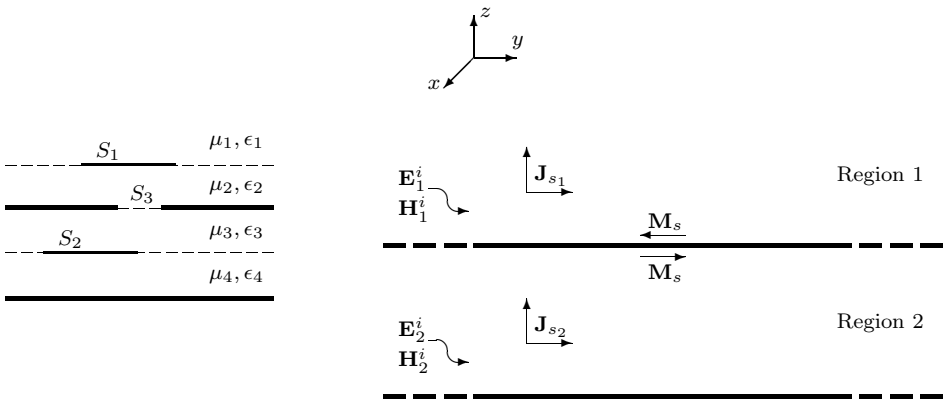

Figure 4.1: Geometry of a general multi-layered medium containing both conducting strips and slots in conducting sheets. The figure on the right shows the equivalent mathematical configuration. Electric surface currents $\mathbf{J}_{s_1}$ and $\mathbf{J}_{s_2}$ are induced on conducting scatterers S_1 and S_2 in Regions 1 and 2 respectively. Magnetic surface currents $\mathbf{M}_s$ are induced on the dielectric interface S_3 defined between Regions 1 and 2.

In the above two equations $\mathbf{A}$ and Φ are the magnetic vector and electric scalar potentials respectively; and $\mathbf{F}$ and Ψ are the electric vector and magnetic scalar potentials.

In the combined field integral equation the tangential electric and magnetic fields are proportional to the total surface currents. Assuming conductor losses to be negligible, the total tangential electric field, i.e. the sum of the incident and scattered fields, is forced to be zero on S_1 and S_2. Also, the total tangential magnetic field should be continuous across the dielectric interface S_3. This requires the magnetic surface current $\mathbf{M}_s$ to be oppositely directed in Regions 1 and 2 on the interface S_3. To ensure field coupling between surfaces S_1, S_2 and S_3 (i.e. also between Regions 1 and 2), it is necessary and sufficient to enforce these two boundary conditions

$$\begin{aligned} \hat{\mathbf{n}} \times (\mathbf{E}_1^i + \mathbf{E}_1^s) &= 0 && \text{on } S_1 \\ \hat{\mathbf{n}} \times (\mathbf{E}_2^i + \mathbf{E}_2^s) &= 0 && \text{on } S_2 \\ \hat{\mathbf{n}} \times (\mathbf{H}_1^i + \mathbf{H}_1^s) &= \hat{\mathbf{n}} \times (\mathbf{H}_2^i + \mathbf{H}_2^s) && \text{on } S_3. \end{aligned} \tag{4.8}$$

Introducing the potentials, the general formulation is obtained

$$\begin{aligned} \hat{\mathbf{n}} \times \mathbf{E}_1^i &= \hat{\mathbf{n}} \times (j\omega\mathbf{A}_1 + \nabla\Phi_1 + \nabla \times \frac{\mathbf{F}_1}{\epsilon_1}) && \text{on } S_1 \\ \hat{\mathbf{n}} \times \mathbf{E}_2^i &= \hat{\mathbf{n}} \times (j\omega\mathbf{A}_2 + \nabla\Phi_2 + \nabla \times \frac{\mathbf{F}_2}{\epsilon_2}) && \text{on } S_2 \\ \hat{\mathbf{n}} \times (\mathbf{H}_1^i - \mathbf{H}_2^i) &= \hat{\mathbf{n}} \times \big(j\omega(\mathbf{F}_1 - \mathbf{F}_2) + \nabla\Psi_1 - \nabla\Psi_2 - \nabla \times (\frac{\mathbf{A}_1}{\mu_1} - \frac{\mathbf{A}_2}{\mu_2})\big) && \text{on } S_3. \end{aligned} \tag{4.9}$$

Note that by using the equivalence principle the structure geometry was effectively separated into two problems. These were called Regions 1 and 2 and are solved independently. Coupling is obtained only when continuity of the magnetic surface currents is enforced at the slotline interfaces.

The integral equations defining the vector and scalar potentials were derived in Chapter 2. For convenience these results are repeated. The magnetic vector and electric scalar potentials are

$$\begin{aligned} \mathbf{A}(\mathbf{r}) &= \int_S \bar{\bar{\mathbf{K}}}_A(\mathbf{r}|\mathbf{r}') \cdot \mathbf{J}_s(\mathbf{r}') dS' \\ \Phi(\mathbf{r}) &= \int_S G_\Phi(\mathbf{r}|\mathbf{r}') q_s(\mathbf{r}') dS' \end{aligned} \tag{4.10}$$

and the dual potentials are

$$\begin{aligned} \mathbf{F}(\mathbf{r}) &= \int_S \bar{\bar{\mathbf{K}}}_F(\mathbf{r}|\mathbf{r}') \cdot \mathbf{M}_s(\mathbf{r}') dS' \\ \Psi(\mathbf{r}) &= \int_S G_\Psi(\mathbf{r}|\mathbf{r}') q_{ms}(\mathbf{r}') dS' \end{aligned} \tag{4.11}$$

where S may now be extended to either S_1, S_2 or S_3.

4.2 Development of Basis Functions

Rao, Wilton and Glisson introduced a set of basis functions suitable for use with the electric field MPIE and triangular patch modelling. Crucial to the construction of such vector basis functions was that their normal components should be continuous across surface edges and that it should be free of fictitious line or point charges. This section outlines the basis functions as presented in [11].

Each basis function is to be associated with an interior or non-boundary edge of the patch model and is to vanish everywhere except on the two triangles attached to the edge. Fig. 4.2 shows two such triangles, T_v^+ and T_v^-, corresponding to the v^{th} edge of a triangulated surface modelling a scatterer. Points in T_v^+ may be designated either by the position vector $\mathbf{r}$ defined with respect to O, or by the position vector $\boldsymbol{\varrho}_v^+$ defined with respect to the free vertex of T_v^+. Similar remarks apply to the position vector $\boldsymbol{\varrho}_v^-$ except that it is directed towards the free vertex of T_v^-. The plus or minus designation of the triangles is determined by the choice of a positive current reference direction for the v^{th} edge, the reference for which is assumed to be from T_v^+ to T_v^-.[1] Superscripts $c+$ and $c-$

[1]The current reference direction may be obtained from the connection matrix used to describe the

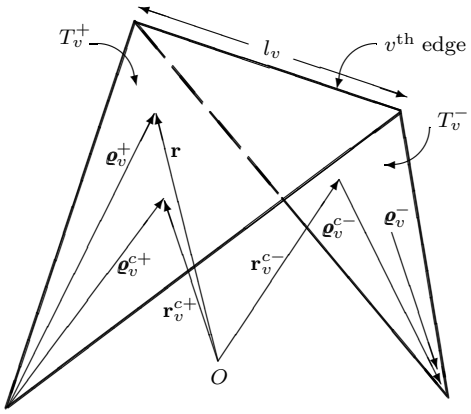

Figure 4.2: Vector dependence of a triangular-domain interior edge.

denote the centroid of each triangle. Define the vector basis function associated with the v^{th} edge as

$$\mathbf{f}_v(\mathbf{r}) = \begin{cases} \frac{l_v}{2A_v^+}\boldsymbol{\varrho}_v^+ & \mathbf{r} \text{ in } T_v^+ \\ \frac{l_v}{2A_v^-}\boldsymbol{\varrho}_v^- & \mathbf{r} \text{ in } T_v^- \\ 0 & \text{otherwise} \end{cases} \tag{4.12}$$

where l_v is the length of the edge and $A_v^\pm$ is the area of triangle $T_v^\pm$ (subscripts refer to edges while superscripts refer to faces). The basis function $\mathbf{f}_v$ is used to approximate the surface current, and listed are some of the properties that uniquely contribute to this.

- The current has no component normal to the boundary (which excludes the common edge) of the surface formed by the triangle pair $T_v^\pm$, and hence no line charges exist along this boundary.
- The component of current normal to the v^{th} edge is constant and continuous across the edge, ensuring that all edges of $T_v^\pm$ are free of line charges.
- The surface divergence of $\mathbf{f}_v$, which is proportional to the surface charge density associated with the basis element, is

$$\nabla \cdot \mathbf{f}_v(\mathbf{r}) = \begin{cases} \frac{l_v}{A_v^+} & \mathbf{r} \text{ in } T_v^+ \\ -\frac{l_v}{A_v^-} & \mathbf{r} \text{ in } T_v^- \\ 0 & \text{otherwise.} \end{cases} \tag{4.13}$$

  The charge density is thus constant in each triangle, the total charge associated with the triangle pair is zero and the basis functions for the charge have the form of pulse

---

triangulation scheme. This matrix merely lists the triangles associated with each edge, the order of appearance effectively assigning an orientation to the edge.

doublets.

The vector basis function stated in Eqn. 4.12 is ideally suited for representing both the surface electric current $\mathbf{J}_s$ and the surface magnetic current $\mathbf{M}_s$ on the triangulated surfaces. Thus the current on S_1 and S_2 may be approximated in terms of $\mathbf{f}_v$ as

$$\begin{aligned} \mathbf{J}_{s_1} &\approx \sum_{v_1=1}^{V_1} I_{v_1} \mathbf{f}_{v_1}(\mathbf{r}), \\ \mathbf{J}_{s_2} &\approx \sum_{v_2=1}^{V_2} I_{v_2} \mathbf{f}_{v_2}(\mathbf{r}) \end{aligned} \tag{4.14}$$

and on S_3 as

$$\mathbf{M}_s \approx \sum_{v_3=1}^{V_3} M_{v_3} \mathbf{f}_{v_3}(\mathbf{r}) \tag{4.15}$$

where I_{v_1}, I_{v_2} and M_{v_3} are coefficients yet to be determined, and $V = V_1 + V_2 + V_3$ represents the total number of interior edges. Since a basis function is associated with every such defined edge of the triangulated structure, up to three basis functions may have nonzero values within each triangular face. At a given edge however, only the basis function associated with that edge has a current component normal to the edge since all other basis currents in adjacent faces are parallel to the edge. Furthermore, since the normal component of $\mathbf{f}_v$ at the v^{th} edge is unity, each coefficient I_v (or M_v), may be interpreted as the normal component of current density flowing past that edge.

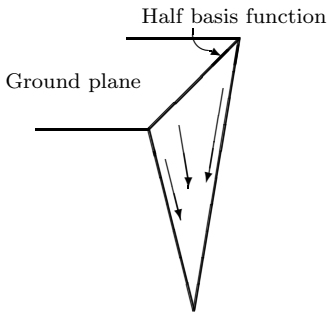

Figure 4.3: Definition of half subsectional basis functions.

At boundary edges, the sum of the normal components of current on opposite sides of the surface cancel because of current continuity. Such edges are left undefined with no contribution to Eqns. 4.14 and 4.15. However, a different approach is needed to model the flow of induced currents through an edge of the geometry into an electrical ground plane. A special set of basis functions, called half basis functions, is used to ensure continuity of current at such an interface. Fig. 4.3 suggests the location of a half subsectional basis

function. These half basis functions show similar properties to the basis functions defined on interior edges, the difference being that continuity is now achieved between a boundary edge and a non-discretised conducting surface.

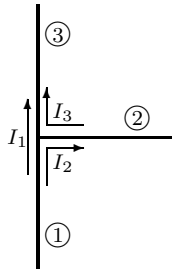

Figure 4.4: Definition of extra basis functions.

Finally, the total flow of current at a junction such as that shown in Fig. 4.4 must equal zero. This requires defining extra basis functions, i.e. between every two triangles that share a common edge, a basis function is to be defined. This results in a multiple of edges that physically describes only one edge position. Following from Fig. 4.4

$$-(I_1 + I_2) + (I_2 - I_3) + (I_1 + I_3) = 0 \tag{4.16}$$

verifying that Kirchhoff's current law is indeed satisfied.

4.3 Testing Procedure

In order to find the current coefficients, the combined field MPIEs are tested with respect to a particular testing function. The testing function was chosen to be identical to the expansion function $\mathbf{f}_v$ developed in the previous section. Based on the symmetric product defined as

$$< \mathbf{f}, \mathbf{g} >= \int_S \mathbf{f} \cdot \mathbf{g} dS, \tag{4.17}$$

Eqn. 4.9 can be tested with $\mathbf{f}_u$, yielding

$$< \mathbf{E}_1^i, \mathbf{f}_{u_1} > = j\omega < \mathbf{A}_1, \mathbf{f}_{u_1} > + < \nabla\Phi_1, \mathbf{f}_{u_1} > + < \nabla \times \frac{\mathbf{F}_1}{\epsilon_1}, \mathbf{f}_{u_1} >, \tag{4.18}$$

$$< \mathbf{E}_2^i, \mathbf{f}_{u_2} > = j\omega < \mathbf{A}_2, \mathbf{f}_{u_2} > + < \nabla\Phi_2, \mathbf{f}_{u_2} > + < \nabla \times \frac{\mathbf{F}_2}{\epsilon_2}, \mathbf{f}_{u_2} > \tag{4.19}$$

and

$$\begin{aligned} < \mathbf{H}_1^i - \mathbf{H}_2^i, \mathbf{f}_{u_3} > = {} & j\omega < \mathbf{F}_1 - \mathbf{F}_2, \mathbf{f}_{u_3} > + < \nabla\Psi_1 - \nabla\Psi_2, \mathbf{f}_{u_3} > - \\ & < \nabla \times (\frac{\mathbf{A}_1}{\mu_1} - \frac{\mathbf{A}_2}{\mu_2}), \mathbf{f}_{u_3} >, \end{aligned} \tag{4.20}$$

with $u_1 = 1, 2, ..., V_1$, $u_2 = 1, 2, ..., V_2$ and $u_3 = 1, 2, ..., V_3$.

A considerable simplification results when evaluating the individual terms of Eqns. 4.18, 4.19 and 4.20 at the respective triangle centroids

$$\mathbf{r}^c = \frac{1}{3}(\mathbf{r}_1 + \mathbf{r}_2 + \mathbf{r}_3). \tag{4.21}$$

To illustrate the approximations used, the vector potential and incident field terms in Eqn. 4.18 may be written as

$$\begin{aligned} \left\langle \begin{Bmatrix} \mathbf{E}_1^i \\ \mathbf{A}_1 \end{Bmatrix}, \mathbf{f}_{u_1} \right\rangle &= l_{u_1} \left[\frac{1}{2A_{u_1}^+} \int_{T_{u_1}^+} \begin{Bmatrix} \mathbf{E}_1^i \\ \mathbf{A}_1 \end{Bmatrix} \cdot \boldsymbol{\varrho}_{u_1}^+ dS + \frac{1}{2A_{u_1}^-} \int_{T_{u_1}^-} \begin{Bmatrix} \mathbf{E}_1^i \\ \mathbf{A}_1 \end{Bmatrix} \cdot \boldsymbol{\varrho}_{u_1}^- dS \right] \\ &\approx \frac{l_{u_1}}{2} \left[\begin{Bmatrix} \mathbf{E}_1^i(\mathbf{r}_{u_1}^{c+}) \\ \mathbf{A}_1(\mathbf{r}_{u_1}^{c+}) \end{Bmatrix} \cdot \boldsymbol{\varrho}_{u_1}^{c+} + \begin{Bmatrix} \mathbf{E}_1^i(\mathbf{r}_{u_1}^{c-}) \\ \mathbf{A}_1(\mathbf{r}_{u_1}^{c-}) \end{Bmatrix} \cdot \boldsymbol{\varrho}_{u_1}^{c-} \right], \end{aligned} \tag{4.22}$$

where the integral over each triangle is eliminated by evaluating $\mathbf{E}_1^i$ or $\mathbf{A}_1$ in each triangle by its value at the triangle centroid.

Similarly, the second term can be rewritten as

$$< \nabla\Phi_1, \mathbf{f}_{u_1} >= -\int_{S_1} \Phi_1 \nabla \cdot \mathbf{f}_{u_1} dS \tag{4.23}$$

and using Eqn. 4.13 the integral simplifies to

$$\begin{aligned} \int_{S_1} \Phi_1 \nabla \cdot \mathbf{f}_{u_1} dS &= l_{u_1} \Big[\frac{1}{A_{u_1}^+} \int_{T_{u_1}^+} \Phi_1 dS - \frac{1}{A_{u_1}^-} \int_{T_{u_1}^-} \Phi_1 dS \Big] \\ &\approx l_{u_1} \Big[\Phi(\mathbf{r}_{u_1}^{c+}) - \Phi(\mathbf{r}_{u_1}^{c-}) \Big]. \end{aligned} \tag{4.24}$$

In Eqn. 4.24 the average of Φ_1 over each triangle is approximated by the value of Φ_1 at the triangle centroid.

The last term in Eqn. 4.18 can be simplified as

$$\begin{aligned} < \nabla \times \frac{\mathbf{F}_1}{\epsilon_1}, \mathbf{f}_{u_1} > &= l_{u_1} \left[\frac{1}{2A_{u_1}^+} \int_{T_{u_1}^+} \left(\nabla \times \frac{\mathbf{F}_1}{\epsilon_1} \right) \cdot \boldsymbol{\varrho}_{u_1}^+ dS + \frac{1}{2A_{u_1}^-} \int_{T_{u_1}^-} \left(\nabla \times \frac{\mathbf{F}_1}{\epsilon_1} \right) \cdot \boldsymbol{\varrho}_{u_1}^- dS \right] \\ &= l_{u_1} \Big[P_1(\mathbf{r}_{u_1}^+) + P_1(\mathbf{r}_{u_1}^-) \Big]. \end{aligned} \tag{4.25}$$

On substituting Eqns. 4.22, 4.24 and 4.25 into the tested form of Eqn. 4.18, the following functional form is obtained

$$\begin{aligned} l_{u_1} \left[\mathbf{E}_1^i(\mathbf{r}_{u_1}^{c+}) \cdot \frac{\boldsymbol{\varrho}_{u_1}^{c+}}{2} + \mathbf{E}_1^i(\mathbf{r}_{u_1}^{c-}) \cdot \frac{\boldsymbol{\varrho}_{u_1}^{c-}}{2} \right] = l_{u_1} \Bigg[& j\omega \left(\mathbf{A}_1(\mathbf{r}_{u_1}^{c+}) \cdot \frac{\boldsymbol{\varrho}_{u_1}^{c+}}{2} + \mathbf{A}_1(\mathbf{r}_{u_1}^{c-}) \cdot \frac{\boldsymbol{\varrho}_{u_1}^{c-}}{2} \right) \\ & + \Phi_1(\mathbf{r}_{u_1}^{c-}) - \Phi_1(\mathbf{r}_{u_1}^{c+}) + P_1(\mathbf{r}_{u_1}^+) + P_1(\mathbf{r}_{u_1}^-) \Bigg]. \end{aligned} \tag{4.26}$$

This equation is enforced at each triangle edge, $u_1 = 1, 2, ..., V_1$. Similarly, Eqn. 4.19 is tested at each edge, $u_2 = 1, 2, ..., V_2$, to give

$$l_{u_2}\left[\mathbf{E}_2^i(\mathbf{r}_{u_2}^{c+})\cdot\frac{\boldsymbol{\varrho}_{u_2}^{c+}}{2}+\mathbf{E}_2^i(\mathbf{r}_{u_2}^{c-})\cdot\frac{\boldsymbol{\varrho}_{u_2}^{c-}}{2}\right]=l_{u_2}\Bigg[j\omega\bigg(\mathbf{A}_2(\mathbf{r}_{u_2}^{c+})\cdot\frac{\boldsymbol{\varrho}_{u_2}^{c+}}{2}+\mathbf{A}_2(\mathbf{r}_{u_2}^{c-})\cdot\frac{\boldsymbol{\varrho}_{u_2}^{c-}}{2}\bigg)+\Phi_2(\mathbf{r}_{u_2}^{c-})-\Phi_1(\mathbf{r}_{u_2}^{c+})+P_2(\mathbf{r}_{u_2}^{+})+P_2(\mathbf{r}_{u_2}^{-})\Bigg]. \tag{4.27}$$

The purpose of approximations 4.22 and 4.24 is to eliminate surface integrals of the potential quantities, allowing a double surface integral to be approximated by a quantity involving a single surface integral in the numerical computation of the moment matrix elements. These approximations are justified by observing that the potentials are locally smooth within each subdomain, as follows from their integral definitions and the locally smooth nature of the source representation in terms of the basis functions. However, the integrals containing the curl operator as defined in Eqn. 4.25 will be evaluated numerically; the derivative of a locally smooth function is not necessarily smooth.

By using similar approximations when testing Eqn. 4.20 at each triangle edge, $u_3 = 1, 2, ..., V_3$, the following functional form is obtained

$$\begin{aligned}&l_{u_3}\left[\Big(\mathbf{H}_1^i(\mathbf{r}_{u_3}^{c+})-\mathbf{H}_2^i(\mathbf{r}_{u_3}^{c+})\Big)\cdot\frac{\boldsymbol{\varrho}_{u_3}^{c+}}{2}+\Big(\mathbf{H}_1^i(\mathbf{r}_{u_3}^{c-})-\mathbf{H}_2^i(\mathbf{r}_{u_3}^{c-})\Big)\cdot\frac{\boldsymbol{\varrho}_{u_3}^{c-}}{2}\right]\\ &=l_{u_3}\Bigg[j\omega\Big(\big(\mathbf{F}_1(\mathbf{r}_{u_3}^{c+})-\mathbf{F}_2(\mathbf{r}_{u_3}^{c+})\big)\cdot\frac{\boldsymbol{\varrho}_{u_3}^{c+}}{2}+\big(\mathbf{F}_1(\mathbf{r}_{u_3}^{c-})-\mathbf{F}_2(\mathbf{r}_{u_3}^{c-})\big)\cdot\frac{\boldsymbol{\varrho}_{u_3}^{c-}}{2}\Big)+\\ &\quad\Psi_1(\mathbf{r}_{u_3}^{c-})-\Psi_2(\mathbf{r}_{u_3}^{c-})-\Psi_1(\mathbf{r}_{u_3}^{c+})+\Psi_2(\mathbf{r}_{u_3}^{c+})-\\ &\quad Q_1(\mathbf{r}_{u_3}^{+})+Q_2(\mathbf{r}_{u_3}^{+})-Q_1(\mathbf{r}_{u_3}^{-})+Q_2(\mathbf{r}_{u_3}^{-})\Bigg]\end{aligned} \tag{4.28}$$

where

$$Q_{1,2}(\mathbf{r}_{u_3}^{\pm})=\frac{1}{2A_{u_3}^{\pm}}\int_{T_{u_3}^{\pm}}\left(\nabla\times\frac{\mathbf{A}_{1,2}}{\mu_{1,2}}\right)\cdot\boldsymbol{\varrho}_{u_3}^{\pm}dS. \tag{4.29}$$

If the approximations had not been made, the testing procedure would have been identical to Galerkin's method since the basis and testing functions chosen are identical. For the MPIE, where the problem is solved for either electric or magnetic currents, the matrix would then satisfy the symmetry property $Z_{uv} = Z_{vu}$. This desirable property is lost due to the approximations made. A factor two advance in both execution speed and memory usage justifies the ideality in restoring such symmetry. Knowing that Z_{uv} and Z_{vu} are different approximations to the same quantity, [24] investigated the possibility in filling only the upper (or lower) triangular matrix of $\bar{\bar{Z}}$. It was found sufficient to compute only half the matrix elements and then simply enforce the symmetrical property $Z_{uv} = Z_{vu}$. When a problem supports both electric and magnetic currents, the *curl* operators in

Eqn. 4.9 disrupt symmetry in the moment matrix. A different approach to packing the matrix is developed and explained in Appendix C.

4.4 Matrix Equation Derivation

Substitution of the electric and magnetic current expansion terms of Eqns. 4.14 and 4.15 into Eqns. 4.26, 4.27 and 4.28 reduces the functional form of the equation to a corresponding partitioned matrix equation [41],

$$\begin{bmatrix} [Z^{JJ}_{u_1v_1}] & [\ 0\ ] & [Z^{JM}_{u_1v_3}] \\ [\ 0\ ] & [Z^{JJ}_{u_2v_2}] & [Z^{JM}_{u_2v_3}] \\ [Z^{MJ}_{u_3v_1}] & [Z^{MJ}_{u_3v_2}] & [Z^{MM}_{u_3v_3}] \end{bmatrix} \begin{bmatrix} [I_{v_1}] \\ [I_{v_2}] \\ [M_{v_3}] \end{bmatrix} = \begin{bmatrix} [E_{u_1}] \\ [E_{u_2}] \\ [H_{u_3}] \end{bmatrix}. \tag{4.30}$$

The elements of the electric and magnetic field excitation vectors are

$$\begin{aligned} E_{u_1} &= l_{u_1}\left(\mathbf{E}^i_1(\mathbf{r}^{c+}_{u_1})\cdot\frac{\boldsymbol{\varrho}^{c+}_{u_1}}{2} + \mathbf{E}^i_1(\mathbf{r}^{c-}_{u_1})\cdot\frac{\boldsymbol{\varrho}^{c-}_{u_1}}{2}\right), \\ E_{u_2} &= l_{u_2}\left(\mathbf{E}^i_2(\mathbf{r}^{c+}_{u_2})\cdot\frac{\boldsymbol{\varrho}^{c+}_{u_2}}{2} + \mathbf{E}^i_2(\mathbf{r}^{c-}_{u_2})\cdot\frac{\boldsymbol{\varrho}^{c-}_{u_2}}{2}\right) \end{aligned} \tag{4.31}$$

and

$$H_{u_3} = l_{u_3}\left(\left(\mathbf{H}^i_1(\mathbf{r}^{c+}_{u_3}) - \mathbf{H}^i_2(\mathbf{r}^{c+}_{u_3})\right)\cdot\frac{\boldsymbol{\varrho}^{c+}_{u_3}}{2} + \left(\mathbf{H}^i_1(\mathbf{r}^{c-}_{u_3}) - \mathbf{H}^i_2(\mathbf{r}^{c-}_{u_3})\right)\cdot\frac{\boldsymbol{\varrho}^{c-}_{u_3}}{2}\right). \tag{4.32}$$

In the system of linear equations Z_{uv} is a $V\times V$ matrix where the various matrix elements are given by the following

$$\begin{aligned} Z^{JJ}_{u_1v_1} &= l_{u_1}\left[j\omega\left(\mathbf{A}^+_{1,u_1v_1}\cdot\frac{\boldsymbol{\varrho}^{c+}_{u_1}}{2} + \mathbf{A}^-_{1,u_1v_1}\cdot\frac{\boldsymbol{\varrho}^{c-}_{u_1}}{2}\right) + \left(\Phi^-_{1,u_1v_1} - \Phi^+_{1,u_1v_1}\right)\right] \\ Z^{JM}_{u_1v_3} &= l_{u_1}\left[P^+_{1,u_1v_3} + P^-_{1,u_1v_3}\right] \\ Z^{JJ}_{u_2v_2} &= l_{u_2}\left[j\omega\left(\mathbf{A}^+_{2,u_2v_2}\cdot\frac{\boldsymbol{\varrho}^{c+}_{u_2}}{2} + \mathbf{A}^-_{2,u_2v_2}\cdot\frac{\boldsymbol{\varrho}^{c-}_{u_2}}{2}\right) + \Phi^-_{2,u_2v_2} - \Phi^+_{2,u_2v_2}\right] \\ Z^{JM}_{u_2v_3} &= -l_{u_2}\left[P^+_{2,u_2v_3} + P^-_{2,u_2v_3}\right] \\ Z^{MJ}_{u_3v_1} &= -l_{u_3}\left[Q^+_{1,u_3v_1} + Q^-_{1,u_3v_1}\right] \\ Z^{MJ}_{u_3v_2} &= l_{u_3}\left[Q^+_{2,u_3v_2} + Q^-_{2,u_3v_2}\right] \\ Z^{MM}_{u_3v_3} &= l_{u_3}\left[j\omega\left(\left(\mathbf{F}^+_{1,u_3v_3} + \mathbf{F}^+_{2,u_3v_3}\right)\cdot\frac{\boldsymbol{\varrho}^{c+}_{u_3}}{2} + \left(\mathbf{F}^-_{1,u_3v_3} + \mathbf{F}^-_{2,u_3v_3}\right)\cdot\frac{\boldsymbol{\varrho}^{c-}_{u_3}}{2}\right) + \right. \\ &\qquad \left.\left(\Psi^-_{1,u_3v_3} - \Psi^+_{1,u_3v_3}\right) + \left(\Psi^-_{2,u_3v_3} - \Psi^+_{2,u_3v_3}\right)\right]. \end{aligned} \tag{4.33}$$

In both $Z_{u_2v_3}$ and $Z_{u_3v_3}$ a sign change was incorporated into $\mathbf{F}_2$ and Ψ_2. This is due to the required current continuity at the dielectric interface between Regions 1 and 2.

Using Eqns. 4.10 and 4.11, the vector and scalar potential integrals take the following form

$$\begin{aligned}
\mathbf{A}_{uv}^{\pm} &= \int_S \bar{\bar{\mathbf{K}}}_A(\mathbf{r}_u^{c\pm}|\mathbf{r}') \cdot \mathbf{f}_v(\mathbf{r}')dS' \\
\Phi_{uv}^{\pm} &= \int_S G_\Phi(\mathbf{r}_u^{c\pm}|\mathbf{r}')q_s(\mathbf{r}')dS' \\
&= -\frac{1}{j\omega}\int_S G_\Phi(\mathbf{r}_u^{c\pm}|\mathbf{r}')\big[\nabla' \cdot \mathbf{f}_v(\mathbf{r}')\big]dS' \\
P_{uv}^{\pm} &= \frac{1}{2A_u^{\pm}}\int_{T_u^{\pm}} \frac{1}{\epsilon}\nabla \times \Big(\int_S \bar{\bar{\mathbf{K}}}_F(\mathbf{r}_u^{\pm}|\mathbf{r}') \cdot \mathbf{f}_v(\mathbf{r}')dS'\Big) \cdot \boldsymbol{\varrho}_u^{\pm}dS.
\end{aligned} \tag{4.34}$$

The integration surface S is equivalent to the two triangles spanning the base function under consideration. Note that the $\pm$ superscripts serve to distinguish $\mathbf{A}_{uv}^{\pm}$ from $\mathbf{A}$, the standard magnetic vector potential. The expressions in Eqn. 4.34 are without the current coefficients I_v. Similar results hold for $\mathbf{F}_{uv}^{\pm}$, $\Psi_{uv}^{\pm}$ and $Q_{uv}^{\pm}$.

4.5 Efficient Implementation

Evaluation of each matrix element Z_{uv} associated with edges u and v involves integrations over triangles $T_v^{\pm}$ with observation points located at the centroids of triangles $T_u^{\pm}$. Some of the same integrals required for the element Z_{uv} are also needed to compute an element Z_{rs}. This happens when $r \neq u$, $s \neq v$, edge r is an edge of T_u^+ or T_u^- while edge s is an edge of T_v^+ or T_v^-. If one focuses attention on a single pair of faces rather than a pair of edges, it is observed that the integrals evaluated for a source face with scalar and vector potentials observed at the centroid of another face are involved in all elements Z_{uv} having edges v as (non-boundary) edges of the source triangle and edges u as the (non-boundary) edges of the observation triangle. Thus, various matrix elements can be easily generated by considering faces rather than edges. An approximately nine times increase in computational speed justifies computing the required potential integrals by face-pair combinations, rather than to directly compute single elements of $\bar{\bar{Z}}$ by edge-pair combinations.

Consider evaluating the vector and scalar potential integrals for a given source and observation face combination. Fig. 4.5 illustrates such a face pair with the observation point in face p and the source currents residing in face q. Each of the three basis functions which may exist simultaneously in T^q is proportional to one of the vectors $\boldsymbol{\varrho}_1$, $\boldsymbol{\varrho}_2$ or $\boldsymbol{\varrho}_3$ defined in the figure. Each vector $\boldsymbol{\varrho}_i$ is directed away from its associated vertex, but would be directed toward the vertex if the current reference direction for the associated edge was

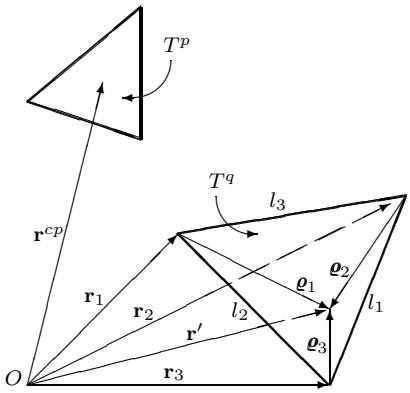

Figure 4.5: Local coordinates and edges for source triangle T^q with observation point in triangle T^p.

into the triangle. Consequently,

$$\boldsymbol{\varrho}_i(\mathbf{r}') = \pm(\mathbf{r}' - \mathbf{r}_i), \qquad i = 1,\, 2,\, 3. \tag{4.35}$$

The positive sign is associated with a positive current reference direction out of T^q while the negative sign is used otherwise. The potential integrals

$$\mathbf{A}_i^{pq} = \frac{l_i}{2A^q} \int_{T^q} \bar{\bar{\mathbf{K}}}_A(\mathbf{r}^{cp}|\mathbf{r}') \cdot \boldsymbol{\varrho}_i(\mathbf{r}') dS' \tag{4.36}$$

and

$$\Phi_i^{pq} = \mp \frac{1}{j\omega} \frac{l_i}{A^q} \int_{T^q} K_\Phi(\mathbf{r}^{cp}|\mathbf{r}') dS' \tag{4.37}$$

must be evaluated, associated with the i^{th} basis function on face q and observed at the centroid on face p. When the curl operator is present in the potential integrand, a double surface integral need to be evaluated. Similar to Eqn. 4.35, there now also exist three possible testing functions in T^p, each proportional to $\boldsymbol{\varrho}_j(\mathbf{r}) = \pm(\mathbf{r} - \mathbf{r}_j)$. Thus, weighted with the i^{th} basis function on face q and tested with the j^{th} basis function on face p

$$\begin{aligned} P_i^{pq} &= \frac{1}{2A^p} \int_{T^p} \frac{1}{\epsilon} \nabla \times \left(\frac{l_i}{2A^q} \int_{T^q} \bar{\bar{\mathbf{K}}}_F(\mathbf{r}|\mathbf{r}') \cdot \boldsymbol{\varrho}_i(\mathbf{r}') dS' \right) \cdot \boldsymbol{\varrho}_j(\mathbf{r}) dS \\ &= \frac{l_i}{4A^p A^q} \frac{1}{\epsilon} \int_{T^p} \int_{T^q} \nabla \times \bar{\bar{\mathbf{K}}}_F(\mathbf{r}|\mathbf{r}') \cdot \boldsymbol{\varrho}_i(\mathbf{r}') \cdot \boldsymbol{\varrho}_j(\mathbf{r}) dS' dS. \end{aligned} \tag{4.38}$$

For each face-pair combination, the potential integrals may be multiplied by the approximate coefficients (Eqn. 4.33) and their contributions accumulated in the appropriate elements of $\bar{\bar{Z}}$ as they are computed.

Eqns. 4.36, 4.37 and 4.38 are most conveniently evaluated by transforming the global coordinate system to a local system of coordinates within T^q. The vectors in Fig. 4.5

divide T^q into three subtriangles A_1, A_2 and A_3, with respectively, l_1, l_2 or l_3 as one of their sides. Realising that the areas are not independent, $A_1 + A_2 + A_3 = A^q$, a suitable coordinate change is to the so-called normalised or simplex area coordinates [42]

$$\xi = \frac{A_1}{A^q}, \quad \eta = \frac{A_2}{A^q}, \quad \zeta = \frac{A_3}{A^q}, \tag{4.39}$$

which, because of the area constraint, must satisfy

$$\xi + \eta + \zeta = 1. \tag{4.40}$$

Note that all three coordinates vary between zero and unity in T^q and that at the triangle vertices $\mathbf{r}_1^q$, $\mathbf{r}_2^q$ and $\mathbf{r}_3^q$, the triplet (ξ, η, ζ) takes on the values $(1, 0, 0)$, $(0, 1, 0)$ and $(0, 0, 1)$ respectively. The transformation from Cartesian to simplex coordinates may be written in vector form as

$$\mathbf{r}' = \xi \mathbf{r}_1^q + \eta \mathbf{r}_2^q + \zeta \mathbf{r}_3^q, \tag{4.41}$$

where ξ, η and ζ are subject to the constraint in Eqn. 4.40. Both [39] and [43] explain how to numerically evaluate integrals using an N_k point integration method principally applicable to triangular distributions. The surface integrals over T^q is performed by a Gaussian quadrature rule and transforms such that

$$\int_{T^q} g(\mathbf{r}) dS = A^q \sum_{k=1}^{N_k} w_k g(\xi_k \mathbf{r}_1^q + \eta_k \mathbf{r}_2^q + \zeta_k \mathbf{r}_3^q) \tag{4.42}$$

where for the k^{th} Gaussian point of location (ξ_k, η_k, ζ_k), there corresponds a Gaussian weight w_k and a functional evaluation $g(\xi_k, \eta_k, \zeta_k)$. A listing of values to ξ, η, ζ and w are given in [39, Appendix II].

Using Eqns. 4.35, 4.41 and 4.42, Eqn. 4.36 may now be written as

$$\begin{aligned} \mathbf{A}_i^{pq} &= \pm \frac{l_i}{2} \sum_{k=1}^{N_k} w_k \Big[\bar{\bar{\mathbf{K}}}_A(\mathbf{r}^{cp} | \mathbf{r}'_k) \cdot [\xi_k(\mathbf{r}_1^q - \mathbf{r}_3^q) + \eta_k(\mathbf{r}_2^q - \mathbf{r}_3^q) + (\mathbf{r}_3^q - \mathbf{r}_i^q)] \Big] \\ &= \pm \frac{l_i}{2} [\mathbf{I}_{A\xi}^{pq} + \mathbf{I}_{A\eta}^{pq} + \mathbf{I}_A^{pq}] \end{aligned} \tag{4.43}$$

where

$$\begin{aligned} \mathbf{I}_{A\xi}^{pq} &= \sum_{k=1}^{N_k} w_k \Big[\bar{\bar{\mathbf{K}}}_A(\mathbf{r}^{cp} | \mathbf{r}'_k) \cdot (\mathbf{r}_1^q - \mathbf{r}_3^q) \xi_k \Big] \\ \mathbf{I}_{A\eta}^{pq} &= \sum_{k=1}^{N_k} w_k \Big[\bar{\bar{\mathbf{K}}}_A(\mathbf{r}^{cp} | \mathbf{r}'_k) \cdot (\mathbf{r}_2^q - \mathbf{r}_3^q) \eta_k \Big] \\ \mathbf{I}_A^{pq} &= \sum_{k=1}^{N_k} w_k \Big[\bar{\bar{\mathbf{K}}}_A(\mathbf{r}^{cp} | \mathbf{r}'_k) \cdot (\mathbf{r}_3^q - \mathbf{r}_i^q) \Big]. \end{aligned} \tag{4.44}$$

Similarly, Eqn. 4.37 becomes

$$\begin{aligned}\Phi_i^{pq} &= \mp\frac{l_i}{j\omega}\sum_{k=1}^{N_k} w_k K_\Phi(\mathbf{r}^{cp}|\mathbf{r}'_k) \\ &= \mp\frac{l_i}{j\omega} I_\Phi^{pq}\end{aligned} \tag{4.45}$$

where

$$I_\Phi^{pq} = \sum_{k=1}^{N_k} w_k K_\Phi(\mathbf{r}^{cp}|\mathbf{r}'_k) \tag{4.46}$$

and lastly Eqn. 4.38 becomes

$$\begin{aligned}P_i^{pq} = \frac{l_i}{4\epsilon}\sum_{k_1=1}^{N_{k_1}} w_{k_1}\sum_{k=1}^{N_k} w_k \Big[&\big(\nabla\times\bar{\bar{\mathbf{K}}}_F(\mathbf{r}|\mathbf{r}'_k)\big|_{\mathbf{r}=\mathbf{r}_{k_1}}\big)\cdot \\ &(\pm)\big(\xi_k(\mathbf{r}_1^q-\mathbf{r}_3^q)+\eta_k(\mathbf{r}_2^q-\mathbf{r}_3^q)+(\mathbf{r}_3^q-\mathbf{r}_i^q)\big)\Big]\cdot \\ &(\pm)\Big[\xi_{k_1}(\mathbf{r}_1^p-\mathbf{r}_3^p)+\eta_{k_1}(\mathbf{r}_2^p-\mathbf{r}_3^p)+(\mathbf{r}_3^p-\mathbf{r}_j^p)\Big]\end{aligned} \tag{4.47}$$

A combination of these integrals must be evaluated for each face pair p and q. These contribute in up to 9 elements of $\bar{\bar{Z}}$ in Eqn. 4.30. For the terms $p = q$ the integrands are singular, and for these cases the static singular portion of each integrand must be removed and integrated analytically. This is explained in Appendix D.

When the source and observation triangles are separated by large distances, approximate expressions are used to evaluate the numerical integration over the source triangle. The criterion for distinguishing near and far interactions is based on the percent difference between the maximum and minimum distances from the three vertices of the source triangle to the centroid of the observation triangle. If the difference is less than 15%,

$$\frac{R_{max}-R_{min}}{R_{min}} \leq 0.15, \tag{4.48}$$

where

$$\begin{aligned}R_{max} &= \max|\mathbf{r}^{cp}-\mathbf{r}_i|, \\ R_{min} &= \min|\mathbf{r}^{cp}-\mathbf{r}_i|, \qquad\qquad i=1,2,3,\end{aligned} \tag{4.49}$$

a far approximation is viable [13], i.e. the surface integration over the source triangle is replaced by the evaluation of the integrand at the centroid of the triangle. This speeds up the computation of the $\bar{\bar{Z}}$ matrix considerably.

To further reduce computation speed a sliding scale was introduced for integrations between near and far interactions. The N point integration method mentioned in Eqn. 4.42,

uses N points to numerically evaluate a complete polynomial of highest order P. As the distance between the source and observation triangles increases, a polynomial of lower order and thus also lesser points may be used to approximate the surface integration. Reaching the criterion specified for far interactions, a polynomial of order 1 and using only one evaluation point is suggested. From the listing [39, Appendix II], the point is specified at the centroid of the triangle and so it can be affirmed that the previous approximation model used by [13] is still valid.

4.6 Excitation Mechanism—Delta Gap

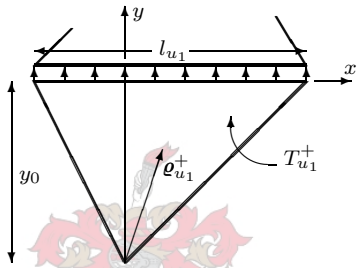

Figure 4.6: Delta gap voltage source between triangles $T^+_{u_1}$ and $T^-_{u_1}$ at $y = 0$.

The excitation fields are seldom known in a direct way, except in a few cases, such as excitation with a plane wave or with a series voltage gap generator. The difficulty encountered is the implementation of a practical excitation mechanism which can be included in the mathematical modelling. While voltage gap sources are not the driving mechanism typically employed in practice, they can be legitimately used in the process of extracting scattering parameters. This is explained Section 4.7.

To compute the excitation vectors E_{u_1}, E_{u_2} and H_{u_3} in Eqn. 4.30, apply a voltage source between an infinitesimally small gap of length $\delta \to 0$ across the common edge u_1 of triangles $T^+_{u_1}$ and $T^-_{u_1}$. Consider Fig. 4.6. If the delta gap is located in triangle $T^+_{u_1}$, the $\mathbf{E}$ field on edge u_1 is given by $\mathbf{E} = \delta(y)\hat{\mathbf{y}}$ and the $\mathbf{H}$ field is zero, giving $H_{u_2} = 0$.

From the definition of the excitation vector, it follows that

$$E_{u_1} = \int_{T^+_{u_1}} \mathbf{E} \cdot \mathbf{f}_{u_1} dS. \tag{4.50}$$

Substituting the electric field $\mathbf{E}$ and the subsectional testing function $\mathbf{f}_{u_1}$ (Eqn. 4.12),

$$E_{u_1} = \frac{l_{u_1}}{2A^+_{u_1}} \int\int \delta(y)\hat{\mathbf{y}} \cdot \boldsymbol{\varrho}^+_{u_1} dydx \tag{4.51}$$

is obtained. Using the integration properties of the Dirac delta function and defining $y_0 = \hat{\mathbf{y}} \cdot \boldsymbol{\varrho}_{u_1}^{+}(y = 0)$ as the component of the basis function perpendicular to the ${u_1}^{\text{th}}$ triangle edge, Eqn. 4.51 reduces to

$$E_{u_1} = \frac{l_{u_1}}{2A_{u_1}^{+}} \int y_0 dx = l_{u_1}. \tag{4.52}$$

Therefore, for a delta gap voltage source between triangles $T_{u_1}^{+}$ and $T_{u_1}^{-}$, the excitation vector E_{u_1} has only one nonzero element, the ${u_1}^{\text{th}}$ element, which is equal to l_{u_1}, the length of the boundary edge between $T_{u_1}^{+}$ and $T_{u_1}^{-}$.

4.7 Extracting Scattering Parameters

Once the approximate distribution of the surface current density is found by solving Eqn. 4.30 for the unknown weighting coefficients I_{v_1}, I_{v_2} and M_{v_3}, scattering parameters for an N-port discontinuity are obtained by examining the current distribution on the ports. In general, N linearly independent excitation schemes are required to evaluate an N-port network.

The ports are driven by applying horizontal voltage generators at the open-circuited port ends. The S-parameter extraction process only requires some form of excitation which allows examination of a sufficient number of current samples on the ports between the discontinuity and the port ends [13]. While the open-circuited port ends do affect the amplitude of the current waves on the ports, the relationships among the waves incident upon and reflected from the discontinuity are nonetheless uniquely defined by its S-parameters. This is confirmed by [7] showing that the reflection coefficient does not change in magnitude and phase if a coaxial line feed is substituted with a voltage gap generator and the line is left open at the excitation end.

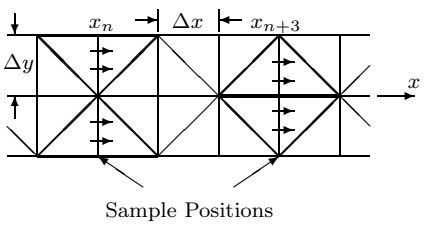

Figure 4.7: Scheme for sampling the x component of current on a uniform line

With the excitation applied to a port extending in the x direction, the sampled currents

on the ports are fitted to the unimodal wave model

$$I_{ij}(x) = \frac{1}{\sqrt{Z_{0_i}}}[a_{ij}e^{-\gamma_i x} - b_{ij}e^{+\gamma_i x}]. \tag{4.53}$$

$I_{ij}(x)$ is the sampled current distribution on the i^{th} port for the j^{th} excitation, obtained by integrating the x directed current density J_x across the port width. Consider the port discretisation as shown in Fig. 4.7. At the indicated sample positions x_n and x_{n+3}, only the highlighted basis functions have x components of current. In the development of the basis functions (Section 4.2) it was shown that the component of current density normal to an edge is constant and that the weighting coefficient may be interpreted as this normal component flowing past that edge. As an example, the current at sample point x_n is given by

$$I(x_n) = (i_1 + i_2)\Delta y \tag{4.54}$$

where i_1 and i_2 are the weighting coefficients for the basis functions spanning the sample point. In a non-uniform mesh, Δy will be substituted by the appropriate edge lengths at which the weighting coefficients are defined.

The uniform line characteristic impedance Z_{0_i} in Eqn. 4.53, is used to normalise the currents when the ports are not identical. For the purpose of this thesis, Z_{0_i} was incorporated into a_{ij} and b_{ij}. This constant factor has no effect on the final S-parameters which are a function of the relationships among the waves incident upon and reflected from the discontinuity.

When the excitation and sampling ports are the same, γ is obtained and optimised for smallest error in the fit. With three unknowns in Eqn. 4.53, it was decided to choose an initial γ value, $\gamma_m = jk_0$, and do a least-squares fit to obtain the values of the wave coefficients a and b. Using the least-squares fit, the optimisation process is reduced to finding the minimum of a one dimensional error function, $E(\gamma)$, which was set to the maximum relative error in a particular fit. Newton-Raphson technique was used to determine the optimised γ value,

$$\gamma_{m+1} = \gamma_m - \alpha\frac{E(\gamma_m)}{E'(\gamma_m)}. \tag{4.55}$$

The factor α was introduced to compensate for possible runaway that may result because of small variations in the error function. Also, when a seemingly optimised γ is found, α is divided by two. This refines the step by which the optimisation proceeds and may lead to an even more refined γ value. A termination criterion of $\alpha < 1e^{-4}$ was used. The original Newton-Raphson algorithm converges on finding a zero. Ideally $E(\gamma) \to 0$, but practically the minimum value of $E(\gamma)$ needs to be found and therefore the termination criterion.

With the line constants known, forward and reverse complex wave coefficients a and b are generated through a least-squares fit of the current samples to Eqn. 4.53. Samples near the port end and discontinuities should be left out due to the presence of decaying modes.

The S-parameters are obtained directly from the computed wave coefficients using the standard S-parameter matrix definition $[b] = [S][a]$. Recasting this matrix to solve for S-parameters, S_{11} and S_{12} for example, are obtained for an arbitrary 2-port by solving

$$\begin{bmatrix} a_1^1 & a_2^1 \\ a_1^2 & a_2^2 \end{bmatrix} \begin{bmatrix} S_{11} \\ S_{12} \end{bmatrix} = \begin{bmatrix} b_1^1 \\ b_1^2 \end{bmatrix} \tag{4.56}$$

where the subscripts on wave coefficients a and b denote the port and the superscripts denote the excitation.

Finally, scattering parameters are more sensitive to errors in current than the far fields. Kipp and Chan [13] indicates that the extracting technique requires at least 20 subcells per wavelength to get acceptable results. This is a stiffer requirement than the 10 subcells per wavelength rule for MoM applied to far-field scattering problems. Also, at low frequencies such high levels of discretisation are unnecessary and become a liability as the electrical lengths of the ports shrink below one-quarter of a wavelength.

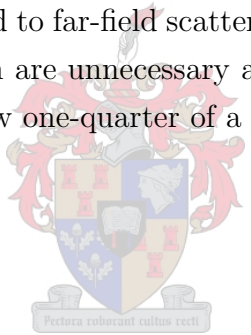

4.8 Conclusion

Based on the original formulation of Rao, Wilton and Glisson [11], a method of moments (MoM) technique has been developed to analyse arbitrarily shaped geometries within multiple substrate layers. The formulation was adapted to solve for both electric and magnetic distributions of surface current density. In Section 4.7 a numerical technique for computing S-parameters was presented, which may be used to evaluate possible microstrip discontinuities, planar antennas, waveguide structures, slot apertures and other geometries embedded in stratified media.

Chapter 5

Results

In this chapter some results obtained with the MoM formulation are presented to validate the analysis method. The examples are of varying complexity, each aimed at the evaluation of a different numerical property. Some examples consist of only horizontal electric scatterers in one layer, while others are spread over multiple layers and may include vertical connections. Finally, the method was applied to a complex multi-layered microstrip-slot-microstrip structure. This example was chosen for its combined electric and magnetic current evaluations.

Results are compared to measurements and numerical computations that have appeared in the literature. Numerical predictions obtained using commercial packages are also included for verification purposes. The results obtained are shown to correspond well with existing and measured data.

5.1 Effective Permittivity of a Microstrip Line

The effective permittivity of a microstrip transmission line of width 1.219 mm has been evaluated. The dielectric substrate has a relative permittivity $\epsilon_r = 9.7$ and thickness 1.27 mm. This geometry has already been analysed in [44] and measured in [45]. Fig. 5.1 shows the comparison between the values obtained with the present MoM formulation, those given by the references above and results generated by the commercial package Microwave Office 2001 Version 4.00. Results are shown between 1 and 8 GHz.

For the numerical solution three meshes were employed, each valid in a different frequency range, 1-2 GHz, 2-4 GHz, and 4-8 GHz. Each line was two transmission line wavelengths long in the lower frequency range and was divided into 160 longitudinal segments. In the

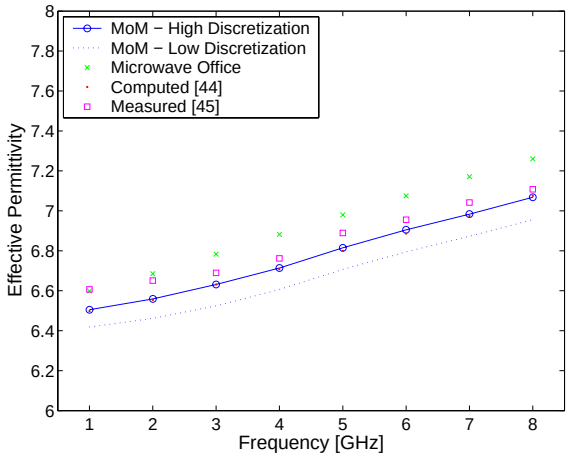

Figure 5.1: Effective permittivity of a microstrip line of width 1.219 mm on a substrate of relative permittivity $\epsilon_r = 9.7$ and thickness 1.27 mm.

transverse direction two different levels of discretisation were used. Either 1 or 3 square subcells span the line for a low and high discretisation.

When the high level of discretisation is used, agreement with the computations of [44] is very good and differences with the measurements of [45] are between 0.5 to 1.5%. It should be mentioned that the measured data found in [45] has an uncertainty of 2%. In the figure, the average values of these measurements are shown. Computed values obtained using Microwave Office have a strange, almost linear behaviour, showing an increased deviation at the higher frequencies. When only one transverse segment is employed, effective permittivities that are approximately 1.5% lower than the previous computations are obtained. This is probably because the edge effect is not properly modelled. Still, the computed effective permittivity is very close to those values given in [44] and [45].

5.2 Microstrip Stub Transmission

Radiation losses for open microstrip elements can be significant at millimeter-wave frequencies. To illustrate the ability of the analysis presented here to account for space and surface wave losses a microstrip stub on a single microstrip layer was compared to previously published measured and computed data.

The problem geometry is given in Fig. 5.2. The microstrip stub contains a T-junction discontinuity and an open end with parameters $w_1 = 1.44$ mm and $\ell_1 = 2.16$ mm. The substrate parameters are $h = 1.27$ mm and $\epsilon_r = 10.65$. For the analysis using triangular MoM, the two ports each have a width $w_2 = 1.44$ mm and extend $\ell_2 = 40$ mm (or

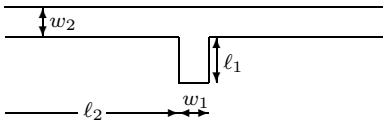

Figure 5.2: Geometry of a microstrip stub ($\epsilon_r = 10.65$, $h = 1.27$ mm, $w_1 = 1.44$ mm, $w_2 = 1.44$ mm, $\ell_1 = 2.16$ mm, $\ell_2 = 40$ mm).

41 subcells) in order to obtain a sufficient number of current samples.

Computed and measured responses are shown in Fig. 5.3a. The measurement data were found in [8], [9] published data obtained with an MoM analysis using a combination of rooftop and predetermined sinusoidal functions, [13] generated a response with an MoM code (also using triangular basis functions), and for comparison the response obtained using Microwave Office (MWO) is also shown. Agreement between the various computed and measured results is very good. The MoM codes all predict the location of the measured stub quarter-wave resonance at 10.15 GHz to within 0.1 GHz and the calculated transmission isolation at resonance is 19 dB (15 dB measured). The response generated by MWO shows resonance at 10 GHz. For MWO, the stub is constructed from a microstrip T-circuit element attached to a section of open-circuited line. These element models are operated within specified regions of validity.

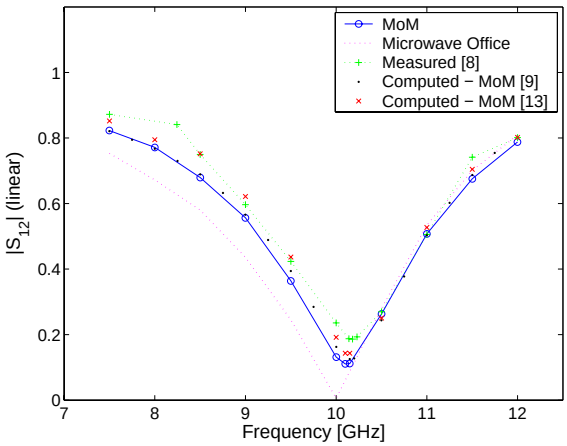

(a) Transmission magnitude.

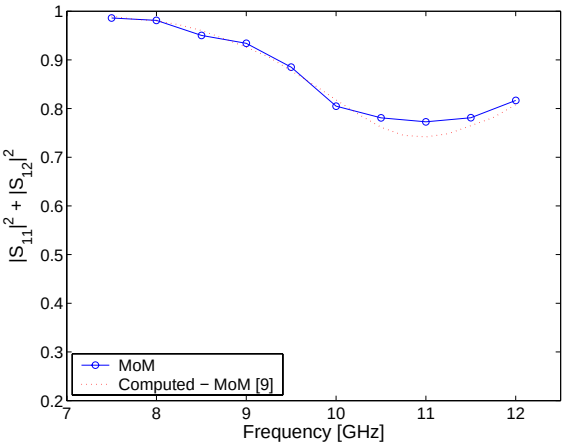

(b) $G = |S_{11}|^2 + |S_{12}|^2$.

Figure 5.3: Characteristics of a microstrip stub. $|S_{11}|^2 + |S_{12}|^2 < 1$ indicates radiation and surface wave loss.

Radiation loss can be an important effect for a substrate of this thickness. Fig. 5.3b corresponds to the quantity $G = |S_{11}|^2 + |S_{12}|^2$. For a lossy junction, $1 - G$ is the fraction

of incident power lost in the junction. This corresponds to the known relation for total radiated power

$$\frac{P_{\text{rad}}}{P_{\text{in}}} = 1 - |S_{11}|^2 - |S_{12}|^2. \tag{5.1}$$

The figure shows that the theoretical loss (radiation and surface waves) peaks at about 23% near 11 GHz.

5.3 Input Impedance for an Edge-fed Circular Microstrip Patch Antenna

Evaluation of the input impedance corresponds to the most sensitive of tests; the slightest change in the reflection coefficient will result in a significant change in the input impedance. The reflection coefficient and input impedance of a circular edge-fed microstrip patch antenna have been tested. The geometry is shown in Fig. 5.4. The dielectric substrate has a relative permittivity of $\epsilon_r = 2.2$ and a thickness of $h = 1.59$ mm. For the present formulation a transmission feed line of length $\ell = 140$ mm and width $w = 4.5474$ mm has been considered with 30 longitudinal segments and 1 transverse segment. The circular patch has a radius of $c = 21.5$ mm. This problem has been measured and numerically analysed in [46] and [12].

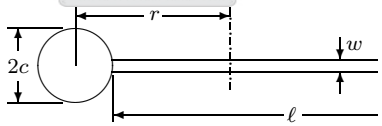

Figure 5.4: Geometry of a microstrip edge-fed circular patch antenna ($\epsilon_r = 2.2$, $h = 1.59$ mm, $c = 21.5$ mm, $w = 4.5474$ mm, $\ell = 140$ mm).

Fig. 5.5 shows a Smith chart plot of calculated and measured impedance loci for the patch antenna. The reference plane used in the present formulation was set at $r = 93.5$ mm from the centre of the circle. Measured data were found in [46] with no reference to the exact location of the phase reference plane.[1] According to [12] the reference plane is located at a distance $r = 96 \pm 0.5$ mm with large uncertainties due to unavailability of accurate data for determining the characteristics of the coaxial to microstrip line connections.

[1] "The measured input impedance data was phase-referenced to the input port of the coax-to-microstrip connector." [46]

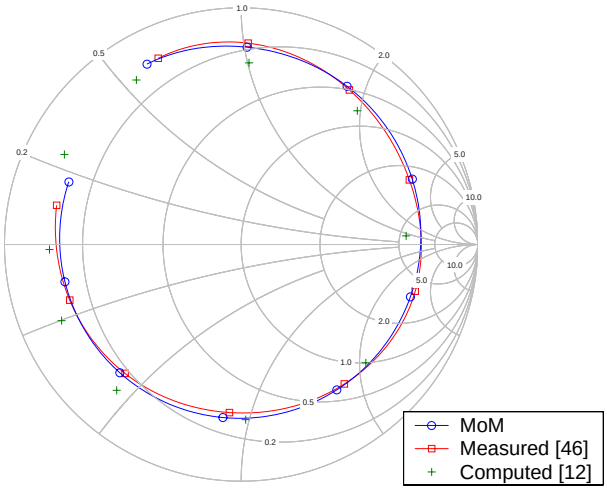

Figure 5.5: Computed and measured input impedance for an edge-fed circular patch antenna. Values are given at frequency intervals of 0.05 GHz between 2.7 and 3.15 GHz clockwise.

Good agreement between the results of the present formulation and measurement data is obtained. The substrate material used to measure the antenna had a nominal relative permittivity of $\epsilon_r = 2.2$, which is the manufacture value. The calculated reflection coefficient is obtained with a relative permittivity of $\epsilon_r = 2.18$, which is within the tolerance limits set by the manufacturer. This value was also used by [46] and [12] to align the frequencies of the computed data with those of the measured.

5.4 Suspended Stripline Transition

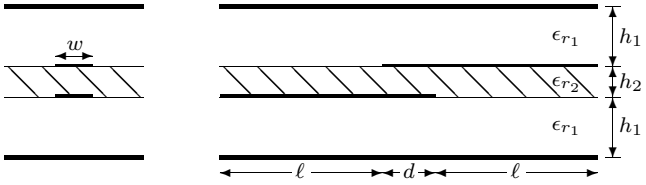

Figure 5.6: Geometry of a 3-layered suspended stripline structure ($\epsilon_{r_1} = 1$, $\epsilon_{r_2} = 3$, $h_1 = 1$ mm, $h_2 = 0.5$ mm, $w = 1$ mm, $d = 20$ mm, $\ell = 60$ mm).

This example of a suspended stripline transition was chosen to test the calculation procedure for a relatively complex geometry using multiple layers. Fig. 5.6 shows the configuration. The 3-layered structure has two air-filled layers, each of height $h_1 = 1$ mm. The third layer is a suspended substrate of relative permittivity $\epsilon_{r_2} = 3$ and thickness

$h_2 = 0.5$ mm. Two lines, each of width $w = 1$ mm, are located on opposite sides of the suspended substrate with an overlapping of $d = 20$ mm.

In Fig. 5.7 the MoM response is compared to the results obtained using Microwave Office's EM simulator, showing good agreement. Predictions deviate at higher frequencies, but still agree in the expected behaviour. The impedance normalisation method implemented by MWO is unknown and differences are expected to be the effect of this implementation. Optimal coupling between ports 1 and 2 occur at frequencies where $d = \lambda/4$ or multiples thereof. Using the structure parameters, these frequencies are predicted to be around 3 and 6 GHz. The figure shows that $|S_{12}|$ is a maximum at 2.5 and 7 GHz with good isolation of the ports at 4.5 GHz.

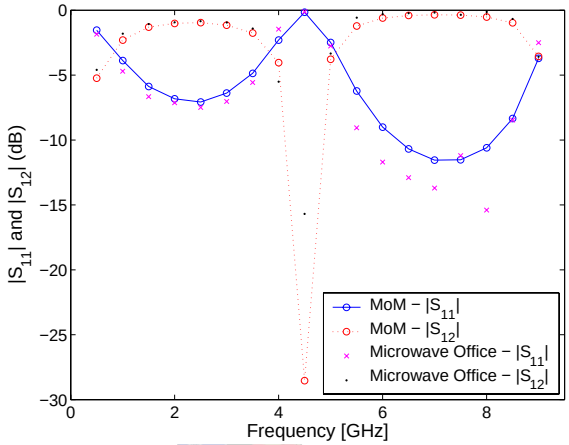

Figure 5.7: Characteristics of a suspended microstrip structure.

5.5 Short Circuits and Side Walls

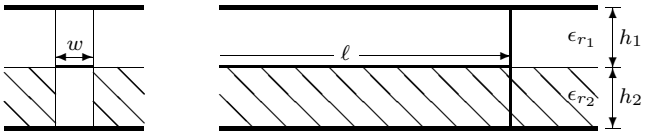

Figure 5.8: Geometry of a full height short circuit ($\epsilon_{r_1} = 1$, $\epsilon_{r_2} = 4.7$, $h_1 = 1$ mm, $h_2 = 1$ mm, $w = 1.5$ mm, $\ell = 80$ mm).

Various short-circuited structures were tested to verify implementation of extra and half subsectional basis functions (Section 4.2). The basic geometry also offers opportunity to verify parameters obtained using transmission line theory. Fig. 5.8 shows the configuration

for a full height short circuit. Substrates are of equal height $h_1 = h_2 = 1$ mm and have relative permittivities $\epsilon_{r_1} = 1$ and $\epsilon_{r_2} = 4.7$. The line has a length $\ell = 80$ mm and was divided into 54 longitudinal segments. In the transverse direction 2 square subcells spanned the width $w = 1.5$ mm.

As a first example, a half height short circuit to ground has been made through the higher permittivity substrate $\epsilon_r = 4.7$. Fig. 5.9a shows the return loss predicted by the MoM code. As expected for a short circuit, $|S_{11}|$ retains a value close to 1 over the entire tested frequency range. Fig. 5.9b shows the current magnitude distribution along the excitation port at 3 GHz. Clearly visible are the null points which are separated by half a wavelength. At this frequency the calculated effective permittivity is $\epsilon_{r,\text{eff}} = 3.06$, resulting in $\lambda = 57.17$ mm. Here λ is the wavelength at the speed of propagation. This value compares very well to the estimated value found from the half wavelength spacing in Fig. 5.9b. For a perfect short circuit, the voltage standing wave ratio (VSWR) is infinite. From the figure a best estimate of VSWR = 145 can be made. This value is limited by the discretisation along the port—even the slightest change in the null point value can have quite a big influence on the VSWR. Finally, the short circuit was characterised by a series combination of circuit elements. At 3 GHz the characteristic impedance was calculated from the structure parameters as $Z_0 = 62.25\ \Omega$. Also, with the reference plane at the short-circuited connection, $S_{11} = 0.981\angle 165.74°$. This gives an input impedance of $Z = R + j\omega L = 0.606 + j7.786$. Thus the short circuit, being imperfect, may be modelled by the combination of a 0.6 Ω resistor and an inductor of approximately 410 pH. Note that the resistive component, as expected for a short circuit, is very small.

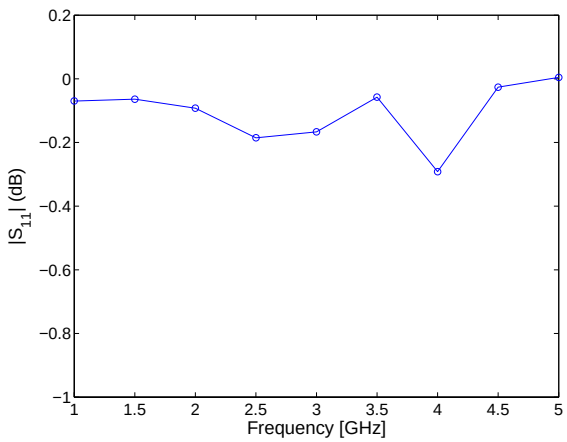

(a) Reflection coefficient magnitude.

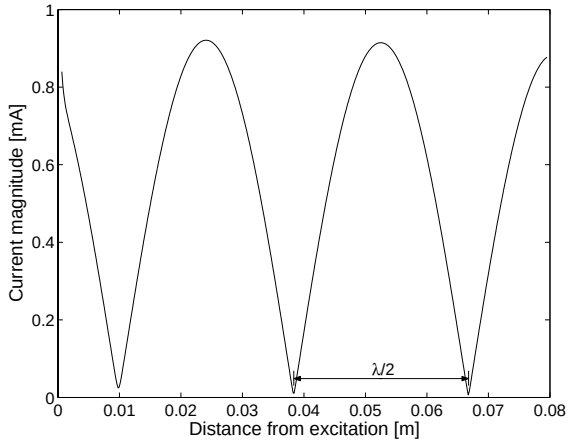

(b) Current distribution at 3 GHz. Null points are separated by $\lambda/2 = 28.51$ mm.

Figure 5.9: Characteristics of a short circuit to ground through the $\epsilon_r = 4.7$ substrate.

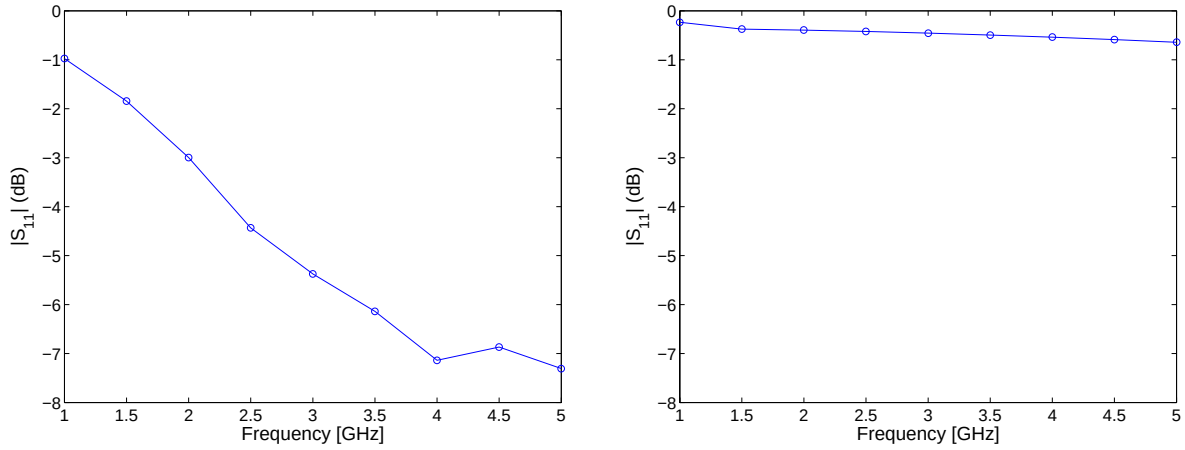

(a) $|S_{11}|$ when parallel-plate waves are propagating.

(b) $|S_{11}|$ when side walls prevent parallel-plate wave propagation.

Figure 5.10: Short circuit reflection can be improved by adding side walls. These prevent propagation of parallel-plate waves.

When the short circuit extends through the upper air-filled layer, the effect of parallel-plate wave propagation becomes apparent. A significant decrease in the magnitude of the reflection coefficient can be seen in Fig. 5.10. The wave modes correspond to the integration poles. To prevent propagation of such waves, side walls are added to the structure. The short circuit is now enclosed by an open-end waveguide that does not support the previously propagating wave-modes. Fig. 5.10b shows the improved reflection coefficient. The short circuit may once again be characterised by circuit elements. For the short circuit without walls, $S_{11} = 0.539\angle 154.02°$ at the zero length reference plane. This yields an input impedance of $Z = R + j\omega L = 19.57 + j13.006$, and the short circuit may be described by a series R-L circuit where $R = 20\ \Omega$ and $L = 690$ pH. For the enclosed short circuit, $S_{11} = 0.949\angle 156.85°$, $Z = 1.697 + j12.74$ and the circuit elements are $R = 1.7\ \Omega$ and $L = 680$ pH. Intuitively, the two short circuits should have the same inductance and, the decrease in magnitude of the reflection response should be associated with a larger resistive element. This is verified when comparing the calculated values - the two inductive elements are within 1.5 % of each other and the corresponding resistive components differ by a factor of 10.

Finally, the full height short circuit of Fig. 5.8 was analysed. Fig. 5.11 shows the return loss values obtained between 1 and 5 GHz. The up to 10% loss in the higher frequency range is due to parallel plate wave propagation. This example may also be interpreted as the superposition of the two half height short circuits previously analysed. To compare the two models, first calculate the circuit elements that model the full height geometry. At 3 GHz, calculations yield $S_{11} = 0.936\angle 170.42°$, resulting in $Z = 2.08 + j5.21$ and thus,

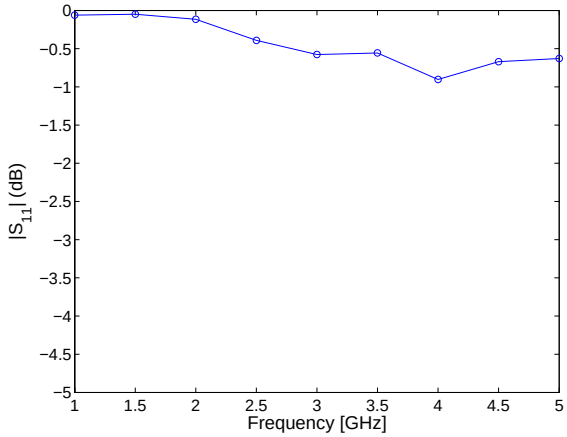

Figure 5.11: Return loss $|S_{11}|$ for a full height short circuit.

$R = 2\ \Omega$ and $L = 280$ pH. These elements are in line with circuit elements obtained when combining the models for the separate half height short circuits. Without compensating for parallel-plate wave propagation $R = 1.8\ \Omega$ and $L = 320$ pH. When using the enclosed half height short circuit, $R = 0.5\ \Omega$ and $L = 260$ pH. This final model shows a different R due to the presence of the enclosing side walls that causes a reduction in radiation.

Fig. 5.12a shows the effect of moving a grounded conducting side wall nearer to a microstrip transmission line. The MoM calculations were performed at 1 GHz and are compared to the solutions obtained using a static 2D Method of Lines (MoL) analysis [47]. Differences in the predictions may be ascribed to the variance in the effective permittivity as a function of frequency. The different plots 0.2-6 represent the varying ratio of microstrip width over microstrip height W/h.

According to [47] the relative field energy in the air space increases when bringing the side wall in close proximity to the transmission line, thus reducing the effective permittivity $\epsilon_{r,\text{eff}}$. Reductions of up to 12 % were computed while varying the normalised spacing between $d/h = 0.2$ and $d/h = 5$. For a side wall to have a negligible effect on the physical problem, the rule of thumb is that the normalised wall spacing be 5 or more. This may be verified using Fig. 5.12a—all plots start converging beyond $d/h = 2$ with the values at $d/h = 5$ very close to the estimate converging limits.

A question was posed as to how fine the side wall should be meshed to obtain accurate results. Fig. 5.12b analysed convergence of the effective dielectric permittivity by using different discretisation densities. Calculations were done at 1 GHz on a ceramic substrate of $\epsilon_r = 9.8$ and thickness $h = 1.27$ mm. The microstrip transmission line had a width of $w = 1.27$ mm and a length $\ell = 30$ mm. A constant mesh divided this line into 31 longitudinal segments and 2 square subcells spanned the line width. The side wall is

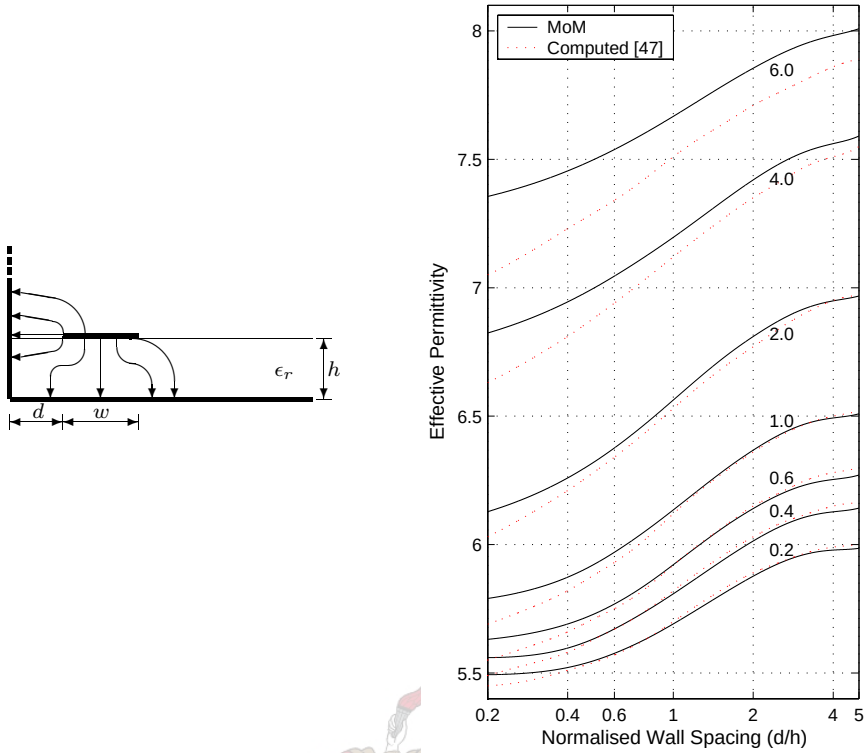

(a) Effect of a housing side wall on the effective permittivity $\epsilon_{r,\text{eff}}$ for microstrip on Al_2O_3 ceramic substrate ($\epsilon_r = 9.8$). The different plots 0.2-6 represent the varying ratio of microstrip width over substrate height w/h.

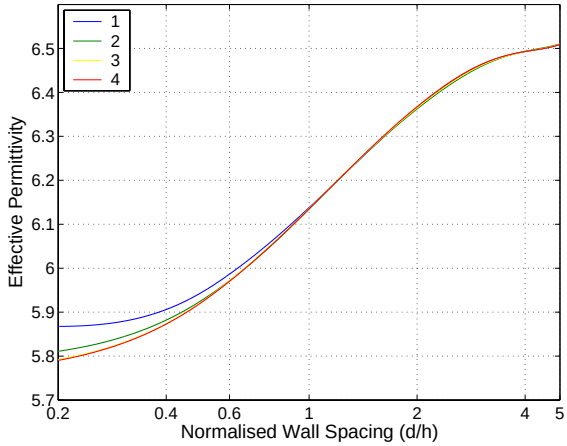

(b) Convergence of the effective permittivity by using different discretisation densities. The different plots 1-4 refer to the maximum edge lengths of $h/1$, $h/2$, $h/3$ and $h/4$ respectively.

Figure 5.12: Effects of a grounded conducting side wall on the effective permittivity for a microstrip transmission line.

assumed to be infinitely high. However, for the numerical calculations the side wall was chosen to extend twice the substrate thickness into the upper air region. This was found sufficient because of the 1:1 ratio between line width and substrate thickness.

For the numerical solution four meshes were employed. Discretisation in the longitudinal direction was held fixed using the same segment length as for the transmission line. In the direction normal to the ground plane, maximum edge lengths of $h/1$, $h/2$, $h/3$ and $h/4$ were considered. These correspond to the graphs labelled 1-4. The discretisation has little effect on the effective permittivity of the line when $d/h > 1$. This is expected because the effect of the side wall becomes less significant with increasing distance d. With the side wall close to the microstrip line, it was found that at least 2 square subcells should span the substrate height to obtain reasonable results. Fig. 5.12b suggests convergence using segment lengths of $h/3$ and finer.

5.6 Microstrip-Slot-Microstrip Transition

The main aim of this work was to implement a formulation able to solve for simultaneous electric and magnetic surface currents. This example shows the advantages of this approach, compared to formulations using only electric currents.

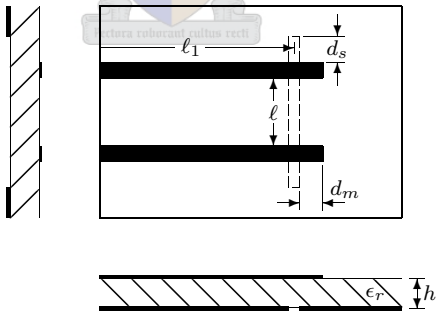

Figure 5.13: Geometry of a microstrip-slot-microstrip transition ($\epsilon_r = 11.1$, $h = 1.27$ mm, $w_m = 1.0$ mm, $w_s = 0.53$ mm, $d_m = 5.24$ mm, $d_s = 6.65$ mm, $\ell = 20.4$ mm).

A coupler with geometry shown in Fig. 5.13 was analysed using a combined electric and magnetic current discretisation. The dielectric substrate has a relative permittivity of $\epsilon_r = 11.1$ and a thickness of $h = 1.27$ mm. The dimensions for the microstrip lines are width $w_m = 1.0$ mm, stub length $d_m = 5.24$ mm and line separation $\ell = 20.4$ mm. The dimensions for the slotline are width $w_s = 0.53$ mm and stub length $d_s = 6.65$ mm. The

reference plane for evaluating the S-parameters were set at a length $\ell_1 = 40.265$ mm from the centre of the slotline.

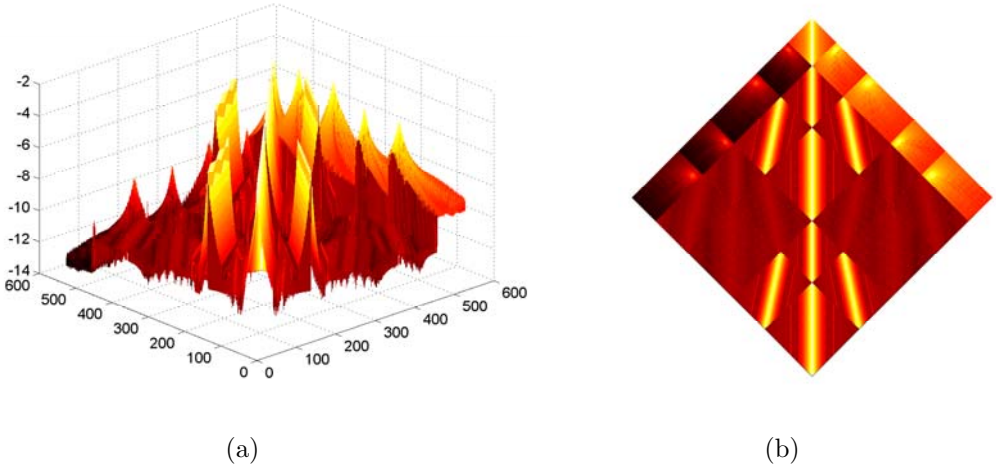

(a) (b)

Figure 5.14: Impedance matrix.

A typical partitioned impedance matrix is plotted in Fig. 5.14. The diagonal elements are the largest by an order of magnitude. It appears evident from the figure that interactions electrically distant have little influence and may possibly even be ignored. This justifies the sliding scale approach (Section 4.5) used for integrations between near and far interactions to save computer time. For the combination of electric and magnetic surface currents, symmetry in the matrix is lost. From Fig. 5.14b four main regions are visible. These correspond to symmetric interactions $J - J$ and $M - M$; and non-symmetric interactions $J - M$ and $M - J$. The notation $J - M$ means that the observation triangle supports an electric current distribution and the source triangle supports a magnetic current distribution.

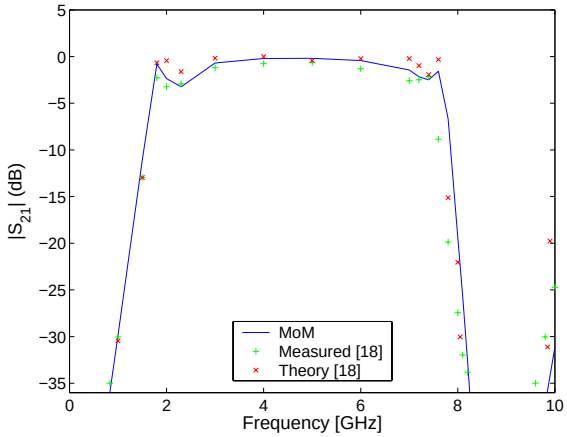

Figure 5.15: Measured and calculated transmission coefficient of a microstrip-slot-microstrip transition.

Fig. 5.15 demonstrates the computed transmission coefficient between ports 1 and 2 with the insertion loss being 0.2 dB. This microstrip-slotline-microstrip transition was also investigated theoretically and verified experimentally by Schwab and Menzel [18]. The results obtained compare well with the MoM technique employed in this thesis.

To justify discretisation of the slotline and hence, the use of the complete MPIE utilising both electric and magnetic surface currents, an alternative mesh has been investigated. This approach requires discretisation of a finite size ground plane. In these two procedures a play-off exist between the number of triangles describing the mesh, i.e. the matrix size; and the efficiency with which the matrix can be filled.

Geometry discretisation	Number of triangles	Number of unknowns	Matrix fill time	Matrix solve time
Slot	156e+60m	154e+59m	54 min 50 sec	0.03 sec
GP - $\lambda_0/10$	724	1002	2 hrs 24 min	3.63 sec
GP - $\lambda_0/15$	1512	2147	8 hrs 12 min	35.34 sec
GP - $\lambda_0/20$	2524	3627	20 hrs 16 min	4 min 20 sec
GP - $\lambda_0/10$ fine	832	1161	3 hrs 2 min	5.55 sec
GP - $\lambda_0/15$ fine	1668	2378	9 hrs 46 min	49.83 sec

Table 5.1: Comparison of matrix data for different discretisation densities. Here GP - $\lambda_0/10$ refers to a uniform discretisation of a finite size ground plane with maximum edge length equal to $\lambda_0/10$ and λ_0 the free-space wavelength at 10 GHz. CPU time is for a single frequency point.

In the numerical solution for the finite size ground plane a variety of discretisation densities have been considered, namely, $\lambda_0/10$, $\lambda_0/15$, $\lambda_0/20$ and two approaches defining a finer mesh around the slot. The nonuniform discretisation was considered necessary to accurately account for the coupling in the slot. Only a limited number of frequency points were evaluated and data obtained are listed in Table 5.1. Important results for comparison are the number of unknowns in the mesh and the matrix fill time per frequency point.

Fig. 5.16 compares the transmission responses obtained for the ground plane ($\lambda_0/10$ and $\lambda_0/10$ fine) meshes with the response obtained using the proposed magnetic current solution in the slot. Both ground plane discretisations show the general behaviour, with larger deviations at higher frequencies. This is an indication that especially for the higher frequencies, an even finer mesh should be employed. The $\lambda_0/10$ discretisation also fails to predict the peak at 1.8 GHz. Because of the times required to perform evaluations with finer meshes, comparitive results are not included.

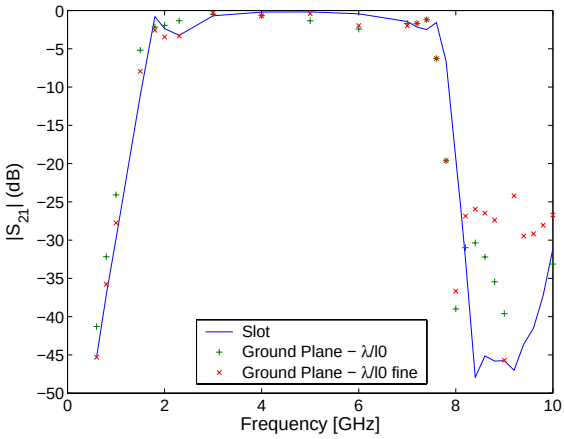

Figure 5.16: Transmission responses obtained when meshing a finite size ground plane.

Considering the computational predictions shown in Fig. 5.15 and the comparison of matrix fill times in Table 5.1, the choice would be to fill smaller matrices using the MoM formulation that solves for simultaneous electric and magnetic currents.

5.7 Multi-Layered Microstrip-Slot-Microstrip Transitions

As a final example, two multi-layered combined electric and magnetic current discretisation problems are analysed. Figs. 5.17a and b explain the different configurations. These two problems are physically equivalent with exception to the port directions. Each example consists of a double dielectric substrate of relative permittivity $\epsilon_r = 11.1$ and thickness $h = 1.27$ mm, which are separated by a slotline in an infinite electrical ground plane. The dimensions for the microstrip lines are width $w_m = 1.0$ mm and stub length $d_m = 5.24$ mm. For the slotline the dimensions are width $w_s = 0.53$ mm and slot stub length $d_s = 6.65$ mm. All reference planes for evaluating the S-parameters were set at lengths $\ell = 40.265$ mm from the centre of the slotline. Each port was divided into 46 longitudinal and 2 transverse segments, while the slot was divided into 30 triangles.

Fig. 5.18 shows a typical plot of the impedance matrix associated with the two geometries of Fig. 5.17. Both examples were separated into two microstrip geometries which are solved independently. Coupling is obtained when continuity of the magnetic surface currents is enforced at the slotline interface. In the impedance matrix the two black squares represent areas of isolation in the testing procedure.

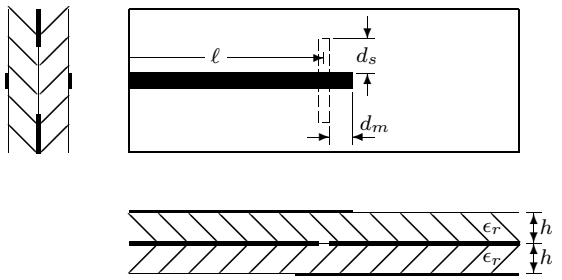

(a)

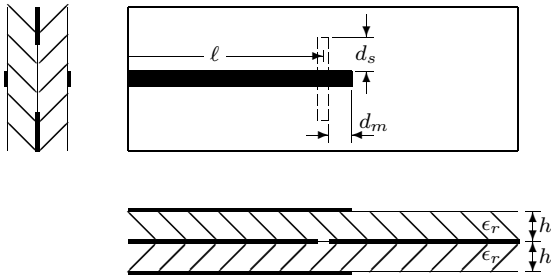

(b)

Figure 5.17: Geometries of two multi-layered microstrip-slot-microstrip transitions ($\epsilon_r = 11.1$, $h = 1.27$ mm, $w_m = 1.0$ mm, $w_s = 0.53$ mm, $d_m = 5.24$ mm, $d_s = 6.65$ mm, $\ell = 40.265$ mm).

In Figs. 5.19a and b the MoM response is compared to a Finite Difference Time Domain prediction generated by the commercial software package CST Microwave Studio Version 3. Both examples demonstrate excellent agreement in the responses obtained. It was expected that the magnitude responses for the examples of Fig. 5.17 should be the same. At higher frequencies there are visible differences in the results generated by the Microwave Studio code. These ripple effects may be a result of the enclosing PEC cavity required by the simulation setup. The simulations were also optimise for error in the discretisation. For a less fine discretisation used in the Microwave Studio simulation, differences in the 4-6 GHz range for the $|S_{11}|$ response were less, implying that more accurate results in the MoM solution is also possible for finer discretisations.

To confirm that the magnitude responses for both examples are the same, Fig. 5.20a gives a combined plot of the MoM responses for Examples 1 and 2 corresponding to the geometries of Fig. 5.17a and b respectively. The S_{21} phase responses for the two examples differ by a constant 180° across the band. This is due to the different exit points of the problems. The phase is shown in Fig. 5.20b and is compared to the results obtained for the cavity enclosed problems simulated using Microwave Studio.

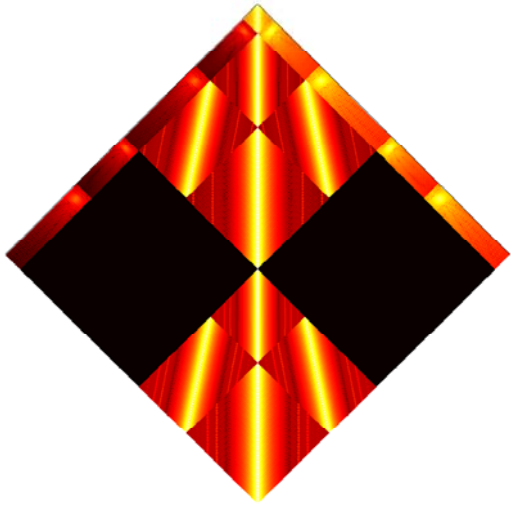

Figure 5.18: Impedance matrix.

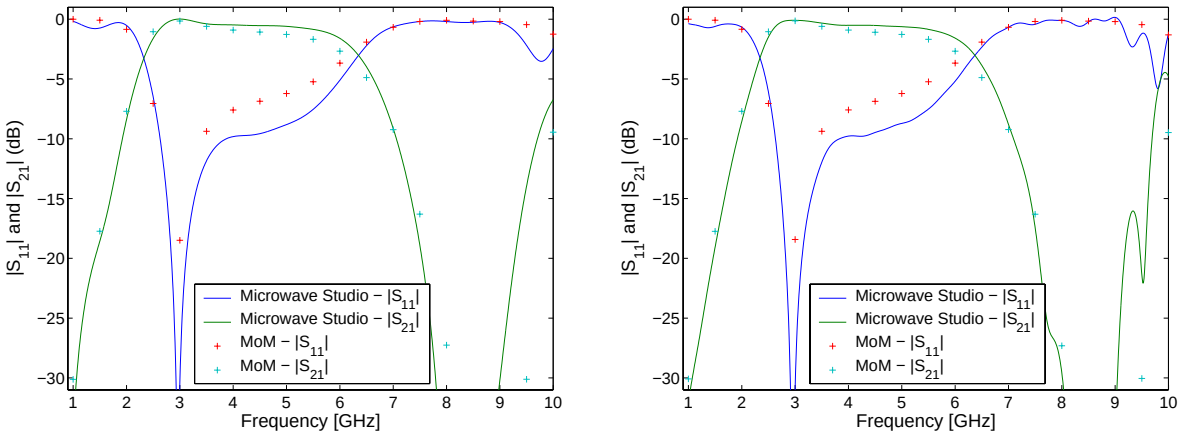

(a) Magnitude response for Fig. 5.17a.

(b) Magnitude response for Fig. 5.17b

Figure 5.19: Computed frequency responses for the microstrip-slot-microstrip transitions of Fig. 5.17.

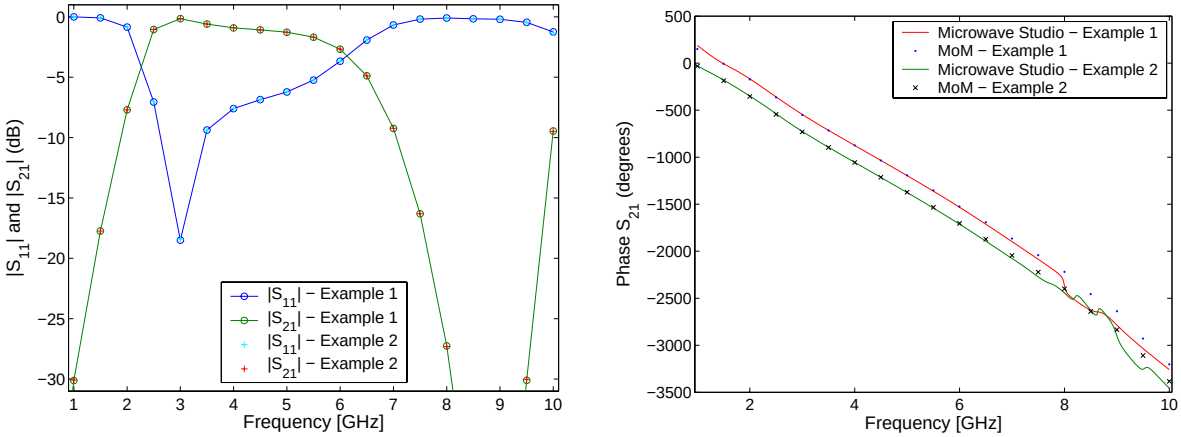

(a) Comparing magnitude responses.

(b) S_{21} phase responses.

Figure 5.20: The two multi-layered microstrip-slot-microstrip transitions of Fig. 5.17 have equal magnitude responses and their phase differ by a constant 180°.

5.8 Programming Language, Hardware Requirements and Execution Speed

The code was written in Lahey/Fujitsu Fortran, LF95 PRO v5.7c, which includes IMSL Fortran 90 MP Library v4.01. This compiler is a product of Lahey Computer Systems, Inc. The geometry was created and meshed using PreFeko, which is a commercial product of Electromagnetic Software & Systems (EMSS). Results were interpreted and graphically presented using Matlab Version 6.5 Release 13. Computations and timed executions were evaluated on an AMD Athlon 2100+ processor with 256 MB RAM.

In the method of moment code, most of the memory is used by the $\bar{\bar{Z}}$ matrix. When a problem supports both electric and magnetic unknown surface current distributions, symmetry in the global matrix is lost and the full matrix should be stored. The set of linear equations is solved using two of the IMSL complex double precision routines.

dlfccg: computes the LU factorisation of a complex general matrix and estimates its L_1 condition number.

dlfscg: solves a complex general system of linear equations given the LU factorisation of the coefficient matrix.

The $\bar{\bar{Z}}$ matrix requires memory to store N^2 double precision complex numbers, where N is the total number of basis functions. Thus, for $N = 992$, the size of the $\bar{\bar{Z}}$ matrix is 15 Mbytes. To this a small amount of overhead memory should be added.

The total solution time for the unknown surface current distribution depends mostly on the matrix fill time, which is a strong function of the time needed to evaluate the Green's functions. Approximations made have an influence on these execution times; the numerical integration method used is a function of near and far interactions, reducing computation time per element for a finer discretisation (or larger geometries).

In parallel to the memory requirements, only half the number of Green's functions need to be evaluated when the matrix is symmetric. For the combined electric and magnetic current problems, the matrix has both symmetric and non-symmetric element groups; potential Green's functions result in a double symmetric entry, whilst the Green's functions for the curl of the potentials need to be individually computed. This can cause a considerable increase in execution time.

Geometry type	Number of triangles	Number of unknowns	Matrix fill time	Matrix solve time
Straight wire	268	267	13 min 40 sec	0.06 sec
Rectangular patch	300	425	32 min 30 sec	0.28 sec

Table 5.2: Synopsis of two computational tasks. CPU time is for a single frequency point.

The total solution times to compute the surface current distribution for a single frequency point are listed for two different tasks (Table 5.2), the first is a wire type geometry and the second a wider conductor pattern. However, it is impossible to compute an average fill time per element, as the computation of the elements is dependent on convergence of the Sommerfeld integrals.

For wire type geometries where one triangle spans the width of the conductor pattern, each triangle can have up to only two adjacent triangles. The number of basis functions, N, are then approximately equal to the number of triangles, T_N. For wide conductor patterns, for example an $m \times n$ rectangular patch, each triangle can have up to three adjacent triangles. The number of triangles is $T_N = 2mn$ and the number of basis functions is $N = mn + m(n-1) + n(m-1)$. For large m and n, the number of basis functions is $N \approx 1.5T_N$. The number of basis functions therefore depends on the geometry and can vary between

$$1 < \frac{N}{T_N} < 1.5. \tag{5.2}$$

For wire type conductor patterns the ratio is close to 1, and for rectangular solid conductor patterns this ratio can be as high as 1.5.

5.9 Conclusion

The triangular moment method presented in this dissertation can be used to successfully predict the scattering parameters (both magnitude and phase) of multi-layered open or closed structures. Some differences are observed, but the general accuracy is very good.

The calculation of the effective permittivity in structures has received much attention in the literature. The code successfully (and with high accuracy) computed this parameter for a microstrip line. Also for microstrip structures, radiation and surface wave loss have been accurately predicted and verified. The computational predictions for a multi-layered coupling structure has been compared, with good agreement, to results obtained using commercial software. A further analysis tested and verified correct implementation for vertical scatterers and special basis functions. This included the effect of a grounded side wall being moved closer to or further apart from a microstrip line. Finally, two microstrip-slot-microstrip transitions have been analysed to illustrate the use of the MoM for combined electric and magnetic current problems. Comparison with results from the literature and using commercial software show excellent correspondence. Advantages of this approach, compared to formulations using only electric currents, are highlighted.

Performance of the implemented method has been discussed and measured against criteria such as memory usage and execution speed.

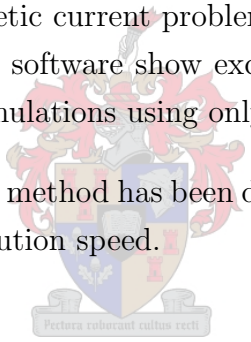

Chapter 6

General Conclusion

6.1 Recommendations

The MoM code has been implemented as the first phase of a simulation tool, which can be exploited when skillfully used by its users. The code does have limitations and it would be worthwhile focusing attention on specific details.

Execution of tasks is a time consuming process. The code runs on a personal computer, but for large problems execution speed becomes a problem—in the commercial world no user wishes to wait hours or even days to complete a simulation run. A commonly encountered solution for this problem is to perform interpolations using preestablished look-up tables [35, 48, 49]. The Green's functions are a weak function of the geometry, and should be computed and tabulated for discrete ρ, ranging from $\rho = 0$ to the maximum distance between any two points on the conductor (or slot) interfaces. With this method only a limited number of Green's functions need to be evaluated and the matrix would be filled using three-dimensional interpolation. This will result in a tremendous improvement of the execution speed.

Different techniques for extracting scattering parameters should be exploited. The present technique works well, but requires port lengths of at least a quarter wavelength. Also, because S-parameters are very sensitive to errors, a much finer mesh and thus also longer execution times are needed. The technique also relies on an optimisation process to correctly find parameter values. Different approaches may be used to verify the implemented technique, but also to characterise N-port networks utilising physical symmetries and to possibly interpolate frequency behaviour.

Various numerical issues had to be carefully considered. Computationally there is a limit

when storing large values—infinity is simply not a possibility. For the integration process up to infinity ($k_\rho \to \infty$), Mosig's Method of Averages was implemented. If and when numerical overflow is encountered, integration is performed up to the maximum permitted value ($k_{\rho,\text{inf}}$), which is then assumed to be the numerical equivalent of infinity. Alongside of this, the question of accuracy should be mentioned. Different integration algorithms have been tested, only one of which was implemented recursively and terminated to a specified tolerance. This implementation was, however, too time intensive to be given further consideration. The other implementations focussed on a fixed number of points per integration interval (Simpson's rule; trapezium rule; and a very limited form of a look-up table and interpolation methods). Simpson's rule was implemented as the best choice to approximate the kernel integrands, which are a strong function of the Bessel function half-period. The above-mentioned numerical problems were given the necessary attention, but may not be fully solved. A detailed analysis of the integration process and its effects on accuracy can still be conducted with findings being incorporated and combined into the present code.

As an extension to this thesis, the near- and far-fields of an arbitrarily shaped object embedded in a multi-layered substrate should be computed. The total field Green's functions for planar media were theoretically derived in Appendix G, and in Appendix H the near-field static terms are extracted from the field Green's functions. These are in a suitable form to be used with the present method of moment formulation. Van Tonder [24] developed code and verified the procedure for planar antennas buried in layered media. The observation point can be within any layer and at any distance within each layer, allowing the total fields to be computed anywhere within the geometry.

6.2 Conclusion

In this thesis a full-wave Method of Moments analysis of arbitrary objects embedded in multi-layered media is presented. The mixed-potential integral equation formulation for infinite open planar structures is extended to account for the effects of horizontal and vertical shielding structures and makes provision for simultaneous electric and magnetic currents. Electric surface currents are introduced on the surface of conducting apertures and magnetic surface currents are introduced at slotline interfaces. This approach eliminates meshing of ground planes altogether. Vertical shielding walls are meshed and connected to horizontal conducting materials through half and multiple basis functions.

Development of the Sommerfeld type Green's functions for planarly layered media is presented in some detail. Further insight into the problem is also provided using asymptotic

expansion methods to simplify these integrals.

The formulation was evaluated by analysing a number of geometries and predicting the scattering parameters. Excellent agreement with measured and numerical data from the literature was obtained in both amplitude and phase.

The code developed is expected to be a valuable simulation tool within an academic environment. A limit to larger practical applications would be the execution time required to solve a problem. However, access to the programme code creates opportunity for its users to exploit specific properties in computational analyses.

Appendix A

Fourier transforms

A.1 Definition of the Fourier transform

The multi-layered medium defined in Section 2.1 extend to infinity in the transverse directions. It is convenient to introduce a two-dimensional Fourier transform pair changing space variables x and y to their spectral counterparts k_x and k_y

$$\tilde{f}(k_x, k_y, z) = \frac{1}{2\pi} \int_{-\infty}^{\infty} \int_{-\infty}^{\infty} f(x, y, z) e^{-jk_x x - jk_y y} dx dy \tag{A.1}$$

where $\tilde{f}(k_x, k_y, z)$ is the Fourier transform of $f(x, y, z)$.

The inverse Fourier transform is

$$f(x, y, z) = \frac{1}{2\pi} \int_{-\infty}^{\infty} \int_{-\infty}^{\infty} \tilde{f}(k_x, k_y, z) e^{jk_x x + jk_y y} dk_x dk_y. \tag{A.2}$$

A.2 Transforms of derivatives

Using the linearity of the Fourier transform, it is found that [50]

$$\mathcal{F}[\frac{\partial^n}{\partial x^n} f(x, y, z)] = (jk_x)^n \tilde{f}(k_x, k_y, z). \tag{A.3}$$

Derivatives with respect to y have the same form. For derivatives with respect to z, however, the integration and differentiation can be interchanged as the integration is independent of z

$$\mathcal{F}[\frac{\partial^n}{\partial z^n} f(x, y, z)] = \frac{\partial^n}{\partial z^n} \tilde{f}(k_x, k_y, z). \tag{A.4}$$

A.3 Inverse Fourier identities

When the medium is translationally invariant in the x and y directions, the variables k_x and k_y occur in the form $k_\rho^2 = k_x^2 + k_y^2$. The following useful inverse Fourier transforms hold [51]

$$\begin{aligned}
\mathcal{F}^{-1}\{\tilde{f}(k_\rho)\} &= \int_0^\infty J_0(k_\rho\rho)k_\rho\tilde{f}(k_\rho)dk_\rho \\
\mathcal{F}^{-1}\{jk_x\tilde{f}(k_\rho)\} &= -\cos\phi\int_0^\infty J_1(k_\rho\rho)k_\rho^2\tilde{f}(k_\rho)dk_\rho \\
\mathcal{F}^{-1}\{jk_y\tilde{f}(k_\rho)\} &= -\sin\phi\int_0^\infty J_1(k_\rho\rho)k_\rho^2\tilde{f}(k_\rho)dk_\rho \\
\mathcal{F}^{-1}\{k_xk_y\tilde{f}(k_\rho)\} &= \sin\phi\cos\phi\int_0^\infty \left[J_0(k_\rho\rho)k_\rho^3 - \frac{2}{\rho}J_1(k_\rho\rho)k_\rho^2\right]\tilde{f}(k_\rho)dk_\rho \\
\mathcal{F}^{-1}\{k_x^2\tilde{f}(k_\rho)\} &= \int_0^\infty \left[\cos^2\phi J_0(k_\rho\rho)k_\rho^3 - \frac{\cos 2\phi}{\rho}J_1(k_\rho\rho)k_\rho^2\right]\tilde{f}(k_\rho)dk_\rho \\
\mathcal{F}^{-1}\{k_y^2\tilde{f}(k_\rho)\} &= \int_0^\infty \left[\sin^2\phi J_0(k_\rho\rho)k_\rho^3 + \frac{\cos 2\phi}{\rho}J_1(k_\rho\rho)k_\rho^2\right]\tilde{f}(k_\rho)dk_\rho.
\end{aligned} \tag{A.5}$$

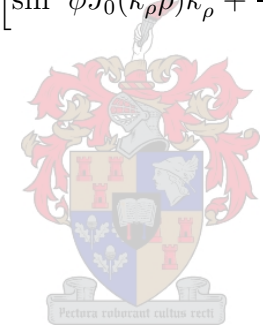

Appendix B

Potentials in terms of the Normal Field Components

The dyadic for the vector potential $\bar{\bar{\mathbf{G}}}_A$, in the traditional Sommerfeld approach for stratified media, is given by

$$\bar{\bar{\mathbf{G}}}_A = \hat{\mathbf{x}} G_A^{xx} \hat{\mathbf{x}} + \hat{\mathbf{y}} G_A^{yy} \hat{\mathbf{y}} + \hat{\mathbf{z}} (G_A^{zx} \hat{\mathbf{x}} + G_A^{zy} \hat{\mathbf{y}} + G_A^{zz} \hat{\mathbf{z}}). \tag{B.1}$$

These quantities can be written in terms of the normal components of the fields [24], [30].

The electric and magnetic fields in the space domain may be derived as a function of the magnetic vector and electric scalar potentials, $\mathbf{A}$ and Φ respectively. Subject to the Lorenz condition $j\omega\mu\epsilon\Phi + \nabla \cdot \mathbf{A} = 0$, valid relationships between the fields and potential functions are [28]

$$\begin{aligned} \mu \mathbf{H} &= \nabla \times \mathbf{A} \\ \mathbf{E} &= -j\omega \mathbf{A} - \nabla \Phi. \end{aligned} \tag{B.2}$$

It is also known that the scalar potential of a unit point charge G_Φ is related to the scalar potential Φ of a time-harmonic dipole pointing in the $\hat{\boldsymbol{\alpha}}$ direction. The relation is given by [29]

$$\Phi = -\frac{1}{j\omega} \nabla G_\Phi \cdot \hat{\boldsymbol{\alpha}} = \frac{1}{j\omega} \nabla' G_\Phi \cdot \hat{\boldsymbol{\alpha}}, \tag{B.3}$$

where ∇' acts on the primed source coordinates.

Now, given the two normal field components E_z and H_z, the four transverse components of the electromagnetic field can be derived in a homogeneous layer. Using Maxwell's

equations for a source-free region and the Fourier transform pair given by

$$\begin{aligned}\tilde{f}(k_x,k_y,z) &= \frac{1}{2\pi}\int_{-\infty}^{\infty}\int_{-\infty}^{\infty} f(x,y,z)e^{-jk_x x - jk_y y}dxdy \\ f(x,y,z) &= \frac{1}{2\pi}\int_{-\infty}^{\infty}\int_{-\infty}^{\infty} \tilde{f}(k_x,k_y,z)e^{jk_x x + jk_y y}dk_x dk_y,\end{aligned} \tag{B.4}$$

the transverse components in the spectral domain are given by [52]

$$\begin{aligned}k_\rho^2\tilde{E}_x &= jk_x\dot{\tilde{E}}_z + \omega\mu k_y\tilde{H}_z \\ k_\rho^2\tilde{E}_y &= jk_y\dot{\tilde{E}}_z - \omega\mu k_x\tilde{H}_z \\ k_\rho^2\tilde{H}_x &= jk_x\dot{\tilde{H}}_z - \omega\epsilon k_y\tilde{E}_z \\ k_\rho^2\tilde{H}_y &= jk_y\dot{\tilde{H}}_z + \omega\epsilon k_x\tilde{E}_z.\end{aligned} \tag{B.5}$$

Here the tilde ($\tilde{}$) denotes a spectral quantity, and $\dot{\psi} = \frac{\partial\psi}{\partial z}$ where ψ represents either $\tilde{E}_z$ or $\tilde{H}_z$ in Eqn. B.5.

Using the relations B.2, B.3 and B.5, the potentials can be written in the spectral domain, and in terms of the normal components of field. Note that alternative solutions are found when choosing a different dyadic for the vector potential. The solution presented here proceeds using the traditional Sommerfeld approach. Also, the the magnetic current $\mathbf{M}$ and the electric vector potential $\mathbf{F}$ have been assumed to be zero.

To complete the derivation, an understanding of the field to dyadic Green's function relation is required. From the point of view of the Green's functions, the normal components of the fields are

$$\begin{aligned}\hat{\mathbf{z}}\cdot\bar{\bar{\mathbf{G}}}_E &= G_E^{zx}\hat{\mathbf{x}} + G_E^{zy}\hat{\mathbf{y}} + G_E^{zz}\hat{\mathbf{z}} \\ \hat{\mathbf{z}}\cdot\bar{\bar{\mathbf{G}}}_H &= G_H^{zx}\hat{\mathbf{x}} + G_H^{zy}\hat{\mathbf{y}}.\end{aligned} \tag{B.6}$$

Thus, a specific field comprises those fields produced by individually x, y and z directed sources. Note that $G_H^{zz} = 0$ because a vertical source in a stratified medium does not produce a vertical magnetic field.

Now, the transverse components of $\bar{\bar{\mathbf{G}}}_E$ and $\bar{\bar{\mathbf{G}}}_H$ are obtained from the normal components by using Eqn. B.5 with $\tilde{E}_s$, $\tilde{H}_s$ ($s = x,\ y$) formally replaced by $\hat{\mathbf{s}}\cdot\bar{\bar{\mathbf{G}}}_E$, $\hat{\mathbf{s}}\cdot\bar{\bar{\mathbf{G}}}_H$, giving

$$\begin{aligned}k_\rho^2\tilde{G}_E^{xx} &= jk_x\dot{\tilde{G}}_E^{zx} + \omega\mu k_y\tilde{G}_H^{zx} \\ k_\rho^2\tilde{G}_E^{yy} &= jk_y\dot{\tilde{G}}_E^{zy} - \omega\mu k_x\tilde{G}_H^{zy} \\ k_\rho^2\tilde{G}_H^{xx} &= jk_x\dot{\tilde{G}}_H^{zx} - \omega\epsilon k_y\tilde{G}_E^{zx} \\ k_\rho^2\tilde{G}_H^{yy} &= jk_y\dot{\tilde{G}}_H^{zy} + \omega\epsilon k_x\tilde{G}_E^{zy}.\end{aligned} \tag{B.7}$$

The three components of the vector equation $\mu\mathbf{H} = \nabla \times \mathbf{A}$ can be reduced and written in the spectral domain as

$$\begin{aligned}\mu\tilde{H}_x &= jk_y\tilde{A}_z - \frac{\partial}{\partial z}\tilde{A}_y \\ \mu\tilde{H}_y &= \frac{\partial}{\partial z}\tilde{A}_x - jk_x\tilde{A}_z \\ \mu\tilde{H}_z &= jk_x\tilde{A}_y - jk_y\tilde{A}_x.\end{aligned} \tag{B.8}$$

Similarly, from $\mathbf{E} = -j\omega\mathbf{A} - \nabla\Phi$, and substituting the Lorenz gauge

$$\begin{aligned}\tilde{E}_z &= -j\omega\tilde{A}_z - \nabla\Phi \\ &= -j\omega\tilde{A}_z + \frac{1}{j\omega\mu\epsilon}\frac{\partial}{\partial z}(jk_x\tilde{A}_x + jk_y\tilde{A}_y + \frac{\partial}{\partial z}\tilde{A}_z).\end{aligned} \tag{B.9}$$

In terms of the field and potential Green's functions for a horizontal source Eqn. B.8 can be written as

$$\begin{aligned}\mu\tilde{G}_H^{xx}\hat{\mathbf{x}} + \mu\tilde{G}_H^{xy}\hat{\mathbf{y}} &= jk_y(\tilde{G}_A^{zx}\hat{\mathbf{x}} + \tilde{G}_A^{zy}\hat{\mathbf{y}}) - \frac{\partial}{\partial z}\tilde{G}_A^{yy}\hat{\mathbf{y}} \\ \mu\tilde{G}_H^{yx}\hat{\mathbf{x}} + \mu\tilde{G}_H^{yy}\hat{\mathbf{y}} &= \frac{\partial}{\partial z}\tilde{G}_A^{xx}\hat{\mathbf{x}} - jk_x(\tilde{G}_A^{zx}\hat{\mathbf{x}} + \tilde{G}_A^{zy}\hat{\mathbf{y}}) \\ \mu\tilde{G}_H^{zx}\hat{\mathbf{x}} + \mu\tilde{G}_H^{zy}\hat{\mathbf{y}} &= jk_x\tilde{G}_A^{yy}\hat{\mathbf{y}} - jk_y\tilde{G}_A^{xx}\hat{\mathbf{x}},\end{aligned} \tag{B.10}$$

and for a vertical source, Eqn. B.9 is equivalent to

$$\tilde{G}_E^{zz}\hat{\mathbf{z}} = -j\omega\tilde{G}_A^{zz}\hat{\mathbf{z}} - \frac{k_z^2}{j\omega\mu\epsilon}\tilde{G}_A^{zz}\hat{\mathbf{z}}. \tag{B.11}$$

The final step involves substituting B.7 into B.10 and B.11. Solving for the potentials yield

$$\begin{aligned}\tilde{G}_A^{xx} &= -\frac{\mu}{jk_y}\tilde{G}_H^{zx} \\ \tilde{G}_A^{yy} &= \frac{\mu}{jk_x}\tilde{G}_H^{zy} \\ k_\rho^2\tilde{G}_A^{zx} &= j\omega\mu\epsilon\tilde{G}_E^{zx} + \frac{k_x\mu}{k_y}\frac{\partial}{\partial z}\tilde{G}_H^{zx} \\ k_\rho^2\tilde{G}_A^{zy} &= j\omega\mu\epsilon\tilde{G}_E^{zy} - \frac{k_y\mu}{k_x}\frac{\partial}{\partial z}\tilde{G}_H^{zy} \\ k_\rho^2\tilde{G}_A^{zz} &= j\omega\mu\epsilon\tilde{G}_E^{zz}.\end{aligned} \tag{B.12}$$

To obtain the equation for the scalar potential of a point charge associated with an x directed horizontal dipole, use the Lorenz condition and the relation B.3, i.e.,

$$\Phi = \frac{j\omega}{k^2}\nabla\cdot\mathbf{A} = -\frac{1}{j\omega}\nabla G_\Phi\cdot\hat{\mathbf{x}} \tag{B.13}$$

From the equivalent Green's function point of view

$$\frac{j\omega}{k^2}(jk_x\tilde{G}_A^{xx} + \frac{\partial}{\partial z}\tilde{G}_A^{zx}) = -\frac{1}{j\omega}jk_x\tilde{G}_\Phi. \tag{B.14}$$

Substituting appropriate results from B.12 and solving for $\tilde{G}_\Phi$, gives

$$\tilde{G}_\Phi = \frac{j\omega}{k_\rho^2 jk_x}\frac{\partial}{\partial z}\tilde{G}_{EJ}^{zx} - \left(\frac{k}{k_\rho}\right)^2\frac{1}{jk_{y\epsilon}}\tilde{G}_{HJ}^{zx}. \tag{B.15}$$

This completes the spectral domain relations for the potentials written in terms of the normal field components.

Appendix C

Packing of the Moment Matrix

Consider Fig. C.1, where q is the source triangle, and p is the observation triangle. The non-boundary sides of q are labelled a, b and c, indicating the number of the basis function spanning that edge. Similarly x, y and z are the basis functions associated with triangle p.

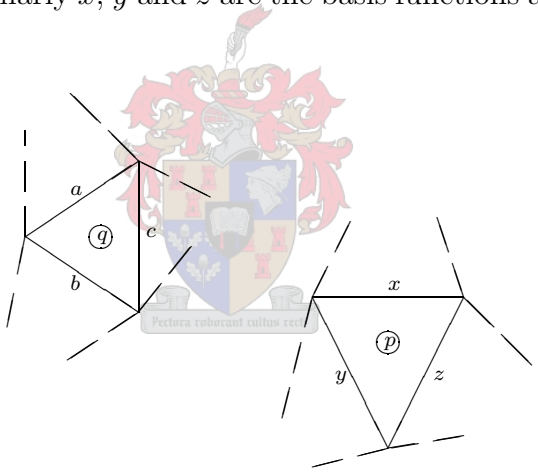

Figure C.1: Triangle pair p and q.

Assume that the surface currents associated with these triangles are electric. By default, the integrals $\mathbf{I}^{pq}_{A\xi}$, $\mathbf{I}^{pq}_{A\eta}$ and $\mathbf{I}^{pq}_{A}$ of Eqn. 4.44 and I^{pq}_{Φ} of Eqn. 4.46, contribute in up to nine elements of the $\bar{\bar{Z}}$ matrix (subscripts distinguish between different simplex coordinate potential integrals, while the superscript identifies the observer to source face-pair combination). When extra basis functions are spanning a particular triangle edge, the computed integrals can contribute to even more elements; this again justifies computing the potential integrals by face-pair combinations, rather than by edge-pair combinations. When the source and observation triangles support different type currents, magnetic and electric respectively, the double integral P^{pq} of Eqn. 4.47 will in a similar way contribute to various elements of the $\bar{\bar{Z}}$ matrix. For example, if I^{pq} represents the contribution of the

associated curl, vector or scalar potential quantity, then I^{pq} contributes to the following Z_{uv} elements

$$I^{pq} \rightarrow \begin{bmatrix} Z_{xa} & Z_{xb} & Z_{xc} \\ Z_{ya} & Z_{yb} & Z_{yc} \\ Z_{za} & Z_{zb} & Z_{zc} \end{bmatrix}. \tag{C.1}$$

To indicate to which Z_{uv} elements a triangle contributes, define a connection matrix T

$$T = \begin{bmatrix} & \vdots & \\ a & b & c \\ & \vdots & \\ x & y & z \\ & \vdots & \end{bmatrix} \begin{matrix} \\ \\ \rightarrow \text{row } q \\ \\ \rightarrow \text{row } p \\ \\ \end{matrix} \tag{C.2}$$

where T is an $N_T \times N_{BF}$ matrix. N_T is the total number of triangles in the structure and N_{BF} is the maximum number of basis functions associated with any triangle. As a default N_{BF} is set to 3. Therefore, the q^{th} row for the matrix T indicates that triangle q is spanned by basis functions a, b and c. A few special cases should be mentioned. If triangle q has only one non-boundary edge, say a, then the other two matrix elements will be zero, $[\,a\ 0\ 0\,]$. If the triangle is spanned by an extra basis function, say c and d share the same physical edge, then N_{BF} should be increased to permit entering all basis functions spanning that triangle, $[\,a\ b\ c\ d\,]$. Note that all non-boundary edges must have a double entry into the connection matrix. When a triangle is connected to a PEC, a half basis function is defined and a single matrix entry is made to associate this connecting edge with one triangle only.

A generalised approach to packing the $\bar{\bar{Z}}$ matrix has been developed. The proposed solution differs from the one introduced by Van Tonder [24] in that multiple problems, all stacked and separated by a PEC, can now be simultaneously solved by filling only one large matrix. Also, the filling algorithm efficiently packs partially symmetric matrices, which are present when solving problems that support a combination of electric and magnetic currents. In the presence of only electric (or magnetic) type currents, the contribution of an element such as I^{pq} in the $\bar{\bar{Z}}$ matrix can be efficiently evaluated - it is sufficient to evaluate only the upper (or lower) triangle elements and then simply enforce symmetry by casting computed values to their symmetric counterparts. This describes the essence of the approach used in [24]. When a problem supports both electric and magnetic surface currents, the $\nabla \times \mathbf{A}$ and $\nabla \times \mathbf{F}$ terms in Eqn. 4.9 disrupt symmetry in the moment matrix. From the definition of the partitioned matrix, Eqn. 4.30, it follows that subsectional symmetric matrices still exist within the global one. The packing scheme developed aims at utilising efficient evaluation techniques for filling these symmetric matrices, within the

global filling procedure.

In pseudo-code the complete packing scheme may be described as

```
for prCnt = 1 to N_Problems
   K = 1
   for pCnt = 1 to prN_T
      p = triList(prCnt, pCnt)
      for qCnt = pCnt to prN_T
         q = triList(prCnt, qCnt)
         for Cnt = 1 to 2
            for pp = 1 to N_BF
               u = T(p, pp)
               if u = 0, then break pp
               for qq = 1 to N_BF
                  v = T(q, qq)
                  if v = 0, then break qq
                  if p = q and u > v, then K = 0
                  if p ≠ q and u = v, then K = 2†
                  U = min[u, v]
                  V = max[u, v]
                  if triType(p) = 'M' and triType(q) = 'J', then
                     V = min[u, v]
                     U = max[u, v]
                  end if
                  Zuv(U, V) = Zuv(U, V) + KI^pq
                  if triType(p) = triType(q), then Zuv(V, U) = Zuv(U, V)
                  K = 1
               next qq
            next pp
            if triType(p) ≠ triType(q), then swop(p, q)
            if triType(p) = triType(q), then break Cnt
         next Cnt
      next qCnt
   next pCnt
next prCnt.
```

(C.3)

Note that the loop involving $qCnt$ only runs from $pCnt$ to prN_T, where prN_T is the number of triangles associated with the problem under consideration. This attains a

†Reference [24] is erroneous

desirable stepping through and packing of only the upper triangle for all subsectional symmetric matrices within $\bar{\bar{Z}}$. Within every loop, symmetry is immediately enforced by casting the computed value to its symmetric counterpart,

$$Z_{uv}(V,U) = Z_{uv}(U,V). \tag{C.4}$$

When the source and observation triangles support different current types, e.g. magnetic ('M') and electric ('J'), symmetry is lost. Integral computations should now be performed twice for every triangle-pair. To accomplish this, an extra loop has been introduced. Its function is to re-enter the filling process after interchanging the values of p and q; the source becomes the observer and vice versa. The approach thus takes a temporary sidestep from evaluating only upper-triangular elements. Also note that when the source triangle supports an electric surface current, the computed value is packed in the lower triangle of the global matrix ($U > V$), and when the source supports a magnetic surface current the computed value is packed in the upper triangle of the matrix ($U < V$). This follows directly from the definition of the partitioned matrix, Eqn. 4.30.

When the source and observation triangles are adjacent or congruent, the factor K manipulates the calculation of the elements on, and next to the diagonal. This adjusting is required because $qCnt$ only runs from $pCnt$ to prN_T. To demonstrate this, consider Fig. C.2.

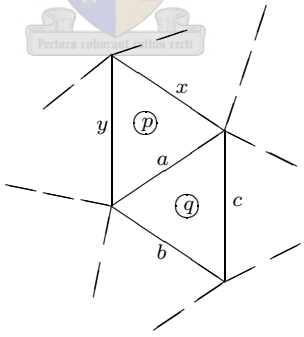

Figure C.2: Triangle pair p and q contributing to the elements of matrix $\bar{\bar{Z}}$ on, and next to, the diagonal.

The diagonal element Z_{aa} consists of the contribution of the following triangle pairs

$$Z_{aa} = I^{pp} + I^{qq} + I^{qp} + I^{pq}. \tag{C.5}$$

Since $qCnt$ only runs from $pCnt$ to prN_T, the code will compute only one of the last two terms. Since $I^{pq} = I^{qp}$ (if the test was fully Galerkin), this contribution can therefore be doubled

$$\text{if } p \neq q \text{ and } u = v, \text{ then } Z_{uv} = Z_{uv} + 2I^{pq}. \tag{C.6}$$

The other adjustment needed is seen when considering the case when the source and observer triangles are equal, $p = q$. Assume that I^{qq} will contribute to the following elements on, and next to, the diagonal. The Z-subscripts used are arbitrary, and are just used to indicate the element position in the matrix

$$I^{qq} \rightarrow \begin{bmatrix} Z_{11} & Z_{12} \\ Z_{21} & Z_{22} \end{bmatrix}. \tag{C.7}$$

The contribution of I^{qq} at Z_{21} will be incorrectly added at Z_{12}, since all contributions of I^{qq} are packed in the upper triangular matrix of $\bar{\bar{Z}}$. Remembering that $Z_{uv} = Z_{uv} + KI^{pq}$, this contribution can simply be zeroed

$$\text{if } p = q \text{ and } u > v, \text{ then } K = 0. \tag{C.8}$$

The advantage of this packing scheme is that an arbitrary number of problems may be stacked and solved simultaneously. These may support any combination of electric and magnetic surface currents. The symmetric submatrices within the global matrix are evaluated efficiently using an adapted form of the packing method introduced by [24]. This method was used as a basis because of its reduction in execution time and the amount of memory required. Simpler problems may still reduce to this form and benefit from these advantages.

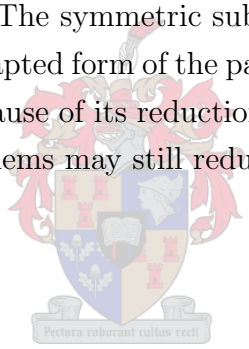

Appendix D

Integration of Singular Integrands

When the observation and source triangles are congruent, singularities arise in the numerical computation of the integrals, since the observation point can coincide with the source point. Wilton et al. [38] presented analytical expressions for the most commonly encountered potential integrals due to uniform and linearly varying source distributions defined on simply shaped domains. Two particular solutions defined on a planar surface with polygonal boundaries have been found useful in the evaluation of the self-term contributions to the moment matrix. The formulae presented have advantages in terms of accuracy, conciseness and convenience for numerical work.

To facilitate evaluation of the potential integrals, a few readily identifiable geometrical quantities are introduced (Fig. D.1). When surface sources are distributed on a planar polygon S, the potential observed at a point $\mathbf{r}$ due to an elemental source on S at $\mathbf{r}'$ is proportional to $\frac{1}{R} = \frac{1}{|\mathbf{r}-\mathbf{r}'|}$. The perpendicular distance from the point located by $\mathbf{r}$ to ∂S_i (the i^{th} edge of S) or its extension is designated P_i^0. ∂S_i is parameterised by the arc length variable l' measured from the plane which is perpendicular to the i^{th} edge and which passes through the point located by $\mathbf{r}$. P_i^0 and l' represent, in effect, a pair of rectangular coordinates in the plane P locating points on ∂S_i. In terms of l', the endpoints of ∂S_i are located at l_i^+ and l_i^-. Distances measured from $\mathbf{r}$ to the associated endpoints $\mathbf{r}_i^+$ and $\mathbf{r}_i^-$ of ∂S_i are denoted R_i^+ and R_i^- respectively. The quantities P_i^0, $\hat{\mathbf{P}}_i^0$, $R_i^\pm$ and $l_i^\pm$ are readily calculated in terms of $\mathbf{r}$ and $\mathbf{r}_i^\pm$ by the following sequence of computations

$$\begin{aligned}
&\hat{\mathbf{l}}_i = \frac{\mathbf{r}_i^+ - \mathbf{r}_i^-}{|\mathbf{r}_i^+ - \mathbf{r}_i^-|} && \hat{\mathbf{u}}_i = \hat{\mathbf{l}}_i \times \hat{\mathbf{n}} \\
&l_i^\pm = (\mathbf{r}_i^\pm - \mathbf{r}) \cdot \hat{\mathbf{l}}_i && P_i^0 = |(\mathbf{r}_i^\pm - \mathbf{r}) \cdot \hat{\mathbf{u}}_i| \\
&R_i^\pm = |\mathbf{r}_i^\pm - \mathbf{r}| = \sqrt{(P_i^0)^2 + (l_i^\pm)^2} && \hat{\mathbf{P}}_i^0 = \frac{(\mathbf{r}_i^\pm - \mathbf{r}) - l_i^\pm \hat{\mathbf{l}}_i}{P_i^0}.
\end{aligned} \tag{D.1}$$

Note that $\hat{\mathbf{u}}_i = \pm\hat{\mathbf{P}}_i^0$, the sign depending on which end of ∂S_i corresponds to the vector $\mathbf{r}_i^+$.

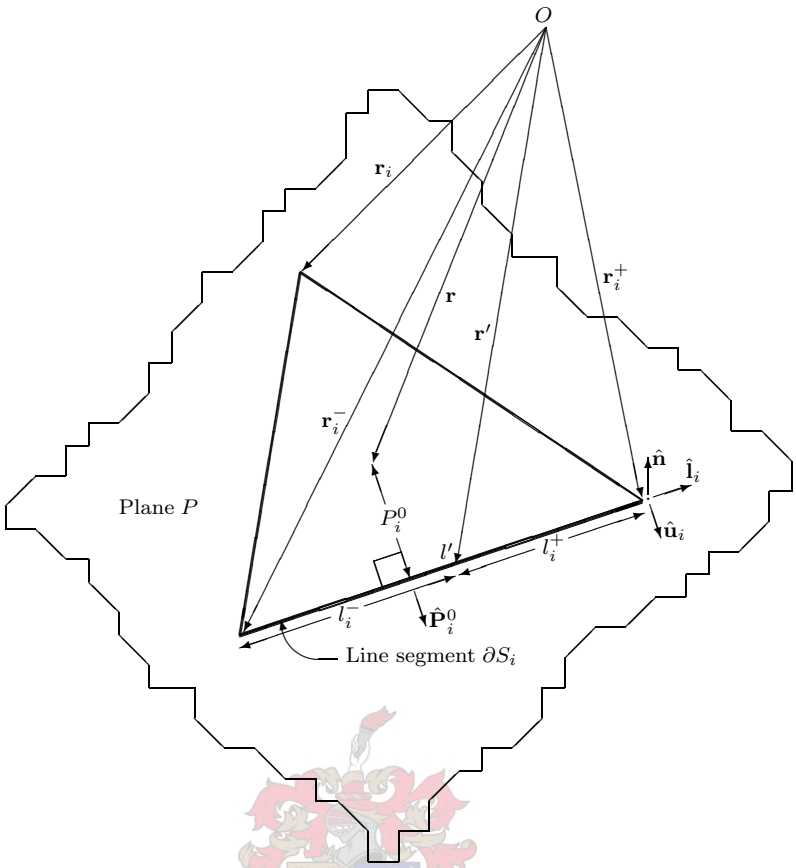

Figure D.1: Geometrical quantities associated with the line segment C lying in the plane P. The observation point for the potential is located by the position vector $\mathbf{r}$ with respect to the coordinate origin O.

Wilton [38] defines a distance d, which represents the height of the observation point above the plane of S, measured positively in the direction of the unit normal $\hat{\mathbf{n}}$. In the Method of Moments solution for the self-term, the observation point is in the plane P at the point $\mathbf{r} = \mathbf{r}^{cp}$. Setting the distance $d = 0$, the potential due to a uniform source distribution on S is proportional to

$$\int_S \frac{1}{R} dS' = \sum_i \hat{\mathbf{P}}_i^0 \cdot \hat{\mathbf{u}}_i \left[P_i^0 \ln \frac{R_i^+ + l_i^+}{R_i^- + l_i^-} \right]. \tag{D.2}$$

If $\mathbf{r}$ is on an edge or its extension, it is easily shown that the contribution to the sum in Eqn. D.2 from that edge vanishes. The form is also symmetric in the vertex indices, which not only is intuitively satisfying, but also has the practical consequence of rendering it suitable for programming using loop/vector operations when the vertex information is stored in vector form.

The corresponding integral for linearly varying source distributions is evaluated in vector

form

$$\int_S \frac{\mathbf{r}' - \mathbf{r}}{R} dS' = \frac{1}{2} \sum_i \hat{\mathbf{u}}_i \left[(P_i^0)^2 \ln \frac{R_i^+ + l_i^+}{R_i^- + l_i^-} + l_i^+ R_i^+ - l_i^- R_i^- \right]. \tag{D.3}$$

Both Eqns. D.2 and D.3 transformed a surface integral to a line integral. Of importance is to get the reference direction of integration over $\partial l'$ correct. It is known [42] that if the matrix

$$\bar{\bar{D}} = \begin{bmatrix} 1 & x_1 & y_1 \\ 1 & x_2 & y_2 \\ 1 & x_3 & y_3 \end{bmatrix} \tag{D.4}$$

is formed, the area of triangle T^q is given by the absolute value of the determinant of $\bar{\bar{D}}$

$$A^q = \frac{1}{2} |\det \bar{\bar{D}}|. \tag{D.5}$$

The sign of the determinant determines the integration direction, $Sign = \text{sign}[\det(\bar{\bar{D}})]$, with $Sign = +1$ if the integration is in an anti-clockwise direction with the unit normal vector $\hat{\mathbf{n}}$ in a positive z direction, and $Sign = -1$ if the integration is in a clockwise direction. Therefore, to get the correct direction of integration, ensure that both the sign of the normal vector and that of the determinant of the nodal coordinate matrix are the same. The direction of integration for an x and y directed triangle may be calculated using nodal coordinate matrices $[1\ y\ z]$ and $[1\ z\ x]$ respectively.

A singular term of the form $\frac{e^{-jkR}}{R}$ is present in the diagonal elements of the vector potential dyads $\bar{\bar{\mathbf{K}}}_A$ and $\bar{\bar{\mathbf{K}}}_F$; and also for the scalar potentials K_Φ and K_Ψ. To evaluate the time-harmonic scalar potential due to a uniform charge distribution on a triangular patch T^q, a subtraction-and-addition of the singularity approach is used. The scalar potential is proportional to

$$\int_{T^q} \frac{e^{-jkR}}{R} dS' = \int_{T^q} \frac{e^{-jkR} - 1}{R} dS' + \int_{T^q} \frac{1}{R} dS'. \tag{D.6}$$

The first integral on the right has a bounded integrand for every observation point and hence can be integrated numerically as was described in Section 4.5; the second integral is a special case of Eqn. D.2 and hence can be evaluated analytically.

On evaluating the diagonal elements of the vector potential dyads, the static parts multiplied with the vector basis functions pose a singularity which cannot be integrated analytically. The basis functions are proportional to the vector $\mathbf{r}' - \mathbf{r}_i$, where $\mathbf{r}_i$ is the i^{th}

vertex of T^q. Vector potentials due to these basis functions are then proportional to

$$\begin{aligned}\int_{T^q}(\mathbf{r}'-\mathbf{r}_i)\frac{e^{-jkR}}{R}dS' &= \int_{T^q}(\mathbf{r}'-\mathbf{r})\frac{e^{-jkR}}{R}dS' + (\mathbf{r}-\mathbf{r}_i)\int_{T^q}\frac{e^{-jkR}}{R}dS' \\ &= \int_{T^q}(\mathbf{r}'-\mathbf{r}^{cp})\frac{e^{-jkR}-1}{R}dS' + (\mathbf{r}^{cp}-\mathbf{r}_i)\int_{T^q}\frac{e^{-jkR}-1}{R}dS' \\ &\quad + \int_{T^q}\frac{\mathbf{r}'-\mathbf{r}^{cp}}{R}dS' + (\mathbf{r}^{cp}-\mathbf{r}_i)\int_{T^q}\frac{1}{R}dS'.\end{aligned} \tag{D.7}$$

The last two integrals are merely Eqns. D.2 and D.3 with S specialised to T^q, and the two preceding ones always have bounded integrands which can be numerically integrated. In the last step, the position vector $\mathbf{r}$ has been replaced with the centroid $\mathbf{r}^{cp}$ of the observation triangle.

For the non-diagonal elements of $\bar{\bar{\mathbf{K}}}_A$ and $\bar{\bar{\mathbf{K}}}_F$ the singularity is of the form

$$\frac{e^{-jks}}{\rho} - \frac{s}{\rho r}e^{-jkr}. \tag{D.8}$$

Treatment of the singularity is described by Bunger and Arndt [31]

> For the non-diagonal elements of $\bar{\bar{\mathbf{K}}}_A$, the analytical expressions of the extracted static parts are singular only at the interfaces between the adjacent layers. Since the terms of the static parts multiplied with the basis functions cannot be integrated analytically, the static parts are simply added to the non-diagonal regular parts of $\bar{\bar{\mathbf{K}}}_A$ in the space domain, and integrated numerically. The singularity of the total non-diagonal elements of $\bar{\bar{\mathbf{K}}}_A$ poses no numerical difficulties, because the triangular segments are not allowed to cross the interface between adjacent layers. The treatment of the singularities in layered media is similar to the treatment of singularities in free-space, the only difference is the appearance of additional image terms.

Correctness of the above statement needed verification because substituting $\rho = 0$ lead to a mathematically undefined result. A Taylor expansion of Eqn. D.8 was developed to avoid the possibility of a singularity at $\rho = 0$

$$\frac{e^{-jks}}{\rho} - \frac{s}{\rho r}e^{-jkr} \approx \frac{e^{-jkr}}{r}[\frac{1}{2}(1+K)\gamma + \frac{1}{24}(1+2K+3K^2)\gamma^3]. \tag{D.9}$$

In the last equation $K = jkr$ and γ can be defined as the angle between the vertical distance s and the spatial distance r separating the source and observer points. As γ approaches zero, $\rho \to 0$ and Eqn. D.8 indeed has an analytical solution for all values of ρ.

Appendix E

Magnetic Dipole Fields in a Layered Medium

Similar to the problem of an electric dipole embedded in a layered medium (Chapter 2 Section 2.3), the TM and TE wave components of a magnetic dipole propagate through a layered medium completely decoupled from each other.

Expressions defining the field equations for a magnetic dipole (Eqn. 2.31) are repeated for convenience

$$\begin{aligned}\mathbf{E}(\mathbf{r}) &= -j\omega\mu\nabla\times\hat{\boldsymbol{\alpha}}IA\frac{e^{-jkr}}{4\pi r}\\ \mathbf{H}(\mathbf{r}) &= k^2\Big(\bar{\bar{\mathbf{I}}}+\frac{\nabla\nabla}{k^2}\Big)\cdot\hat{\boldsymbol{\alpha}}IA\frac{e^{-jkr}}{4\pi r}.\end{aligned} \tag{E.1}$$

For a horizontal magnetic dipole (HMD) located in medium m and pointing in the x direction, the respective Green's functions for the normal field component wave propagation in medium n are

$$\begin{aligned}G^{zx}_{EM,n} &= -j\omega\mu_m\frac{IA}{4\pi}\sin\phi\int_0^\infty J_1(k_\rho\rho)\frac{k_\rho^2}{jk_{mz}}F^{HMD}_{E_z}\frac{\epsilon_m}{\epsilon_n}dk_\rho\\ G^{zx}_{HM,n} &= -\frac{IA}{4\pi}\cos\phi\int_0^\infty J_1(k_\rho\rho)k_\rho^2F^{HMD}_{H_z}\frac{\mu_m}{\mu_n}dk_\rho.\end{aligned} \tag{E.2}$$

A vertical magnetic dipole (VMD) located in medium m has a zero E_z component, therefore no TM wave. Using Eqn. E.1, the Green's function expansion of the normal field component for TE wave propagation in medium n is

$$G^{zz}_{HM,n} = \frac{IA}{4\pi}\int_0^\infty J_0(k_\rho\rho)\frac{k_\rho^3}{jk_{mz}}F^{VMD}_{H_z}\frac{\mu_m}{\mu_n}dk_\rho. \tag{E.3}$$

The functions $F^{HMD}_{E_z}$, $F^{HMD}_{H_z}$ and $F^{VMD}_{H_z}$ are the z-dependent solutions of wave propagation for a magnetic dipole source in a stratified medium. These functions depend on the position of the observation layer relative to the source layer.

Observation point and source in the same layer, $n = m$

Inside the m^{th} layer the z variation of the solutions for a horizontal magnetic dipole and vertical magnetic dipole are

$$\begin{aligned} F_{E_z}^{HMD} &= e^{-jk_{mz}|z-z'|} + B_m^{TM,HMD} e^{jk_{mz}z} + D_m^{TM,HMD} e^{-jk_{mz}z} \\ F_{H_z}^{HMD} &= \mp e^{-jk_{mz}|z-z'|} + B_m^{TE,HMD} e^{jk_{mz}z} + D_m^{TE,HMD} e^{-jk_{mz}z} \\ F_{H_z}^{VMD} &= e^{-jk_{mz}|z-z'|} + B_m^{TE,VMD} e^{jk_{mz}z} + D_m^{TE,VMD} e^{-jk_{mz}z} \end{aligned} \tag{E.4}$$

where the amplitude coefficients are found from constraint conditions for the waves at $z = -d_{m-1}$ and $z = -d_m$

$$\begin{aligned} B_m^{TM,HMD} &= \tilde{R}_{m,m-1}^{TM}\left[+e^{-jk_{mz}|d_{m-1}+z'|} + e^{-jk_{mz}(d_m-d_{m-1})}\tilde{R}_{m,m+1}^{TM}e^{-jk_{mz}|d_m+z'|}\right]\tilde{M}_m^{TM}e^{jk_{mz}d_{m-1}} \\ D_m^{TM,HMD} &= \tilde{R}_{m,m+1}^{TM}\left[+e^{-jk_{mz}|d_m+z'|} + e^{-jk_{mz}(d_m-d_{m-1})}\tilde{R}_{m,m-1}^{TM}e^{-jk_{mz}|d_{m-1}+z'|}\right]\tilde{M}_m^{TM}e^{-jk_{mz}d_m} \\ B_m^{TE,HMD} &= \tilde{R}_{m,m-1}^{TE}\left[-e^{-jk_{mz}|d_{m-1}+z'|} + e^{-jk_{mz}(d_m-d_{m-1})}\tilde{R}_{m,m+1}^{TE}e^{-jk_{mz}|d_m+z'|}\right]\tilde{M}_m^{TE}e^{jk_{mz}d_{m-1}} \\ D_m^{TE,HMD} &= \tilde{R}_{m,m+1}^{TE}\left[+e^{-jk_{mz}|d_m+z'|} - e^{-jk_{mz}(d_m-d_{m-1})}\tilde{R}_{m,m-1}^{TE}e^{-jk_{mz}|d_{m-1}+z'|}\right]\tilde{M}_m^{TE}e^{-jk_{mz}d_m} \\ B_m^{TE,VMD} &= \tilde{R}_{m,m-1}^{TE}\left[+e^{-jk_{mz}|d_{m-1}+z'|} + e^{-jk_{mz}(d_m-d_{m-1})}\tilde{R}_{m,m+1}^{TE}e^{-jk_{mz}|d_m+z'|}\right]\tilde{M}_m^{TE}e^{jk_{mz}d_{m-1}} \\ D_m^{TE,VMD} &= \tilde{R}_{m,m+1}^{TE}\left[+e^{-jk_{mz}|d_m+z'|} + e^{-jk_{mz}(d_m-d_{m-1})}\tilde{R}_{m,m-1}^{TE}e^{-jk_{mz}|d_{m-1}+z'|}\right]\tilde{M}_m^{TE}e^{-jk_{mz}d_m}. \end{aligned} \tag{E.5}$$

The values of $\tilde{M}_m^{TM}$ and $\tilde{M}_m^{TE}$ were defined in Section 2.3. Conveniently, both sources use the same value. Similarly, the generalised reflection coefficients were derived for an electric dipole source and is given by Eqns. 2.19 to 2.21.

Observation point in layer $n < m$

Using a recursive method similar to that described for an electric dipole, the z-dependence of the field in Region n can be written as

$$\begin{aligned} F_{E_z}^{HMD} &= A_n^{TM,HMD+}\left[e^{-jk_{nz}z} + \tilde{R}_{n,n-1}^{TM}e^{2jk_{nz}d_{n-1}+jk_{nz}z}\right] \\ F_{H_z}^{HMD} &= A_n^{TE,HMD+}\left[e^{-jk_{nz}z} + \tilde{R}_{n,n-1}^{TE}e^{2jk_{nz}d_{n-1}+jk_{nz}z}\right] \\ F_{H_z}^{VMD} &= A_n^{TE,VMD+}\left[e^{-jk_{nz}z} + \tilde{R}_{n,n-1}^{TE}e^{2jk_{nz}d_{n-1}+jk_{nz}z}\right], \end{aligned} \tag{E.6}$$

with A_n^+ the amplitude of the upgoing wave, given by

$$A_n^+ e^{jk_{nz}d_n} = A_m^+ e^{jk_{mz}d_m}\prod_{i=n}^{m-1}\left(e^{-jk_{i+1,z}(d_{i+1}-d_i)}S_{i+1,i}^+\right) \tag{E.7}$$

and

$$S^{+}_{i+1,i} = \frac{T_{i+1,i}}{1 - R_{i,i+1}\tilde{R}_{i,i-1}e^{-2jk_{iz}(d_i - d_{i-1})}}. \tag{E.8}$$

To calculate the amplitude of the upgoing wave in the source layer A^{+}_{m}, use the same procedure as was explained for an electric dipole (Section 2.3)

$$\begin{aligned}
A^{TM,HMD+}_{m} &= \left[+e^{jk_{mz}z'} + e^{-jk_{mz}(2d_m + z')}\tilde{R}^{TM}_{m,m+1}\right]\tilde{M}^{TM}_{m} \\
A^{TE,HMD+}_{m} &= \left[-e^{jk_{mz}z'} + e^{-jk_{mz}(2d_m + z')}\tilde{R}^{TE}_{m,m+1}\right]\tilde{M}^{TE}_{m} \\
A^{TE,VMD+}_{m} &= \left[+e^{jk_{mz}z'} + e^{-jk_{mz}(2d_m + z')}\tilde{R}^{TE}_{m,m+1}\right]\tilde{M}^{TE}_{m}.
\end{aligned} \tag{E.9}$$

Observation point in layer $n > m$

To find the z-dependence of the field in Region n, with $n > m$, recursive relations similar to Eqns. 2.26 to 2.29 for an electric dipole source are used. The results are

$$\begin{aligned}
F^{HMD}_{E_z} &= A^{TM,HMD-}_{n}\left[e^{jk_{nz}z} + \tilde{R}^{TM}_{n,n+1}e^{-2jk_{nz}d_n - jk_{nz}z}\right] \\
F^{HMD}_{H_z} &= A^{TE,HMD-}_{n}\left[e^{jk_{nz}z} + \tilde{R}^{TE}_{n,n+1}e^{-2jk_{nz}d_n - jk_{nz}z}\right] \\
F^{VMD}_{H_z} &= A^{TE,VMD-}_{n}\left[e^{jk_{nz}z} + \tilde{R}^{TE}_{n,n+1}e^{-2jk_{nz}d_n - jk_{nz}z}\right]
\end{aligned} \tag{E.10}$$

where the amplitude of the downgoing wave A^{-}_{n} is related to the amplitude of the downgoing wave in the source layer A^{-}_{m}. The relation is given by

$$A^{-}_{n}e^{-jk_{nz}d_{n-1}} = A^{-}_{m}e^{-jk_{mz}d_{m-1}}\prod_{i=m}^{n-1}\left(e^{-jk_{iz}(d_i - d_{i-1})}S^{-}_{i,i+1}\right) \tag{E.11}$$

with

$$S^{-}_{i,i+1} = \frac{T_{i,i+1}}{1 - R_{i+1,i}\tilde{R}_{i+1,i+2}e^{-2jk_{i+1,z}(d_{i+1} - d_i)}}. \tag{E.12}$$

and

$$\begin{aligned}
A^{TM,HMD-}_{m} &= \left[+e^{-jk_{mz}z'} + e^{jk_{mz}(2d_{m-1} + z')}\tilde{R}^{TM}_{m,m-1}\right]\tilde{M}^{TM}_{m} \\
A^{TE,HMD-}_{m} &= \left[+e^{-jk_{mz}z'} - e^{jk_{mz}(2d_{m-1} + z')}\tilde{R}^{TE}_{m,m-1}\right]\tilde{M}^{TE}_{m} \\
A^{TE,VMD-}_{m} &= \left[+e^{-jk_{mz}z'} + e^{jk_{mz}(2d_{m-1} + z')}\tilde{R}^{TE}_{m,m-1}\right]\tilde{M}^{TE}_{m}.
\end{aligned} \tag{E.13}$$

Appendix F

Electric Potential Green's Functions

To find the electric vector and magnetic scalar potential Green's functions, the principle of duality can be effectively utilised. In addition to Eqn. 2.30, the duality replacements for the vector potentials are

$$\mathbf{A} \rightarrow \mathbf{F} \quad \text{and} \quad \mathbf{F} \rightarrow -\mathbf{A}. \tag{F.1}$$

The dyadic for the electric vector potential $\bar{\bar{\mathbf{K}}}_F$ is given by

$$\bar{\bar{\mathbf{K}}}_F = \begin{bmatrix} G_F^{xx} & 0 & K_F^{xz} \\ 0 & G_F^{xx} & K_F^{yz} \\ G_F^{zx} & G_F^{zy} & K_F^{zz} \end{bmatrix}. \tag{F.2}$$

As was explained for the magnetic potentials, evaluation of G_F^{xx}, G_F^{zx}, K_F^{xz} and K_F^{zz} is sufficient for a complete description of the dyadic kernel. In addition the Green's function for the scalar potential associated with a horizontal magnetic dipole G_Ψ should be computed.

With $F_{E_z}^{HMD}$, $F_{H_z}^{HMD}$ and $F_{H_z}^{VMD}$ given by either Eqn. E.6 or E.10, the spatial domain Green's functions for the electric potentials are

$$\begin{aligned}
G_\Psi &= \frac{j\omega\mu_m IA}{4\pi\mu_n}\int_0^\infty J_0(k_\rho\rho)\Big(\frac{1}{k_\rho}\frac{\partial}{\partial z}F_{H_z}^{HMD} + \frac{k_n^2}{jk_{mz}k_\rho}F_{E_z}^{HMD}\frac{\epsilon_m}{\epsilon_n}\Big)dk_\rho \\
G_F^{xx} &= \frac{j\omega\mu_m\epsilon_n IA}{4\pi}\int_0^\infty J_0(k_\rho\rho)\frac{k_\rho}{jk_{mz}}F_{E_z}^{HMD}\frac{\epsilon_m}{\epsilon_n}dk_\rho \\
G_F^{zx} &= \frac{j\omega\mu_m\epsilon_n IA}{4\pi}\cos\phi\int_0^\infty J_1(k_\rho\rho)\Big(-F_{H_z}^{HMD} + \frac{1}{jk_{mz}}\frac{\partial}{\partial z}F_{E_z}^{HMD}\frac{\epsilon_m}{\epsilon_n}\Big)dk_\rho \\
K_F^{xz} &= \frac{j\omega\mu_m\epsilon_n IA}{4\pi}\cos\phi\int_0^\infty J_1(k_\rho\rho)\frac{j}{k_{mz}}\Big(\frac{k_m^2}{k_n^2}\frac{\partial}{\partial z}F_{H_z}^{VMD} + \frac{\partial}{\partial z'}F_{E_z}^{HMD}\frac{\epsilon_m}{\epsilon_n}\Big)dk_\rho \\
K_F^{zz} &= -\frac{j\omega\mu_m\epsilon_n IA}{4\pi}\int_0^\infty J_0(k_\rho\rho)\Big[j\Big(\frac{k_\rho}{k_{mz}}\frac{k_m^2}{k_n^2} - \frac{k_{mz}}{k_\rho}\Big)F_{H_z}^{VMD} + \frac{j}{k_{mz}k_\rho}\frac{\partial^2}{\partial z'\partial z}F_{E_z}^{HMD}\frac{\epsilon_m}{\epsilon_n}\Big]dk_\rho.
\end{aligned} \tag{F.3}$$

In the above equations the source and observation points are separated by at least one layer, $|n-m| > 1$, and asymptotic techniques cannot be used to increase convergence of the Sommerfeld integrals.

When the source and observation points are in adjacent layers, $|n-m| = 1$, the largest asymptotic term is extracted to improve convergence. In this case there are no image terms and the static part corresponds to the direct transmitted wave, which was graphically explained in Fig. 3.4. The associated transmission coefficients are

$$\begin{aligned} T_M^{TM,\infty} &= \frac{2\epsilon_m}{\epsilon_n + \epsilon_m} \\ T_M^{TE,\infty} &= \frac{2\mu_n}{\mu_n + \mu_m} \end{aligned} \tag{F.4}$$

and the "averaged" propagation constant used for an equivalent homogeneous medium (Section 3.3) is

$$k_i = 0.5[\Re(k_m) + \Re(k_n)] + j \min[\Im(k_m), \Im(k_n)]. \tag{F.5}$$

When the source and observation points are located in the same layer, $m = n$, the first three largest asymptotic terms are extracted in the spectral domain. In the space domain, these terms represent the direct part, and two images at the upper and lower interfaces. This was shown in Fig. 3.5. The reflection coefficients have the same values as those used for the magnetic potentials

$$\begin{aligned} R_{m,m-1}^{TE,\infty} &= \frac{\mu_{m-1} - \mu_m}{\mu_{m-1} + \mu_m} \qquad R_{m,m+1}^{TE,\infty} = \frac{\mu_{m+1} - \mu_m}{\mu_{m+1} + \mu_m} \\ R_{m,m-1}^{TM,\infty} &= \frac{\epsilon_{m-1} - \epsilon_m}{\epsilon_{m-1} + \epsilon_m} \qquad R_{m,m+1}^{TM,\infty} = \frac{\epsilon_{m+1} - \epsilon_m}{\epsilon_{m+1} + \epsilon_m} \end{aligned} . \tag{F.6}$$

Finally, $F_{E_z}^{HMD}$, $F_{H_z}^{HMD}$ and $F_{H_z}^{VMD}$ are given by either Eqn. E.4 (without the direct terms), Eqn. E.6 or Eqn. E.10. The particular choice depends on the respective source and observation layers.

Evaluation of G_Ψ

Observation point and source in adjacent layers, $|n-m| = 1$

$$\begin{aligned} G_\Psi = \frac{j\omega\mu_m IA}{4\pi\mu_n} \Bigg[T_M^{TE,\infty} \frac{e^{-jk_i r}}{r} + \int_0^\infty J_0(k_\rho \rho) \Big(\frac{1}{k_\rho} \frac{\partial}{\partial z} F_{H_z}^{HMD} \\ + \frac{k_n^2}{j k_{mz} k_\rho} F_{E_z}^{HMD} \frac{\epsilon_m}{\epsilon_n} - T_M^{TE,\infty} e^{-jk_{iz}|z-z'|} \frac{k_\rho}{jk_{iz}} \Big) dk_\rho \Bigg] \end{aligned} \tag{F.7}$$

Observation point and source in the same layer, $n = m$

$$G_\Psi = \frac{j\omega IA}{4\pi}\Bigg[\frac{e^{-jk_m r}}{r} - R^{TE,\infty}_{m,m-1}\frac{e^{-jk_m r_1}}{r_1} - R^{TE,\infty}_{m,m+1}\frac{e^{-jk_m r_2}}{r_2} + \int_0^\infty J_0(k_\rho\rho)\Big(\frac{1}{k_\rho}\frac{\partial}{\partial z}F^{HMD}_{H_z} + \frac{k_m^2}{jk_{mz}k_\rho}F^{HMD}_{E_z} + R^{TE,\infty}_{m,m-1}e^{-jk_{mz}s_1}\frac{k_\rho}{jk_{mz}} + R^{TE,\infty}_{m,m+1}e^{-jk_{mz}s_2}\frac{k_\rho}{jk_{mz}}\Big)dk_\rho\Bigg] \tag{F.8}$$

Evaluation of G^{xx}_F

Observation point and source in adjacent layers, $|n - m| = 1$

$$G^{xx}_F = \frac{j\omega\mu_m\epsilon_n IA}{4\pi}\Bigg[T^{TM,\infty}_M\frac{e^{-jk_i r}}{r} + \int_0^\infty J_0(k_\rho\rho)k_\rho\Big(\frac{F^{HMD}_{E_z}}{jk_{mz}}\frac{\epsilon_m}{\epsilon_n} - \frac{T^{TM,\infty}_M}{jk_{iz}}e^{-jk_{iz}|z-z'|}\Big)dk_\rho\Bigg] \tag{F.9}$$

Observation point and source in the same layer, $n = m$

$$G^{xx}_F = \frac{j\omega\mu_m\epsilon_m IA}{4\pi}\Bigg[\frac{e^{-jk_m r}}{r} + R^{TM,\infty}_{m,m-1}\frac{e^{-jk_m r_1}}{r_1} + R^{TM,\infty}_{m,m+1}\frac{e^{-jk_m r_2}}{r_2} + \int_0^\infty J_0(k_\rho\rho)\frac{k_\rho}{jk_{mz}}\Big(F^{HMD}_{E_z} - R^{TM,\infty}_{m,m-1}e^{-jk_{mz}s_1} - R^{TM,\infty}_{m,m+1}e^{-jk_{mz}s_2}\Big)dk_\rho\Bigg] \tag{F.10}$$

Evaluation of G^{zx}_F

Observation point and source in adjacent layers, $|n - m| = 1$

$$G^{zx}_F = \frac{j\omega\mu_m\epsilon_n IA}{4\pi}\cos\phi\Bigg[-\text{sign}(z-z')(T^{TM,\infty}_M - T^{TE,\infty}_M)\Big(\frac{1}{\rho}e^{-jk_i|z-z'|} - \frac{|z-z'|}{\rho r}e^{-jk_i r}\Big) + \int_0^\infty J_1(k_\rho\rho)\Big(-F^{HMD}_{H_z} + \frac{1}{jk_{mz}}\frac{\partial}{\partial z}F^{HMD}_{E_z}\frac{\epsilon_m}{\epsilon_n} + \text{sign}(z-z')(T^{TM,\infty}_M - T^{TE,\infty}_M)e^{-jk_{iz}|z-z'|}\Big)dk_\rho\Bigg] \tag{F.11}$$

Observation point and source in the same layer, $n = m$

$$G^{zx}_F = \frac{j\omega\mu_m\epsilon_m IA}{4\pi}\cos\phi\Bigg[(R^{TE,\infty}_{m,m-1} + R^{TM,\infty}_{m,m-1})\Big(\frac{1}{\rho}e^{-jk_m s_1} - \frac{s_1}{\rho r_1}e^{-jk_m r_1}\Big) - (R^{TE,\infty}_{m,m+1} + R^{TM,\infty}_{m,m+1})\Big(\frac{1}{\rho}e^{-jk_m s_2} - \frac{s_2}{\rho r_2}e^{-jk_m r_2}\Big) + \int_0^\infty J_1(k_\rho\rho)\Big(-F^{HMD}_{H_z} + \frac{1}{jk_{mz}}\frac{\partial}{\partial z}F^{HMD}_{E_z} - (R^{TE,\infty}_{m,m-1} + R^{TM,\infty}_{m,m-1})e^{-jk_{mz}s_1} + (R^{TE,\infty}_{m,m+1} + R^{TM,\infty}_{m,m+1})e^{-jk_{mz}s_2}\Big)dk_\rho\Bigg] \tag{F.12}$$

Evaluation of K_F^{xz}

Observation point and source in adjacent layers, $|n-m|=1$

$$\begin{aligned}K_F^{xz} = \frac{j\omega\mu_m\epsilon_n IA}{4\pi}\cos\phi\Bigg[&-\text{sign}(z-z')(T_M^{TM,\infty} - \frac{k_m^2}{k_n^2}T_M^{TE,\infty})\Big(\frac{1}{\rho}e^{-jk_i|z-z'|} - \frac{|z-z'|}{\rho r}e^{-jk_i r}\Big)\\ &+ \int_0^\infty J_1(k_\rho\rho)\Big(\frac{j}{k_{mz}}\frac{k_m^2}{k_n^2}\frac{\partial}{\partial z}F_{H_z}^{VMD} + \frac{j}{k_{mz}}\frac{\partial}{\partial z'}F_{E_z}^{HMD}\frac{\epsilon_m}{\epsilon_n}\\ &+ \text{sign}(z-z')(T_M^{TM,\infty} - \frac{k_m^2}{k_n^2}T_M^{TE,\infty})e^{-jk_{iz}|z-z'|}\Big)dk_\rho\Bigg]\end{aligned} \tag{F.13}$$

Observation point and source in the same layer, $n=m$

$$\begin{aligned}K_F^{xz} = \frac{j\omega\mu_m\epsilon_m IA}{4\pi}\cos\phi\Bigg[&-(R_{m,m-1}^{TE,\infty} + R_{m,m-1}^{TM,\infty})\Big(\frac{1}{\rho}e^{-jk_m s_1} - \frac{s_1}{\rho r_1}e^{-jk_m r_1}\Big)\\ &+ (R_{m,m+1}^{TE,\infty} + R_{m,m+1}^{TM,\infty})\Big(\frac{1}{\rho}e^{-jk_m s_2} - \frac{s_2}{\rho r_2}e^{-jk_m r_2}\Big)\\ &+ \int_0^\infty J_1(k_\rho\rho)\Big(\frac{j}{k_{mz}}\frac{\partial}{\partial z}F_{H_z}^{VMD} + \frac{j}{k_{mz}}\frac{\partial}{\partial z'}F_{E_z}^{HMD}\\ &+ (R_{m,m-1}^{TE,\infty} + R_{m,m-1}^{TM,\infty})e^{-jk_{mz}s_1} - (R_{m,m+1}^{TE,\infty} + R_{m,m+1}^{TM,\infty})e^{-jk_{mz}s_2}\Big)dk_\rho\Bigg]\end{aligned} \tag{F.14}$$

Evaluation of K_F^{zz}

Observation point and source in adjacent layers, $|n-m|=1$

$$\begin{aligned}K_F^{zz} = \frac{j\omega\mu_m\epsilon_n IA}{4\pi}\Bigg[&-\Big(T_M^{TM,\infty} - (\frac{k_m^2}{k_n^2}+1)T_M^{TE,\infty}\Big)\frac{e^{-jk_i r}}{r}\\ &- \int_0^\infty J_0(k_\rho\rho)\Big[j\Big(\frac{k_\rho}{k_{mz}}\frac{k_m^2}{k_n^2} - \frac{k_{mz}}{k_\rho}\Big)F_{H_z}^{VMD} + \frac{j}{k_{mz}k_\rho}\frac{\partial^2}{\partial z'\partial z}F_{E_z}^{HMD}\frac{\epsilon_m}{\epsilon_n}\\ &+ \Big(T_M^{TM,\infty} - (\frac{k_m^2}{k_n^2}+1)T_M^{TE,\infty}\Big)e^{-jk_{iz}|z-z'|}\frac{jk_\rho}{k_{iz}}\Big]dk_\rho\Bigg]\end{aligned} \tag{F.15}$$

Observation point and source in the same layer, $n = m$

$$
\begin{aligned}
K_F^{zz} = \frac{j\omega\mu_m\epsilon_m IA}{4\pi}\Bigg[&\frac{e^{-jk_m r}}{r} + \Big(R_{m,m-1}^{TM,\infty} + 2R_{m,m-1}^{TE,\infty}\Big)\frac{e^{-jk_m r_1}}{r_1} \\
&+ \Big(R_{m,m+1}^{TM,\infty} + 2R_{m,m+1}^{TE,\infty}\Big)\frac{e^{-jk_m r_2}}{r_2} \\
&- \int_0^\infty J_0(k_\rho\rho)\Big[j\Big(\frac{k_\rho}{k_{mz}} - \frac{k_{mz}}{k_\rho}\Big)F_{H_z}^{VMD} + \frac{j}{k_{mz}k_\rho}\frac{\partial^2}{\partial z'\partial z}F_{E_z}^{HMD} \\
&- \Big(R_{m,m-1}^{TM,\infty} + 2R_{m,m-1}^{TE,\infty}\Big)e^{-jk_{mz}s_1}\frac{jk_\rho}{k_{mz}} \\
&- \Big(R_{m,m+1}^{TM,\infty} + 2R_{m,m+1}^{TE,\infty}\Big)e^{-jk_{mz}s_2}\frac{jk_\rho}{k_{mz}}\Big]dk_\rho\Bigg]
\end{aligned}
\tag{F.16}
$$

Appendix G

Total Field Green's Functions

In this Appendix the Green's functions in the frequency domain, for the total electric and magnetic fields are developed. A time-varying electric dipole embedded in stratified media is used to give a detailed analysis on the concepts involved. The derivation elaborates on the work of Van Tonder [24] and [25], with the functions in a suitable form to be used with the triangular method of moments. The Green's functions of the dual magnetic dipole are summarised and included for completeness.

The total field observed at the point (ρ, z), due to a source located at $(0, z')$, can be expressed as the sum of the direct and reflected fields

$$\begin{aligned} \mathbf{E} &= \mathbf{E}^D + \mathbf{E}^R \\ \mathbf{H} &= \mathbf{H}^D + \mathbf{H}^R. \end{aligned} \tag{G.1}$$

When the observation point and the source are in the same layer, $n = m$, the direct field corresponds to the field in a homogeneous, isotropic medium due to a point current source directed in the $\hat{\boldsymbol{\alpha}}$ direction, $\mathbf{J}(\mathbf{r}) = \hat{\boldsymbol{\alpha}} I\ell\delta(\mathbf{r})$. Expressions defining such direct fields were derived in Section 2.2, and Eqns. 2.9 and 2.10 are repeated for convenience

$$\begin{aligned} \mathbf{E}^D &= -j\omega\mu\Big(\bar{\bar{\mathbf{I}}} + \frac{\nabla\nabla}{k^2}\Big) \cdot \hat{\boldsymbol{\alpha}} I\ell \frac{e^{-jkr}}{4\pi r} \\ \mathbf{H}^D &= \nabla \times \hat{\boldsymbol{\alpha}} I\ell \frac{e^{-jkr}}{4\pi r}. \end{aligned} \tag{G.2}$$

When the observation point and source are in different layers, however, all direct fields are zero and the total field is a function of the reflected fields only.

Given the two normal components E_z and H_z, the four transverse components of the electromagnetic field can be derived in each of the homogeneous layers. Using Maxwell's

equations for a source-free region and the Fourier transform pair given by

$$\begin{aligned}\tilde{f}(k_x,k_y,z) &= \frac{1}{2\pi}\int_{-\infty}^{\infty}\int_{-\infty}^{\infty} f(x,y,z)e^{-jk_x x - jk_y y}dxdy \\ f(x,y,z) &= \frac{1}{2\pi}\int_{-\infty}^{\infty}\int_{-\infty}^{\infty} \tilde{f}(k_x,k_y,z)e^{jk_x x + jk_y y}dk_x dk_y,\end{aligned} \tag{G.3}$$

the transverse components in the spectral domain are given by [52]

$$\begin{aligned}k_\rho^2\tilde{E}_x &= jk_x\dot{\tilde{E}}_z + \omega\mu k_y\tilde{H}_z \\ k_\rho^2\tilde{E}_y &= jk_y\dot{\tilde{E}}_z - \omega\mu k_x\tilde{H}_z \\ k_\rho^2\tilde{H}_x &= jk_x\dot{\tilde{H}}_z - \omega\epsilon k_y\tilde{E}_z \\ k_\rho^2\tilde{H}_y &= jk_y\dot{\tilde{H}}_z + \omega\epsilon k_x\tilde{E}_z.\end{aligned} \tag{G.4}$$

Here the tilde ($\tilde{}$) denotes a spectral quantity, and $\dot{\psi} = \frac{\partial\psi}{\partial z}$ where ψ represents either $\tilde{E}_z$ or $\tilde{H}_z$ in Eqn. G.4.

G.1 Green's Functions for the Fields of an HED

Consider Eqn. 2.14 expressing the Green's functions of the normal TM and TE field components for an HED. Depending on the respective observation and source layers, $F_{E_z}^{HED}$ and $F_{H_z}^{HED}$ are given by either Eqn. 2.16, 2.22 or 2.26.

With the observation point and the source in the same layer, $m = n$, it was realised that the total field comprises both a direct and reflected field component. From Eqn. 2.16, the first term may be recognised to represent the direct wave, whilst the second and third terms give rise to a reflected wave.

From Eqn. 2.14 and using Eqn. G.2, the Green's functions for the direct fields can be written in closed form. The z components of the direct field created by an x directed Hertzian dipole are

$$\begin{aligned}G_{EJ,m}^{zx\,D} &= \frac{I\ell}{4\pi}\frac{j}{\omega\epsilon_m}\cos\phi\int_0^{\infty} J_1(k_\rho\rho)k_\rho^2\Big(\mp e^{-jk_{mz}|z-z'|}\Big)dk_\rho \\ &= -\frac{I\ell}{4\pi}\frac{j}{\omega\epsilon_m}\frac{\partial^2}{\partial z\partial x}\frac{e^{-jk_m r}}{r} \\ &= \cos\phi\frac{I\ell}{4\pi}e^{-jk_m r}\Big(\frac{j\omega\mu_m}{r} + \frac{3\eta_m}{r^2} + \frac{3}{j\omega\epsilon_m r^3}\Big)\sin\theta\cos\theta\end{aligned} \tag{G.5}$$

and

$$\begin{aligned} G^{zx\,D}_{HJ,m} &= \frac{I\ell}{4\pi}\sin\phi\int_0^\infty J_1(k_\rho\rho)\frac{k_\rho^2}{jk_{mz}}e^{-jk_{mz}|z-z'|}dk_\rho \\ &= -\frac{I\ell}{4\pi}\frac{\partial}{\partial y}\frac{e^{-jk_m r}}{r} \\ &= \sin\phi\frac{I\ell}{4\pi}e^{-jk_m r}\Big(\frac{jk_m}{r}+\frac{1}{r^2}\Big)\sin\theta. \end{aligned} \tag{G.6}$$

In the above two equations it was assumed that both the observation and source points are in the same layer, $m = n$. Also, for the x directed source, $\hat{\boldsymbol{\alpha}} = \hat{\mathbf{x}}$ was used; and lastly, in carrying out the Cartesian coordinate differentiation, the relations $r = \sqrt{x^2+y^2+z^2}$, $x = r\sin\theta\cos\phi$, $y = r\sin\theta\sin\phi$ and $z = r\cos\theta$ hold.

With the second and third terms in Eqn. 2.16 corresponding to the reflected wave, the total TM and TE fields are

$$\begin{aligned} G^{zx}_{EJ,m} &= G^{zx\,D}_{EJ,m} + G^{zx\,R}_{EJ,m} \\ &= G^{zx\,D}_{EJ,m} + \frac{I\ell}{4\pi}\frac{j}{\omega\epsilon_m}\cos\phi\int_0^\infty J_1(k_\rho\rho)k_\rho^2\Big(B_m^{TM,HED}e^{jk_{mz}z} + D_m^{TM,HED}e^{-jk_{mz}z}\Big)dk_\rho \\ &= \cos\phi\,(C_J^D + C_J^R) \\ &= \cos\phi\,C_J \end{aligned} \tag{G.7}$$

and

$$\begin{aligned} G^{zx}_{HJ,m} &= G^{zx\,D}_{HJ,m} + G^{zx\,R}_{HJ,m} \\ &= G^{zx\,D}_{HJ,m} + \frac{I\ell}{4\pi}\sin\phi\int_0^\infty J_1(k_\rho\rho)\frac{k_\rho^2}{jk_{mz}}\Big(B_m^{TE,HED}e^{jk_{mz}z} + D_m^{TE,HED}e^{-jk_{mz}z}\Big)dk_\rho \\ &= \sin\phi\,(F_J^D + F_J^R) \\ &= \sin\phi\,F_J. \end{aligned} \tag{G.8}$$

When the observation point and the source are in different layers, i.e. $m \neq n$, all direct fields are zero, and $F^{HED}_{E_z}$ and $F^{HED}_{H_z}$ in Eqn. 2.14 are given by either Eqn. 2.22 or 2.26.

Using Eqn. 2.14, define in the spectral domain in terms of dyadic Green's functions

$$\tilde{G}^{zx}_{EJ} = \frac{I\ell}{4\pi\omega\epsilon_n}F^{HED}_{E_z} \tag{G.9}$$

and

$$\tilde{G}^{zx}_{HJ} = -\frac{I\ell}{4\pi}\frac{F^{HED}_{H_z}}{k_{mz}}\frac{\mu_m}{\mu_n}. \tag{G.10}$$

Before evaluation of the transverse fields in the frequency domain, the k_x and k_y dependence of the amplitudes in Eqns. G.9 and G.10 must be explicitly known. Realising

that

$$\begin{aligned} G_{EJ}^{zx} &= -j\mathcal{F}^{-1}\{jk_x\tilde{G}_{EJ}^{zx}\} \\ G_{HJ}^{zx} &= -j\mathcal{F}^{-1}\{jk_y\tilde{G}_{HJ}^{zx}\}, \end{aligned} \tag{G.11}$$

it follows that by means of a constant amplitude extraction and substitution into Eqn. G.4, the Green's functions for the transverse fields of an HED can be computed from

$$\begin{aligned} \tilde{G}_{EJ}^{xx} &= \frac{1}{k_\rho^2}\Big(jk_x^2\dot{\tilde{G}}_{EJ}^{zx} + \omega\mu k_y^2\tilde{G}_{HJ}^{zx}\Big) \\ \tilde{G}_{EJ}^{yx} &= \frac{k_xk_y}{k_\rho^2}\Big(j\dot{\tilde{G}}_{EJ}^{zx} - \omega\mu\tilde{G}_{HJ}^{zx}\Big) \\ \tilde{G}_{HJ}^{xx} &= \frac{k_xk_y}{k_\rho^2}\Big(j\dot{\tilde{G}}_{HJ}^{zx} - \omega\epsilon\tilde{G}_{EJ}^{zx}\Big) \\ \tilde{G}_{HJ}^{yx} &= \frac{1}{k_\rho^2}\Big(jk_y^2\dot{\tilde{G}}_{HJ}^{zx} + \omega\epsilon k_x^2\tilde{G}_{EJ}^{zx}\Big). \end{aligned} \tag{G.12}$$

Using the inverse Fourier identities of A.5, the Green's functions in the frequency domain are obtained.

To summarise, for the electric and magnetic fields

$$\begin{aligned} G_{EJ}^{xx} &= \cos^2\phi\, A_J + \sin^2\phi\, B_J \\ G_{EJ}^{yx} &= \sin\phi\cos\phi\,(A_J - B_J) \\ G_{EJ}^{zx} &= \cos\phi\, C_J \\ G_{HJ}^{xx} &= \sin\phi\cos\phi\,(D_J - E_J) \\ G_{HJ}^{yx} &= \sin^2\phi\, D_J + \cos^2\phi\, E_J \\ G_{HJ}^{zx} &= \sin\phi\, F_J \end{aligned} \tag{G.13}$$

where

$$\begin{aligned} A_J &= A_J^D + \int_0^\infty \Big[\Big(J_0(k_\rho\rho)k_\rho - \frac{J_1(k_\rho\rho)}{\rho}\Big)j\dot{\tilde{G}}_{EJ}^{zx} + \frac{J_1(k_\rho\rho)}{\rho}\omega\mu_n\tilde{G}_{HJ}^{zx}\Big]dk_\rho \\ B_J &= B_J^D + \int_0^\infty \Big[\Big(J_0(k_\rho\rho)k_\rho - \frac{J_1(k_\rho\rho)}{\rho}\Big)\omega\mu_n\tilde{G}_{HJ}^{zx} + \frac{J_1(k_\rho\rho)}{\rho}j\dot{\tilde{G}}_{EJ}^{zx}\Big]dk_\rho \\ C_J &= C_J^D + j\int_0^\infty J_1(k_\rho\rho)k_\rho^2\tilde{G}_{EJ}^{zx}dk_\rho \\ D_J &= D_J^D + \int_0^\infty \Big[\Big(J_0(k_\rho\rho)k_\rho - \frac{J_1(k_\rho\rho)}{\rho}\Big)j\dot{\tilde{G}}_{HJ}^{zx} + \frac{J_1(k_\rho\rho)}{\rho}\omega\epsilon_n\tilde{G}_{EJ}^{zx}\Big]dk_\rho \\ E_J &= E_J^D + \int_0^\infty \Big[\Big(J_0(k_\rho\rho)k_\rho - \frac{J_1(k_\rho\rho)}{\rho}\Big)\omega\epsilon_n\tilde{G}_{EJ}^{zx} + \frac{J_1(k_\rho\rho)}{\rho}j\dot{\tilde{G}}_{HJ}^{zx}\Big]dk_\rho \\ F_J &= F_J^D + j\int_0^\infty J_1(k_\rho\rho)k_\rho^2\tilde{G}_{HJ}^{zx}dk_\rho. \end{aligned} \tag{G.14}$$

$\tilde{G}_{EJ}^{zx}$ and $\tilde{G}_{HJ}^{zx}$ are defined in Eqns. G.9 and G.10 where $F_{E_z}^{HED}$ and $F_{H_z}^{HED}$ depend on the respective observation and source layers, n and m.

For $n = m$, $F_{E_z}^{HED}$ and $F_{H_z}^{HED}$ are given by Eqn. 2.16, but without the $e^{-jk_{mz}|z-z'|}$ term which represents the direct fields. As was shown in Eqn. G.5, the direct fields can be computed analytically,

$$\begin{aligned}
A_J^D &= \frac{I\ell}{4\pi} e^{-jk_m r}\left[\left(\frac{2\eta_m}{r^2} + \frac{2}{j\omega\epsilon_m r^3}\right)\sin^2\theta - \left(\frac{j\omega\mu_m}{r} + \frac{\eta_m}{r^2} + \frac{1}{j\omega\epsilon_m r^3}\right)\cos^2\theta\right] \\
B_J^D &= -\frac{I\ell}{4\pi} e^{-jk_m r}\left[\frac{j\omega\mu_m}{r} + \frac{\eta_m}{r^2} + \frac{1}{j\omega\epsilon_m r^3}\right] \\
C_J^D &= \frac{I\ell}{4\pi} e^{-jk_m r}\left[\frac{j\omega\mu_m}{r} + \frac{3\eta_m}{r^2} + \frac{3}{j\omega\epsilon_m r^3}\right]\sin\theta\cos\theta \\
D_J^D &= -\frac{I\ell}{4\pi} e^{-jk_m r}\left[\frac{jk_m}{r} + \frac{1}{r^2}\right]\cos\theta \\
E_J^D &= D_J^D \\
F_J^D &= \frac{I\ell}{4\pi} e^{-jk_m r}\left[\frac{jk_m}{r} + \frac{1}{r^2}\right]\sin\theta.
\end{aligned} \tag{G.15}$$

For $n < m$, $F_{E_z}^{HED}$ and $F_{H_z}^{HED}$ are given by Eqn. 2.22, and all direct fields are zero; hence, $A_J^D, ..., F_J^D = 0$.

For $n > m$, $F_{E_z}^{HED}$ and $F_{H_z}^{HED}$ are given by Eqn. 2.26, and all direct fields are zero; hence, $A_J^D, ..., F_J^D = 0$.

Similar to the above approach, the Green's functions for the fields of a VED, HMD and VMD can be computed.

G.2 Green's Functions for the Fields of a VED

Using Eqn. 2.15, define in the spectral domain in terms of dyadic Green's functions

$$\tilde{G}_{EJ}^{zz} = -\frac{I\ell}{4\pi\omega\epsilon_n}\frac{k_\rho^2}{k_{mz}} F_{E_z}^{VED}. \tag{G.16}$$

The normal field Green's functions can be written as the direct inverse Fourier transform

$$\begin{aligned}
G_{EJ}^{zz} &= \mathcal{F}^{-1}\{\tilde{G}_{EJ}^{zz}\} \\
G_{HJ}^{zz} &= \mathcal{F}^{-1}\{\tilde{G}_{HJ}^{zz}\}.
\end{aligned} \tag{G.17}$$

Note that $\tilde{G}_{HJ}^{zz} = 0$ because a vertical source in a stratified medium does not produce a vertical magnetic field.

Using the inverse Fourier identities of A.5, and the reduced transverse field relations

following from Eqn. G.4,

$$\begin{aligned}
\tilde{G}^{xz}_{EJ} &= \frac{1}{k_\rho^2} jk_x \dot{\tilde{G}}^{zz}_{EJ} \\
\tilde{G}^{yz}_{EJ} &= \frac{1}{k_\rho^2} jk_y \dot{\tilde{G}}^{zz}_{EJ} \\
\tilde{G}^{xz}_{HJ} &= -\frac{1}{k_\rho^2} \omega\epsilon k_y \tilde{G}^{zz}_{EJ} \\
\tilde{G}^{yz}_{HJ} &= \frac{1}{k_\rho^2} \omega\epsilon k_x \tilde{G}^{zz}_{EJ},
\end{aligned} \tag{G.18}$$

the total electric and magnetic field Green's functions are

$$\begin{aligned}
G^{xz}_{EJ} &= \cos\phi \, G_J \\
G^{yz}_{EJ} &= \sin\phi \, G_J \\
G^{zz}_{EJ} &= H_J \\
G^{xz}_{HJ} &= -\sin\phi \, I_J \\
G^{yz}_{HJ} &= \cos\phi \, I_J \\
G^{zz}_{HJ} &= 0
\end{aligned} \tag{G.19}$$

where the integrals G_J, H_J and I_J are given by

$$\begin{aligned}
G_J &= G_J^D - \int_0^\infty J_1(k_\rho\rho) \dot{\tilde{G}}^{zz}_{EJ} dk_\rho \\
H_J &= H_J^D + \int_0^\infty J_0(k_\rho\rho) k_\rho \tilde{G}^{zz}_{EJ} dk_\rho \\
I_J &= I_J^D + j\omega\epsilon_n \int_0^\infty J_1(k_\rho\rho) \tilde{G}^{zz}_{EJ} dk_\rho.
\end{aligned} \tag{G.20}$$

Here $F^{VED}_{E_z}$, incorporated in Eqn. G.16, depends on the observation layer, n, and the source layer, m.

For $n = m$, $F^{VED}_{E_z}$ is given by Eqn. 2.16, but without the $e^{-jk_{mz}|z-z'|}$ term. Using Eqn. G.2, the direct fields can be theoretically expressed in closed form

$$\begin{aligned}
G_J^D &= \frac{I\ell}{4\pi} e^{-jk_m r} \Big[\frac{j\omega\mu_m}{r} + \frac{3\eta_m}{r^2} + \frac{3}{j\omega\epsilon_m r^3} \Big] \sin\theta\cos\theta \\
H_J^D &= \frac{I\ell}{4\pi} e^{-jk_m r} \Big[\Big(\frac{2\eta_m}{r^2} + \frac{2}{j\omega\epsilon_m r^3} \Big) - \Big(\frac{j\omega\mu_m}{r} + \frac{3\eta_m}{r^2} + \frac{3}{j\omega\epsilon_m r^3} \Big) \sin^2\theta \Big] \\
I_J^D &= \frac{I\ell}{4\pi} e^{-jk_m r} \Big[\frac{jk_m}{r} + \frac{1}{r^2} \Big] \sin\theta.
\end{aligned} \tag{G.21}$$

For $n < m$, $F^{VED}_{E_z}$ is given by Eqn. 2.22, and all direct fields are zero, i.e. $G_J^D, ..., I_J^D = 0$.

For $n > m$, $F^{VED}_{E_z}$ is given by Eqn. 2.26, and all direct fields are zero, i.e. $G_J^D, ..., I_J^D = 0$.

G.3 Green's Functions for the Fields of an HMD

When setting up the Sommerfeld integrals for a magnetic dipole embedded in a stratified medium, the results obtained in Eqns. E.1, E.2 and E.3 are of greatest importance. The first is used to compute analytical results for the direct fields. The second and third give the two normal components, which is essential in developing the remaining transverse field Green's functions.

Applying duality and the inverse Fourier identities of A.5, the Green's functions in the frequency domain are obtained. For the total fields of an HMD

$$\begin{aligned}
G^{xx}_{EM} &= \sin\phi\cos\phi\,(D_M - E_M) \\
G^{yx}_{EM} &= \sin^2\phi\,D_M + \cos^2\phi\,E_M \\
G^{zx}_{EM} &= \sin\phi\,F_M \\
G^{xx}_{HM} &= \cos^2\phi\,A_M + \sin^2\phi\,B_M \\
G^{yx}_{HM} &= \sin\phi\cos\phi\,(A_M - B_M) \\
G^{zx}_{HM} &= \cos\phi\,C_M
\end{aligned} \tag{G.22}$$

where

$$\begin{aligned}
A_M &= A^D_M + \int_0^\infty \Big[\Big(J_0(k_\rho\rho)k_\rho - \frac{J_1(k_\rho\rho)}{\rho}\Big)j\dot{\tilde{G}}^{zx}_{HM} + \frac{J_1(k_\rho\rho)}{\rho}(-\omega\epsilon_n\tilde{G}^{zx}_{EM})\Big]dk_\rho \\
B_M &= B^D_M + \int_0^\infty \Big[\Big(J_0(k_\rho\rho)k_\rho - \frac{J_1(k_\rho\rho)}{\rho}\Big)(-\omega\epsilon_n\tilde{G}^{zx}_{EM}) + \frac{J_1(k_\rho\rho)}{\rho}j\dot{\tilde{G}}^{zx}_{HM}\Big]dk_\rho \\
C_M &= C^D_M + j\int_0^\infty J_1(k_\rho\rho)k_\rho^2\tilde{G}^{zx}_{HM}dk_\rho \\
D_M &= D^D_M + \int_0^\infty \Big[\Big(J_0(k_\rho\rho)k_\rho - \frac{J_1(k_\rho\rho)}{\rho}\Big)j\dot{\tilde{G}}^{zx}_{EM} + \frac{J_1(k_\rho\rho)}{\rho}(-\omega\mu_n\tilde{G}^{zx}_{HM})\Big]dk_\rho \\
E_M &= E^D_M + \int_0^\infty \Big[\Big(J_0(k_\rho\rho)k_\rho - \frac{J_1(k_\rho\rho)}{\rho}\Big)(-\omega\mu_n\tilde{G}^{zx}_{HM}) + \frac{J_1(k_\rho\rho)}{\rho}j\dot{\tilde{G}}^{zx}_{EM}\Big]dk_\rho \\
F_M &= F^D_M + j\int_0^\infty J_1(k_\rho\rho)k_\rho^2\tilde{G}^{zx}_{EM}dk_\rho.
\end{aligned} \tag{G.23}$$

In Eqn. G.23, the spectral domain Green's functions are

$$\tilde{G}^{zx}_{EM} = j\omega\mu_m\frac{IA}{4\pi}\frac{F^{HMD}_{E_z}}{k_{mz}}\frac{\epsilon_m}{\epsilon_n} \tag{G.24}$$

and

$$\tilde{G}^{zx}_{HM} = j\frac{IA}{4\pi}F^{HMD}_{H_z}\frac{\mu_m}{\mu_n}. \tag{G.25}$$

$F^{HMD}_{E_z}$ and $F^{HMD}_{H_z}$ depend on the observation and source layers, namely, n and m respectively.

For $n = m$, $F_{E_z}^{HMD}$ and $F_{H_z}^{HMD}$ are given by Eqn. E.4, but without the $e^{-jk_{mz}|z-z'|}$ term. When the source and observation layers are the same, the direct fields are computed analytically, giving

$$\begin{aligned}
A_M^D &= \frac{IA}{4\pi}e^{-jk_m r}\Big[\Big(\frac{2jk_m}{r^2}+\frac{2}{r^3}\Big)\sin^2\theta - \Big(-\frac{k_m^2}{r}+\frac{jk_m}{r^2}+\frac{1}{r^3}\Big)\cos^2\theta\Big] \\
B_M^D &= -\frac{IA}{4\pi}e^{-jk_m r}\Big[-\frac{k_m^2}{r}+\frac{jk_m}{r^2}+\frac{1}{r^3}\Big] \\
C_M^D &= \frac{IA}{4\pi}e^{-jk_m r}\Big[-\frac{k_m^2}{r}+\frac{3jk_m}{r^2}+\frac{3}{r^3}\Big]\sin\theta\cos\theta \\
D_M^D &= -\frac{IA}{4\pi}e^{-jk_m r}\Big[\frac{\omega\mu_m k_m}{r}-\frac{j\omega\mu_m}{r^2}\Big]\cos\theta \\
E_M^D &= D_M^D \\
F_M^D &= \frac{IA}{4\pi}e^{-jk_m r}\Big[\frac{\omega\mu_m k_m}{r}-\frac{j\omega\mu_m}{r^2}\Big]\sin\theta.
\end{aligned} \tag{G.26}$$

For $n < m$, $F_{E_z}^{HMD}$ and $F_{H_z}^{HMD}$ are given by Eqn. E.6, and all direct fields $A_M^D, ..., F_M^D$ are zero.

For $n > m$, $F_{E_z}^{HMD}$ and $F_{H_z}^{HMD}$ are given by Eqn. E.10. Similarly, all direct fields are zero, i.e., $A_M^D, ..., F_M^D = 0$.

G.4 Green's Functions for the Fields of a VMD

The principle of duality is applied to obtain the Green's function identities for the total electric and magnetic fields of a VMD as

$$\begin{aligned}
G_{EM}^{xz} &= -\sin\phi\, I_M \\
G_{EM}^{yz} &= \cos\phi\, I_M \\
G_{EM}^{zz} &= 0 \\
G_{HM}^{xz} &= \cos\phi\, G_M \\
G_{HM}^{yz} &= \sin\phi\, G_M \\
G_{HM}^{zz} &= H_M.
\end{aligned} \tag{G.27}$$

The integrals G_M, H_M and I_M are given by

$$\begin{aligned}
G_M &= G_M^D - \int_0^\infty J_1(k_\rho\rho)\dot{\tilde{G}}_{HM}^{zz}dk_\rho \\
H_M &= H_M^D + \int_0^\infty J_0(k_\rho\rho)k_\rho\tilde{G}_{HM}^{zz}dk_\rho \\
I_M &= I_M^D - j\omega\mu_n\int_0^\infty J_1(k_\rho\rho)\tilde{G}_{HM}^{zz}dk_\rho
\end{aligned} \tag{G.28}$$

where

$$\tilde{G}^{zz}_{HM} = \frac{IA}{4\pi}\frac{k_\rho^2}{jk_{mz}}F^{VMD}_{H_z}\frac{\mu_m}{\mu_n}. \tag{G.29}$$

In Eqn. G.29, $F^{VMD}_{H_z}$ depends on the observation layer, n, and the source layer, m.

For $n = m$, $F^{VMD}_{H_z}$ is given by Eqn. E.4, but without the $e^{-jk_{mz}|z-z'|}$ term which represents the direct fields. Closed form solutions for the direct fields are

$$\begin{aligned}
G^D_M &= \frac{IA}{4\pi}e^{-jk_m r}\Big[-\frac{k_m^2}{r} + \frac{3jk_m}{r^2} + \frac{3}{r^3}\Big]\sin\theta\cos\theta \\
H^D_M &= \frac{IA}{4\pi}e^{-jk_m r}\Big[\Big(\frac{2jk_m}{r^2} + \frac{2}{r^3}\Big) - \Big(-\frac{k_m^2}{r} + \frac{3jk_m}{r^2} + \frac{3}{r^3}\Big)\sin^2\theta\Big] \\
I^D_M &= \frac{IA}{4\pi}e^{-jk_m r}\Big[\frac{\omega\mu_m k_m}{r} - \frac{j\omega\mu_m}{r^2}\Big]\sin\theta.
\end{aligned} \tag{G.30}$$

For $n < m$, $F^{VMD}_{H_z}$ is given by Eqn. E.6. All direct fields are zero ($G^D_M, ..., I^D_M = 0$).

For $n > m$, $F^{VMD}_{H_z}$ is given by Eqn. E.10. All direct fields are zero ($G^D_M, ..., I^D_M = 0$).

G.5 Conclusion

Green's functions for the total electric and magnetic fields were formulated in a suitable form to be used with the triangular method of moments. Van Tonder [24] presented a convenient method to evaluate the total **E** and **H** fields due to currents on electric scatterers, which can be extended to possible equivalent magnetic slot apertures. The observation point may be in any layer and at any arbitrary distance within that layer. Van Tonder's formulation focussed on the computational analysis for a horizontal electric dipole source. This may be used as a basis to extend evaluations to consider vertical electric dipole sources as well as the combination of electric and magnetic sources.

Appendix H

Evaluation of Dipole Near-Fields

Similar to extracting static terms from the potential Green's functions to increase convergence, near-field static terms can be extracted from the total field Green's functions. The terms extracted depends on the respective source and observation layers. When $|n-m|>1$, no extraction is done and the Sommerfeld integrals remain as in Eqns. G.14, G.20, G.23 and G.28 with all direct fields zero.

Evaluation of Electric Dipole Near-Fields

When near fields are evaluated with the source and observation points close to an interface, near-field singular terms can be extracted from the total field Green's functions. This approach is similar to that explained in Chapter 3 Section 3.3.

When the source and observation points are in adjacent layers, $|n-m|=1$, the Sommerfeld integrals for the total field Green's functions in the space domain can be written as

$$\begin{aligned} A_J = \frac{I\ell}{4\pi}\int_0^\infty \Big[\Big(J_0(k_\rho\rho)k_\rho - \frac{J_1(k_\rho\rho)}{\rho}\Big)\Big(\frac{j}{\omega\epsilon_n}\Big)\Big(\dot{F}_{E_z}^{HED} - T_J^{TM,\infty} jk_{iz}e^{-jk_{iz}s}\Big) \\ + \frac{J_1(k_\rho\rho)}{\rho}\Big(\frac{-\omega\mu_n F_{H_z}^{HED}}{k_{mz}}\frac{\mu_m}{\mu_n}\Big)\Big]dk_\rho \\ + \frac{I\ell}{4\pi}\frac{j}{\omega\epsilon_n}T_J^{TM,\infty}\Big[\frac{\partial^2}{\partial s^2}\Big(\frac{e^{-jk_i r}}{r}\Big) + \frac{1}{\rho^2}\frac{\partial}{\partial s}\Big(e^{-jk_i s} - \frac{s}{r}e^{-jk_i r}\Big)\Big] \end{aligned}$$

$$B_J = \frac{I\ell}{4\pi}\int_0^\infty \Big[\Big(J_0(k_\rho\rho)k_\rho - \frac{J_1(k_\rho\rho)}{\rho}\Big)\Big(\frac{-\omega\mu_n F^{HED}_{H_z}}{k_{mz}}\frac{\mu_m}{\mu_n}\Big) + \frac{J_1(k_\rho\rho)}{\rho}\Big(\frac{j}{\omega\epsilon_n}\Big)\Big(\dot{F}^{HED}_{E_z} - T^{TM,\infty}_J jk_{iz}e^{-jk_{iz}s}\Big)\Big]dk_\rho - \frac{I\ell}{4\pi}\frac{j}{\omega\epsilon_n}T^{TM,\infty}_J\frac{1}{\rho^2}\frac{\partial}{\partial s}\Big(e^{-jk_is} - \frac{s}{r}e^{-jk_ir}\Big)$$

$$C_J = \frac{I\ell}{4\pi}\frac{j}{\omega\epsilon_n}\int_0^\infty J_1(k_\rho\rho)k_\rho^2\Big(F^{HED}_{E_z} + \mathrm{sign}(z-z')T^{TM,\infty}_J e^{-jk_{iz}s}\Big)dk_\rho - \mathrm{sign}(z-z')\frac{I\ell}{4\pi}\frac{j}{\omega\epsilon_n}T^{TM,\infty}_J e^{-jk_ir}\Big(-\frac{k_i^2}{r} + \frac{3jk_i}{r^2} + \frac{3}{r^3}\Big)\sin\theta\cos\theta$$

$$D_J = \frac{I\ell}{4\pi}\int_0^\infty \Big[\Big(J_0(k_\rho\rho)k_\rho - \frac{J_1(k_\rho\rho)}{\rho}\Big)\Big(\frac{\dot{F}^{HED}_{H_z}}{jk_{mz}}\frac{\mu_m}{\mu_n} + \mathrm{sign}(z-z')T^{TE,\infty}_J e^{-jk_{iz}s}\Big) + \frac{J_1(k_\rho\rho)}{\rho}\Big(F^{HED}_{E_z} + \mathrm{sign}(z-z')T^{TM,\infty}_J e^{-jk_{iz}s}\Big)\Big]dk_\rho + \mathrm{sign}(z-z')\frac{I\ell}{4\pi}\Big[T^{TE,\infty}_J\frac{\partial}{\partial s}\Big(\frac{e^{-jk_ir}}{r}\Big) + (T^{TE,\infty}_J - T^{TM,\infty}_J)\frac{1}{\rho^2}\Big(e^{-jk_is} - \frac{s}{r}e^{-jk_ir}\Big)\Big]$$

$$E_J = \frac{I\ell}{4\pi}\int_0^\infty \Big[\Big(J_0(k_\rho\rho)k_\rho - \frac{J_1(k_\rho\rho)}{\rho}\Big)\Big(F^{HED}_{E_z} + \mathrm{sign}(z-z')T^{TM,\infty}_J e^{-jk_{iz}s}\Big) + \frac{J_1(k_\rho\rho)}{\rho}\Big(\frac{\dot{F}^{HED}_{H_z}}{jk_{mz}}\frac{\mu_m}{\mu_n} + T^{TE,\infty}_J e^{-jk_{iz}s}\Big)\Big]dk_\rho + \mathrm{sign}(z-z')\frac{I\ell}{4\pi}\Big[T^{TM,\infty}_J\frac{\partial}{\partial s}\Big(\frac{e^{-jk_ir}}{r}\Big) + (T^{TM,\infty}_J - T^{TE,\infty}_J)\frac{1}{\rho^2}\Big(e^{-jk_is} - \frac{s}{r}e^{-jk_ir}\Big)\Big]$$

$$F_J = \frac{I\ell}{4\pi}\int_0^\infty J_1(k_\rho\rho)k_\rho^2\Big(\frac{F^{HED}_{H_z}}{jk_{mz}}\frac{\mu_m}{\mu_n} - T^{TE,\infty}_J\frac{e^{-jk_{iz}s}}{jk_{iz}}\Big)dk_\rho + \frac{I\ell}{4\pi}T^{TE,\infty}_J e^{-jk_ir}\Big(\frac{jk_i}{r} + \frac{1}{r^2}\Big)\sin\theta$$

$$G_J = \frac{I\ell}{4\pi}\frac{j}{\omega\epsilon_n}\int_0^\infty J_1(k_\rho\rho)k_\rho^2\Big(\frac{\dot{F}^{VED}_{E_z}}{jk_{mz}} + \mathrm{sign}(z-z')T^{TM,\infty}_J e^{-jk_{iz}s}\Big)dk_\rho - \mathrm{sign}(z-z')\frac{I\ell}{4\pi}\frac{j}{\omega\epsilon_n}T^{TM,\infty}_J e^{-jk_ir}\Big(-\frac{k_i^2}{r} + \frac{3jk_i}{r^2} + \frac{3}{r^3}\Big)\sin\theta\cos\theta$$

$$H_J = \frac{I\ell}{4\pi}\frac{j}{\omega\epsilon_n}\int_0^\infty J_0(k_\rho\rho)k_\rho\Big(-\frac{k_\rho^2 F^{VED}_{E_z}}{jk_{mz}} + T^{TM,\infty}_J jk_{iz}e^{-jk_{iz}s}\Big)dk_\rho - \frac{I\ell}{4\pi}\frac{j}{\omega\epsilon_n}T^{TM,\infty}_J\frac{\partial^2}{\partial s^2}\Big(\frac{e^{-jk_ir}}{r}\Big)$$

$$
\begin{aligned}
I_J = \frac{I\ell}{4\pi}\int_0^\infty J_1(k_\rho\rho)k_\rho^2\Big(\frac{F_{E_z}^{VED}}{jk_{mz}} - T_J^{TM,\infty}\frac{e^{-jk_{iz}s}}{jk_{iz}}\Big)dk_\rho \\
+ \frac{I\ell}{4\pi}T_J^{TM,\infty}e^{-jk_i r}\Big(\frac{jk_i}{r}+\frac{1}{r^2}\Big)\sin\theta
\end{aligned}
\tag{H.1}
$$

Similarly, when the source and observation layers are equal, $m = n$, the Sommerfeld integrals can be written as

$$
\begin{aligned}
A_J = A_J^D + \frac{I\ell}{4\pi}\int_0^\infty \Big[\Big(J_0(k_\rho\rho)k_\rho - \frac{J_1(k_\rho\rho)}{\rho}\Big)\Big(\frac{j}{\omega\epsilon_m}\Big)\Big(\dot F_{E_z}^{HED} + R_{m,m-1}^{TM,\infty}jk_{mz}e^{-jk_{mz}s_1} \\
+ R_{m,m+1}^{TM,\infty}jk_{mz}e^{-jk_{mz}s_2}\Big) + \frac{J_1(k_\rho\rho)}{\rho}\Big(\frac{-\omega\mu_m F_{H_z}^{HED}}{k_{mz}}\Big)\Big]dk_\rho \\
- \frac{I\ell}{4\pi}\frac{j}{\omega\epsilon_m}R_{m,m-1}^{TM,\infty}\Big[\frac{\partial^2}{\partial s_1^2}\Big(\frac{e^{-jk_m r_1}}{r_1}\Big) + \frac{1}{\rho^2}\frac{\partial}{\partial s_1}\Big(e^{-jk_m s_1} - \frac{s_1}{r_1}e^{-jk_m r_1}\Big)\Big] \\
- \frac{I\ell}{4\pi}\frac{j}{\omega\epsilon_m}R_{m,m+1}^{TM,\infty}\Big[\frac{\partial^2}{\partial s_2^2}\Big(\frac{e^{-jk_m r_2}}{r_2}\Big) + \frac{1}{\rho^2}\frac{\partial}{\partial s_2}\Big(e^{-jk_m s_2} - \frac{s_2}{r_2}e^{-jk_m r_2}\Big)\Big]
\end{aligned}
$$

$$
\begin{aligned}
B_J = B_J^D + \frac{I\ell}{4\pi}\int_0^\infty \Big[\Big(J_0(k_\rho\rho)k_\rho - \frac{J_1(k_\rho\rho)}{\rho}\Big)\Big(\frac{-\omega\mu_m F_{H_z}^{HED}}{k_{mz}}\Big) \\
+ \frac{J_1(k_\rho\rho)}{\rho}\Big(\frac{j}{\omega\epsilon_m}\Big)\Big(\dot F_{E_z}^{HED} + R_{m,m-1}^{TM,\infty}jk_{mz}e^{-jk_{mz}s_1} + R_{m,m+1}^{TM,\infty}jk_{mz}e^{-jk_{mz}s_2}\Big)\Big]dk_\rho \\
+ \frac{I\ell}{4\pi}\frac{j}{\omega\epsilon_m}R_{m,m-1}^{TM,\infty}\frac{1}{\rho^2}\frac{\partial}{\partial s_1}\Big(e^{-jk_m s_1} - \frac{s_1}{r_1}e^{-jk_m r_1}\Big) \\
+ \frac{I\ell}{4\pi}\frac{j}{\omega\epsilon_m}R_{m,m+1}^{TM,\infty}\frac{1}{\rho^2}\frac{\partial}{\partial s_2}\Big(e^{-jk_m s_2} - \frac{s_2}{r_2}e^{-jk_m r_2}\Big)
\end{aligned}
$$

$$
\begin{aligned}
C_J = C_J^D + \frac{I\ell}{4\pi}\frac{j}{\omega\epsilon_m}\int_0^\infty J_1(k_\rho\rho)k_\rho^2\Big(F_{E_z}^{HED} + R_{m,m-1}^{TM,\infty}e^{-jk_{mz}s_1} - R_{m,m+1}^{TM,\infty}e^{-jk_{mz}s_2}\Big)dk_\rho \\
+ \frac{I\ell}{4\pi}R_{m,m-1}^{TM,\infty}e^{-jk_m r_1}\Big(\frac{j\omega\mu_m}{r_1} + \frac{3\eta_m}{r_1^2} + \frac{3}{j\omega\epsilon_m r_1^3}\Big)\sin\theta_1\cos\theta_1 \\
- \frac{I\ell}{4\pi}R_{m,m+1}^{TM,\infty}e^{-jk_m r_2}\Big(\frac{j\omega\mu_m}{r_2} + \frac{3\eta_m}{r_2^2} + \frac{3}{j\omega\epsilon_m r_2^3}\Big)\sin\theta_2\cos\theta_2
\end{aligned}
$$

$$
\begin{aligned}
D_J = D_J^D + \frac{I\ell}{4\pi}\int_0^\infty \Big[\Big(J_0(k_\rho\rho)k_\rho - \frac{J_1(k_\rho\rho)}{\rho}\Big)\Big(\frac{\dot F_{H_z}^{HED}}{jk_{mz}} - R_{m,m-1}^{TE,\infty}e^{-jk_{mz}s_1} + R_{m,m+1}^{TE,\infty}e^{-jk_{mz}s_2}\Big) \\
+ \frac{J_1(k_\rho\rho)}{\rho}\Big(F_{E_z}^{HED} + R_{m,m-1}^{TM,\infty}e^{-jk_{mz}s_1} - R_{m,m+1}^{TM,\infty}e^{-jk_{mz}s_2}\Big)\Big]dk_\rho \\
- \frac{I\ell}{4\pi}\Big[R_{m,m-1}^{TE,\infty}\frac{\partial}{\partial s_1}\Big(\frac{e^{-jk_m r_1}}{r_1}\Big) - R_{m,m+1}^{TE,\infty}\frac{\partial}{\partial s_2}\Big(\frac{e^{-jk_m r_2}}{r_2}\Big)\Big] \\
- \frac{I\ell}{4\pi}\Big(R_{m,m-1}^{TE,\infty} + R_{m,m-1}^{TM,\infty}\Big)\frac{1}{\rho^2}\Big(e^{-jk_m s_1} - \frac{s_1}{r_1}e^{-jk_m r_1}\Big) \\
+ \frac{I\ell}{4\pi}\Big(R_{m,m+1}^{TE,\infty} + R_{m,m+1}^{TM,\infty}\Big)\frac{1}{\rho^2}\Big(e^{-jk_m s_2} - \frac{s_2}{r_2}e^{-jk_m r_2}\Big)
\end{aligned}
$$

$$
\begin{aligned}
E_J = E_J^D &+ \frac{I\ell}{4\pi}\int_0^\infty \Big[\Big(J_0(k_\rho\rho)k_\rho - \frac{J_1(k_\rho\rho)}{\rho}\Big)\Big(F_{E_z}^{HED} + R_{m,m-1}^{TM,\infty}e^{-jk_{mz}s_1} - R_{m,m+1}^{TM,\infty}e^{-jk_{mz}s_2}\Big) \\
&+ \frac{J_1(k_\rho\rho)}{\rho}\Big(\frac{\dot{F}_{H_z}^{HED}}{jk_{mz}} - R_{m,m-1}^{TE,\infty}e^{-jk_{mz}s_1} + R_{m,m+1}^{TE,\infty}e^{-jk_{mz}s_2}\Big)\Big]dk_\rho \\
&+ \frac{I\ell}{4\pi}\Big[R_{m,m-1}^{TM,\infty}\frac{\partial}{\partial s_1}\Big(\frac{e^{-jk_m r_1}}{r_1}\Big) - R_{m,m+1}^{TM,\infty}\frac{\partial}{\partial s_2}\Big(\frac{e^{-jk_m r_2}}{r_2}\Big)\Big] \\
&+ \frac{I\ell}{4\pi}\Big(R_{m,m-1}^{TM,\infty} + R_{m,m-1}^{TE,\infty}\Big)\frac{1}{\rho^2}\Big(e^{-jk_m s_1} - \frac{s_1}{r_1}e^{-jk_m r_1}\Big) \\
&- \frac{I\ell}{4\pi}\Big(R_{m,m+1}^{TM,\infty} + R_{m,m+1}^{TE,\infty}\Big)\frac{1}{\rho^2}\Big(e^{-jk_m s_2} - \frac{s_2}{r_2}e^{-jk_m r_2}\Big)
\end{aligned}
$$

$$
\begin{aligned}
F_J = F_J^D &+ \frac{I\ell}{4\pi}\int_0^\infty J_1(k_\rho\rho)\frac{k_\rho^2}{jk_{mz}}\Big(F_{H_z}^{HED} - R_{m,m-1}^{TE,\infty}e^{-jk_{mz}s_1} - R_{m,m+1}^{TE,\infty}e^{-jk_{mz}s_2}\Big)dk_\rho \\
&+ \frac{I\ell}{4\pi}R_{m,m-1}^{TE,\infty}e^{-jk_m r_1}\Big(\frac{jk_m}{r_1} + \frac{1}{r_1^2}\Big)\sin\theta_1 + \frac{I\ell}{4\pi}R_{m,m+1}^{TE,\infty}e^{-jk_m r_2}\Big(\frac{jk_m}{r_2} + \frac{1}{r_2^2}\Big)\sin\theta_2
\end{aligned}
$$

$$
\begin{aligned}
G_J = G_J^D &+ \frac{I\ell}{4\pi}\frac{j}{\omega\epsilon_m}\int_0^\infty J_1(k_\rho\rho)k_\rho^2\Big(\frac{\dot{F}_{E_z}^{VED}}{jk_{mz}} - R_{m,m-1}^{TM,\infty}e^{-jk_{mz}s_1} + R_{m,m+1}^{TM,\infty}e^{-jk_{mz}s_2}\Big)dk_\rho \\
&- \frac{I\ell}{4\pi}R_{m,m-1}^{TM,\infty}e^{-jk_m r_1}\Big(\frac{j\omega\mu_m}{r_1} + \frac{3\eta_m}{r_1^2} + \frac{3}{j\omega\epsilon_m r_1^3}\Big)\sin\theta_1\cos\theta_1 \\
&+ \frac{I\ell}{4\pi}R_{m,m+1}^{TM,\infty}e^{-jk_m r_2}\Big(\frac{j\omega\mu_m}{r_2} + \frac{3\eta_m}{r_2^2} + \frac{3}{j\omega\epsilon_m r_2^3}\Big)\sin\theta_2\cos\theta_2
\end{aligned}
$$

$$
\begin{aligned}
H_J = H_J^D &+ \frac{I\ell}{4\pi}\frac{j}{\omega\epsilon_m}\int_0^\infty J_0(k_\rho\rho)k_\rho\Big(\frac{-k_\rho^2 F_{E_z}^{VED}}{jk_{mz}} \\
&+ jk_{mz}(R_{m,m-1}^{TM,\infty}e^{-jk_{mz}s_1} + R_{m,m+1}^{TM,\infty}e^{-jk_{mz}s_2})\Big)dk_\rho \\
&- \frac{I\ell}{4\pi}\frac{j}{\omega\epsilon_m}\Big[R_{m,m-1}^{TM,\infty}\frac{\partial^2}{\partial s_1^2}\Big(\frac{e^{-jk_m r_1}}{r_1}\Big) + R_{m,m+1}^{TM,\infty}\frac{\partial^2}{\partial s_2^2}\Big(\frac{e^{-jk_m r_2}}{r_2}\Big)\Big]
\end{aligned}
$$

$$
\begin{aligned}
I_J = I_J^D &+ \frac{I\ell}{4\pi}\int_0^\infty J_1(k_\rho\rho)\frac{k_\rho^2}{jk_{mz}}\Big(F_{E_z}^{VED} - R_{m,m-1}^{TM,\infty}e^{-jk_{mz}s_1} - R_{m,m+1}^{TM,\infty}e^{-jk_{mz}s_2}\Big)dk_\rho \\
&+ \frac{I\ell}{4\pi}R_{m,m-1}^{TM,\infty}e^{-jk_m r_1}\Big(\frac{jk_m}{r_1} + \frac{1}{r_1^2}\Big)\sin\theta_1 + \frac{I\ell}{4\pi}R_{m,m+1}^{TM,\infty}e^{-jk_m r_2}\Big(\frac{jk_m}{r_2} + \frac{1}{r_2^2}\Big)\sin\theta_2
\end{aligned}
\tag{H.2}
$$

Evaluation of Magnetic Dipole Near-Fields

When the source and observation points are in adjacent layers, $|n-m|=1$, the Sommerfeld integrals can be written as

$$A_M = -\frac{IA}{4\pi}\frac{k_m^2}{k_n^2}\int_0^\infty \Big[\Big(J_0(k_\rho\rho)k_\rho - \frac{J_1(k_\rho\rho)}{\rho}\Big)\Big(\dot{F}_{H_z}^{HMD}\frac{\epsilon_n}{\epsilon_m} - T_M^{TE,\infty} jk_{iz}e^{-jk_{iz}s}\Big) + \frac{J_1(k_\rho\rho)}{\rho}\Big(\frac{jk_n^2 F_{E_z}^{HMD}}{k_{mz}}\Big)\Big]dk_\rho - \frac{IA}{4\pi}\frac{k_m^2}{k_n^2}T_M^{TE,\infty}\Big[\frac{\partial^2}{\partial s^2}\Big(\frac{e^{-jk_ir}}{r}\Big) + \frac{1}{\rho^2}\frac{\partial}{\partial s}\Big(e^{-jk_is} - \frac{s}{r}e^{-jk_ir}\Big)\Big]$$

$$B_M = -\frac{IA}{4\pi}\frac{k_m^2}{k_n^2}\int_0^\infty \Big[\Big(J_0(k_\rho\rho)k_\rho - \frac{J_1(k_\rho\rho)}{\rho}\Big)\Big(\frac{jk_n^2 F_{E_z}^{HMD}}{k_{mz}}\Big) + \frac{J_1(k_\rho\rho)}{\rho}\Big(\dot{F}_{H_z}^{HMD}\frac{\epsilon_n}{\epsilon_m} - T_M^{TE,\infty} jk_{iz}e^{-jk_{iz}s}\Big)\Big]dk_\rho + \frac{IA}{4\pi}\frac{k_m^2}{k_n^2}T_M^{TE,\infty}\frac{1}{\rho^2}\frac{\partial}{\partial s}\Big(e^{-jk_is} - \frac{s}{r}e^{-jk_ir}\Big)$$

$$C_M = -\frac{IA}{4\pi}\frac{k_m^2}{k_n^2}\int_0^\infty J_1(k_\rho\rho)k_\rho^2\Big(F_{H_z}^{HMD}\frac{\epsilon_n}{\epsilon_m} + \mathrm{sign}(z-z')T_M^{TE,\infty}e^{-jk_{iz}s}\Big)dk_\rho + \mathrm{sign}(z-z')\frac{IA}{4\pi}\frac{k_m^2}{k_n^2}T_M^{TE,\infty}e^{-jk_ir}\Big(-\frac{k_i^2}{r} + \frac{3jk_i}{r^2} + \frac{3}{r^3}\Big)\sin\theta\cos\theta$$

$$D_M = \frac{IA}{4\pi}\frac{k_m^2}{j\omega\epsilon_n}\int_0^\infty \Big[\Big(J_0(k_\rho\rho)k_\rho - \frac{J_1(k_\rho\rho)}{\rho}\Big)\Big(\frac{\dot{F}_{E_z}^{HMD}}{jk_{mz}} + \mathrm{sign}(z-z')T_M^{TM,\infty}e^{-jk_{iz}s}\Big) + \frac{J_1(k_\rho\rho)}{\rho}\Big(F_{H_z}^{HMD}\frac{\epsilon_n}{\epsilon_m} + \mathrm{sign}(z-z')T_M^{TE,\infty}e^{-jk_{iz}s}\Big)\Big]dk_\rho + \mathrm{sign}(z-z')\frac{IA}{4\pi}\frac{k_m^2}{j\omega\epsilon_n}\Big[T_M^{TM,\infty}\frac{\partial}{\partial s}\Big(\frac{e^{-jk_ir}}{r}\Big) + (T_M^{TM,\infty} - T_M^{TE,\infty})\frac{1}{\rho^2}\Big(e^{-jk_is} - \frac{s}{r}e^{-jk_ir}\Big)\Big]$$

$$E_M = \frac{IA}{4\pi}\frac{k_m^2}{j\omega\epsilon_n}\int_0^\infty \Big[\Big(J_0(k_\rho\rho)k_\rho - \frac{J_1(k_\rho\rho)}{\rho}\Big)\Big(F_{H_z}^{HMD}\frac{\epsilon_n}{\epsilon_m} + \mathrm{sign}(z-z')T_M^{TE,\infty}e^{-jk_{iz}s}\Big) + \frac{J_1(k_\rho\rho)}{\rho}\Big(\frac{\dot{F}_{E_z}^{HMD}}{jk_{mz}}\frac{\mu_m}{\mu_n} + T_M^{TM,\infty}e^{-jk_{iz}s}\Big)\Big]dk_\rho + \mathrm{sign}(z-z')\frac{IA}{4\pi}\frac{k_m^2}{j\omega\epsilon_n}\Big[T_M^{TE,\infty}\frac{\partial}{\partial s}\Big(\frac{e^{-jk_ir}}{r}\Big) + (T_M^{TE,\infty} - T_M^{TM,\infty})\frac{1}{\rho^2}\Big(e^{-jk_is} - \frac{s}{r}e^{-jk_ir}\Big)\Big]$$

$$
\begin{aligned}
F_M &= \frac{IA}{4\pi}\frac{k_m^2}{j\omega\epsilon_n}\int_0^\infty J_1(k_\rho\rho)k_\rho^2\Big(\frac{F_{E_z}^{HMD}}{jk_{mz}} - T_M^{TM,\infty}\frac{e^{-jk_{iz}s}}{jk_{iz}}\Big)dk_\rho \\
&\quad + \frac{IA}{4\pi}\frac{k_m^2}{j\omega\epsilon_n}T_M^{TM,\infty}e^{-jk_ir}\Big(\frac{jk_i}{r}+\frac{1}{r^2}\Big)\sin\theta \\
\\
G_M &= -\frac{IA}{4\pi}\frac{k_m^2}{k_n^2}\int_0^\infty J_1(k_\rho\rho)k_\rho^2\Big(\frac{\dot{F}_{H_z}^{VMD}}{jk_{mz}}\frac{\epsilon_n}{\epsilon_m} + \mathrm{sign}(z-z')T_M^{TE,\infty}e^{-jk_{iz}s}\Big)dk_\rho \\
&\quad + \mathrm{sign}(z-z')\frac{IA}{4\pi}\frac{k_m^2}{k_n^2}T_M^{TE,\infty}e^{-jk_ir}\Big(-\frac{k_i^2}{r}+\frac{3jk_i}{r^2}+\frac{3}{r^3}\Big)\sin\theta\cos\theta \\
\\
H_M &= -\frac{IA}{4\pi}\frac{k_m^2}{k_n^2}\int_0^\infty J_0(k_\rho\rho)k_\rho\Big(\frac{-k_\rho^2F_{H_z}^{VMD}}{jk_{mz}}\frac{\epsilon_n}{\epsilon_m} + T_M^{TE,\infty}jk_{iz}e^{-jk_{iz}s}\Big)dk_\rho \\
&\quad + \frac{IA}{4\pi}\frac{k_m^2}{k_n^2}T_M^{TE,\infty}\frac{\partial^2}{\partial s^2}\Big(\frac{e^{-jk_ir}}{r}\Big) \\
\\
I_M &= \frac{IA}{4\pi}\frac{k_m^2}{j\omega\epsilon_n}\int_0^\infty J_1(k_\rho\rho)k_\rho^2\Big(\frac{F_{H_z}^{VMD}}{jk_{mz}}\frac{\epsilon_n}{\epsilon_m} - T_M^{TE,\infty}\frac{e^{-jk_{iz}s}}{jk_{iz}}\Big)dk_\rho \\
&\quad + \frac{IA}{4\pi}\frac{k_m^2}{j\omega\epsilon_n}T_M^{TE,\infty}e^{-jk_ir}\Big(\frac{jk_i}{r}+\frac{1}{r^2}\Big)\sin\theta
\end{aligned}
\tag{H.3}
$$

Similarly, when the observation and source points are located in the same layer, $n = m$, the Sommerfeld integrals for the total field Green's functions can be written as

$$
\begin{aligned}
A_M &= A_M^D - \frac{IA}{4\pi}\int_0^\infty\Big[\Big(J_0(k_\rho\rho)k_\rho - \frac{J_1(k_\rho\rho)}{\rho}\Big)\Big(\dot{F}_{H_z}^{HMD} + R_{m,m-1}^{TE,\infty}jk_{mz}e^{-jk_{mz}s_1} \\
&\quad + R_{m,m+1}^{TE,\infty}jk_{mz}e^{-jk_{mz}s_2}\Big) + \frac{J_1(k_\rho\rho)}{\rho}\Big(\frac{-k_m^2F_{E_z}^{HMD}}{jk_{mz}}\Big)\Big]dk_\rho \\
&\quad + \frac{IA}{4\pi}R_{m,m-1}^{TE,\infty}\Big[\frac{\partial^2}{\partial s_1^2}\Big(\frac{e^{-jk_mr_1}}{r_1}\Big) + \frac{1}{\rho^2}\frac{\partial}{\partial s_1}\Big(e^{-jk_ms_1} - \frac{s_1}{r_1}e^{-jk_mr_1}\Big)\Big] \\
&\quad + \frac{IA}{4\pi}R_{m,m+1}^{TE,\infty}\Big[\frac{\partial^2}{\partial s_2^2}\Big(\frac{e^{-jk_mr_2}}{r_2}\Big) + \frac{1}{\rho^2}\frac{\partial}{\partial s_2}\Big(e^{-jk_ms_2} - \frac{s_2}{r_2}e^{-jk_mr_2}\Big)\Big] \\
\\
B_M &= B_M^D - \frac{IA}{4\pi}\int_0^\infty\Big[\Big(J_0(k_\rho\rho)k_\rho - \frac{J_1(k_\rho\rho)}{\rho}\Big)\Big(\frac{-k_m^2F_{E_z}^{HMD}}{jk_{mz}}\Big) \\
&\quad + \frac{J_1(k_\rho\rho)}{\rho}\Big(\dot{F}_{H_z}^{HMD} + R_{m,m-1}^{TE,\infty}jk_{mz}e^{-jk_{mz}s_1} + R_{m,m+1}^{TE,\infty}jk_{mz}e^{-jk_{mz}s_2}\Big)\Big]dk_\rho \\
&\quad - \frac{IA}{4\pi}R_{m,m-1}^{TE,\infty}\frac{1}{\rho^2}\frac{\partial}{\partial s_1}\Big(e^{-jk_ms_1} - \frac{s_1}{r_1}e^{-jk_mr_1}\Big) \\
&\quad - \frac{IA}{4\pi}R_{m,m+1}^{TE,\infty}\frac{1}{\rho^2}\frac{\partial}{\partial s_2}\Big(e^{-jk_ms_2} - \frac{s_2}{r_2}e^{-jk_mr_2}\Big)
\end{aligned}
$$

$$C_M = C_M^D - \frac{IA}{4\pi}\int_0^\infty J_1(k_\rho\rho)k_\rho^2\Big(F_{H_z}^{HMD} + R_{m,m-1}^{TE,\infty}e^{-jk_{mz}s_1} - R_{m,m+1}^{TE,\infty}e^{-jk_{mz}s_2}\Big)dk_\rho$$
$$+ \frac{IA}{4\pi}R_{m,m-1}^{TE,\infty}e^{-jk_mr_1}\Big(-\frac{k_m^2}{r_1} + \frac{3jk_m}{r_1^2} + \frac{3}{r_1^3}\Big)\sin\theta_1\cos\theta_1$$
$$- \frac{IA}{4\pi}R_{m,m+1}^{TE,\infty}e^{-jk_mr_2}\Big(-\frac{k_m^2}{r_2} + \frac{3jk_m}{r_2^2} + \frac{3}{r_2^3}\Big)\sin\theta_2\cos\theta_2$$

$$D_M = D_M^D - j\omega\mu_m\frac{IA}{4\pi}\int_0^\infty\Big[\Big(J_0(k_\rho\rho)k_\rho - \frac{J_1(k_\rho\rho)}{\rho}\Big)\Big(\frac{\dot{F}_{E_z}^{HMD}}{jk_{mz}} - R_{m,m-1}^{TM,\infty}e^{-jk_{mz}s_1}$$
$$+ R_{m,m+1}^{TM,\infty}e^{-jk_{mz}s_2}\Big) + \frac{J_1(k_\rho\rho)}{\rho}\Big(F_{H_z}^{HMD} + R_{m,m-1}^{TE,\infty}e^{-jk_{mz}s_1} - R_{m,m+1}^{TE,\infty}e^{-jk_{mz}s_2}\Big)\Big]dk_\rho$$
$$+ j\omega\mu_m\frac{IA}{4\pi}\Big[R_{m,m-1}^{TM,\infty}\frac{\partial}{\partial s_1}\Big(\frac{e^{-jk_mr_1}}{r_1}\Big) - R_{m,m+1}^{TM,\infty}\frac{\partial}{\partial s_2}\Big(\frac{e^{-jk_mr_2}}{r_2}\Big)\Big]$$
$$+ j\omega\mu_m\frac{IA}{4\pi}\Big(R_{m,m-1}^{TM,\infty} + R_{m,m-1}^{TE,\infty}\Big)\frac{1}{\rho^2}\Big(e^{-jk_ms_1} - \frac{s_1}{r_1}e^{-jk_mr_1}\Big)$$
$$- j\omega\mu_m\frac{IA}{4\pi}\Big(R_{m,m+1}^{TM,\infty} + R_{m,m+1}^{TE,\infty}\Big)\frac{1}{\rho^2}\Big(e^{-jk_ms_2} - \frac{s_2}{r_2}e^{-jk_mr_2}\Big)$$

$$E_M = E_M^D - j\omega\mu_m\frac{IA}{4\pi}\int_0^\infty\Big[\Big(J_0(k_\rho\rho)k_\rho - \frac{J_1(k_\rho\rho)}{\rho}\Big)\Big(F_{H_z}^{HMD} + R_{m,m-1}^{TE,\infty}e^{-jk_{mz}s_1}$$
$$- R_{m,m+1}^{TE,\infty}e^{-jk_{mz}s_2}\Big) + \frac{J_1(k_\rho\rho)}{\rho}\Big(\frac{\dot{F}_{E_z}^{HMD}}{jk_{mz}} - R_{m,m-1}^{TM,\infty}e^{-jk_{mz}s_1} + R_{m,m+1}^{TM,\infty}e^{-jk_{mz}s_2}\Big)\Big]dk_\rho$$
$$- j\omega\mu_m\frac{IA}{4\pi}\Big[R_{m,m-1}^{TE,\infty}\frac{\partial}{\partial s_1}\Big(\frac{e^{-jk_mr_1}}{r_1}\Big) - R_{m,m+1}^{TE,\infty}\frac{\partial}{\partial s_2}\Big(\frac{e^{-jk_mr_2}}{r_2}\Big)\Big]$$
$$- j\omega\mu_m\frac{IA}{4\pi}\Big(R_{m,m-1}^{TE,\infty} + R_{m,m-1}^{TM,\infty}\Big)\frac{1}{\rho^2}\Big(e^{-jk_ms_1} - \frac{s_1}{r_1}e^{-jk_mr_1}\Big)$$
$$+ j\omega\mu_m\frac{IA}{4\pi}\Big(R_{m,m+1}^{TE,\infty} + R_{m,m+1}^{TM,\infty}\Big)\frac{1}{\rho^2}\Big(e^{-jk_ms_2} - \frac{s_2}{r_2}e^{-jk_mr_2}\Big)$$

$$F_M = F_M^D - j\omega\mu_m\frac{IA}{4\pi}\int_0^\infty J_1(k_\rho\rho)\frac{k_\rho^2}{jk_{mz}}\Big(F_{E_z}^{HMD} - R_{m,m-1}^{TM,\infty}e^{-jk_{mz}s_1} - R_{m,m+1}^{TM,\infty}e^{-jk_{mz}s_2}\Big)dk_\rho$$
$$- j\omega\mu_m\frac{IA}{4\pi}R_{m,m-1}^{TM,\infty}e^{-jk_mr_1}\Big(\frac{jk_m}{r_1} + \frac{1}{r_1^2}\Big)\sin\theta_1$$
$$- j\omega\mu_m\frac{IA}{4\pi}R_{m,m+1}^{TM,\infty}e^{-jk_mr_2}\Big(\frac{jk_m}{r_2} + \frac{1}{r_2^2}\Big)\sin\theta_2$$

$$G_M = G_M^D - \frac{IA}{4\pi}\int_0^\infty J_1(k_\rho\rho)k_\rho^2\Big(\frac{\dot{F}_{H_z}^{VMD}}{jk_{mz}} - R_{m,m-1}^{TE,\infty}e^{-jk_{mz}s_1} + R_{m,m+1}^{TE,\infty}e^{-jk_{mz}s_2}\Big)dk_\rho$$
$$- \frac{IA}{4\pi}R_{m,m-1}^{TE,\infty}e^{-jk_mr_1}\Big(-\frac{k_m^2}{r_1} + \frac{3jk_m}{r_1^2} + \frac{3}{r_1^3}\Big)\sin\theta_1\cos\theta_1$$
$$+ \frac{IA}{4\pi}R_{m,m+1}^{TE,\infty}e^{-jk_mr_2}\Big(-\frac{k_m^2}{r_2} + \frac{3jk_m}{r_2^2} + \frac{3}{r_2^3}\Big)\sin\theta_2\cos\theta_2$$

$$
\begin{aligned}
H_M = H_M^D &- \frac{IA}{4\pi}\int_0^\infty J_0(k_\rho\rho)k_\rho\Big(\frac{-k_\rho^2 F_{H_z}^{VMD}}{jk_{mz}} + jk_{mz}(R_{m,m-1}^{TE,\infty}e^{-jk_{mz}s_1} + R_{m,m+1}^{TE,\infty}e^{-jk_{mz}s_2})\Big)dk_\rho \\
&+ \frac{IA}{4\pi}\Big[R_{m,m-1}^{TE,\infty}\frac{\partial^2}{\partial s_1^2}\Big(\frac{e^{-jk_m r_1}}{r_1}\Big) + R_{m,m+1}^{TE,\infty}\frac{\partial^2}{\partial s_2^2}\Big(\frac{e^{-jk_m r_2}}{r_2}\Big)\Big]
\end{aligned}
$$

$$
\begin{aligned}
I_M = I_M^D &- j\omega\mu_m\frac{IA}{4\pi}\int_0^\infty J_1(k_\rho\rho)\frac{k_\rho^2}{jk_{mz}}\Big(F_{H_z}^{VMD} - R_{m,m-1}^{TE,\infty}e^{-jk_{mz}s_1} - R_{m,m+1}^{TE,\infty}e^{-jk_{mz}s_2}\Big)dk_\rho \\
&- j\omega\mu_m\frac{IA}{4\pi}R_{m,m-1}^{TE,\infty}e^{-jk_m r_1}\Big(\frac{jk_m}{r_1} + \frac{1}{r_1^2}\Big)\sin\theta_1 \\
&- j\omega\mu_m\frac{IA}{4\pi}R_{m,m+1}^{TE,\infty}e^{-jk_m r_2}\Big(\frac{jk_m}{r_2} + \frac{1}{r_2^2}\Big)\sin\theta_2
\end{aligned}
\tag{H.4}
$$

Bibliography

[1] R.F. Harrington, *Field Computations by Moment Methods*, New York: Macmillan, 1968.

[2] J. Jin, *The Finite Element Method in Electromagnetics*, New York: Wiley, 1993.

[3] K. Kunz and R. Luebber, *The Finite Difference Time Domain Method for Electromagnetics*, Boca Raton, FL: CRC Press, 1993.

[4] J.R. Mosig and F.E. Gardiol, "General integral equation formulation for microstrip antennas and scatterers," *IEE Proceedings*, vol. 132, pp. 424–432, Dec. 1985.

[5] L. Barlatey, J.R. Mosig, and T. Sphicopoulos, "Analysis of stacked microstrip patches with a mixed potential integral equation," *IEEE Trans. on Antennas and Propagation*, vol. 38, no. 5, pp. 608–615, May 1990.

[6] K.A. Michalski and D. Zheng, "Electromagnetic scattering and radiation by surfaces of arbitrary shape in layered media, Part I: Theory," *IEEE Trans. on Antennas and Propagation*, vol. 38, no. 3, pp. 335–344, Mar. 1990.

[7] P.N. Katehi and N.G. Alexopoulos, "Frequency-dependent characteristics of microstrip discontinuities in millimeter-wave integrated circuits," *IEEE Trans. on Microwave Theory and Techniques*, vol. MTT-33, no. 10, pp. 1029–1035, Oct. 1985.

[8] W.P. Harokopus and P.B. Katehi, "Characterization of microstrip discontinuities on multilayer dielectric substrates including radiation losses," *IEEE Trans. on Microwave Theory and Techniques*, vol. MTT-37, pp. 2058–2065, Dec. 1989.

[9] R. Jackson, "Full-wave finite element analysis of irregular microstrip discontinuities," *IEEE Trans. on Microwave Theory and Techniques*, vol. 37, pp. 81–89, Jan. 1989.

[10] J.R. Mosig, "Arbitrarily shaped microstrip structures and their analysis with a mixed potential integral equation," *IEEE Trans. on Microwave Theory and Techniques*, vol. 36, no. 2, pp. 314–323, Feb. 1988.

[11] S.M. Rao, D.R. Wilton, and A.W. Glisson, "Electromagnetic scattering by surfaces of arbitrary shape," *IEEE Trans. on Antennas and Propagation*, vol. AP-30, no. 3, pp. 409–418, May 1982.

[12] K.-L. Wu, J. Litva, R. Fralich, and C. Wu, "Full wave analysis of arbitrarily shaped line-fed microstrip antennas using triangular finite-element method," *IEE Proceedings-H*, vol. 138, no. 5, pp. 421–428, Oct. 1991.

[13] R. Kipp and C.H. Chan, "Triangular-domain basis functions for full-wave analysis of microstrip discontinuities," *IEEE Trans. on Microwave Theory and Techniques*, vol. 41, no. 6/7, pp. 1187–1194, June/July 1993.

[14] A. Sommerfeld, *Partial Differential Equations in Physics*, chapter VI, Academic Press, New York, 1949.

[15] L.B. Felsen and N. Marcuvitz, *Radiation and Scattering of Waves*, IEEE Press, 1994.

[16] J.R. Mosig and F.E. Gardiol, "Analytical and numerical techniques in the Green's function treatment of microstrip antennas and scatterers," *IEE Proceedings*, vol. 130. Pt. H, no. 2, pp. 175–182, Mar. 1983.

[17] K.A. Michalski and D. Zheng, "Electromagnetic scattering and radiation by surfaces of arbitrary shape in layered media, Part II: Implementation and results for contiguous half-spaces," *IEEE Trans. on Antennas and Propagation*, vol. 38, no. 3, pp. 345–352, Mar. 1990.

[18] W. Schwab and W. Menzel, "On the design of planar microwave components using multilayer structures," *IEEE Trans. on Microwave Theory and Techniques*, vol. 40, no. 1, pp. 67–72, Jan. 1992.

[19] S.B. Cohn, "Slot line on a dielectric substrate," *IEEE Trans. on Microwave Theory and Techniques*, vol. MTT-17, no. 10, pp. 768–778, Oct. 1969.

[20] B. Schüppert, "Microstrip/slotline transitions: Modeling and experimental investigation," *IEEE Trans. on Microwave Theory and Techniques*, vol. 36, no. 8, pp. 1272–1282, Aug. 1988.

[21] N.L. Van den Berg and P.B. Katehi, "Full-wave analysis of aperture coupled shielded microstrip lines," *IEEE MTT-S Dig.*, pp. 163–166, 1990.

[22] J. Sercu, N. Fach, F. Libbrecht, and P. Lagasse, "Mixed potential integral equation technique for hybrid microstrip-slotline multilayered circuits using a mixed rectangular-triangular mesh," *IEEE Trans. on Microwave Theory and Techniques*, vol. 43, no. 5, pp. 1162–1172, May 1995.

[23] W.C. Chew, *Waves and Fields in Inhomogeneous Media*, Van Nostrand Reinhold, New York, 1990.

[24] J.J. van Tonder, *Electromagnetic Radiation by Planar Antennas Buried in Layered Media*, PhD dissertation, University of Stellenbosch, 1995.

[25] J.J. van Tonder, "Electromagnetic field of HED/VED dipole located in layered medium," Tech. Rep. 1, Electromagnetic Software & Systems, Apr. 2000.

[26] A. Ishimaru, *Electromagnetic Wave Propagation, Radiation, and Scattering*, Prentice Hall, 1991.

[27] J.D. Jackson, *Classical Electrodynamics*, chapter 6, pp. 273–275, John Wiley & Sons, Inc., 1999.

[28] S. Ramo, J.R. Whinnery, and T. Van Duzer, *Fields and Waves in Communication Electronics*, John Wiley and Sons, Inc., 3rd edition, 1994.

[29] K.A. Michalski, "On the scalar potential of a point charge associated with a time-harmonic dipole in a layered medium," *IEEE Trans. on Antennas and Propagation*, vol. 35, no. 11, pp. 1299–1301, Nov. 1987.

[30] J.R. Mosig, *Integral Equation Technique*, Numerical Techniques for Microwave and Millimeter-Wave Passive Structures (T. Itoh, Ed), Chapter 3. John Wiley and Sons, 1989.

[31] R. Bunger and F. Arndt, "Efficient MPIE approach for the analysis of three-dimensional microstrip structures in layered media," *IEEE Trans. on Microwave Theory and Techniques*, vol. 45, no. 8, pp. 1141–1153, Aug. 1997.

[32] J.R. Mosig and F.E. Gardiol, "A dynamical radiation model for microstrip structures," *Advances in Electronics and Electron Physics, Academic Press*, vol. 59, pp. 139–237, 1982.

[33] J.R. Mosig, R.C. Hall, and F.E. Gardiol, *Numerical Analysis of Microstrip Patch Antennas*, Handbook of Microstrip Antennas (J.R. James and P.S. Hall, Eds), Chapter 8. Peter Peregrinus, 1989.

[34] K.A. Michalski, "Extrapolation methods for Sommerfeld integral tails," *IEEE Trans. on Antennas and Propagation*, vol. 46, no. 10, pp. 1405–1418, Oct. 1998.

[35] G.J. Burke and E.K. Miller, "Modeling antennas near to and penetrating a lossy interface," *IEEE Trans. on Antennas and Propagation*, vol. AP-32, no. 10, pp. 1040–1049, Oct. 1984.

[36] N. Kinayman and M.I. Aksun, "Efficient use of closed-form Green's functions for the analysis of planar geometries with vertical connections," *IEEE Trans. on Microwave Theory and Techniques*, vol. 45, no. 5, pp. 593–603, May 1997.

[37] C.F. du Toit, *The Computation of Electromagnetic Fields at Non-Asymptotic Distances from an Antenna using Cylindrical Near-Field Measurements*, PhD dissertation, University of Stellenbosch, 1992.

[38] D.R. Wilton, S.M. Rao, A.W. Glisson, D.H. Schaubert, O.M. Al-Bundak, and C.M. Butler, "Potential integrals for uniform and linear source distributions on polygonal and polyhedral domains," *IEEE Trans. on Antennas and Propagation*, vol. AP-32, no. 3, pp. 276–281, Mar. 1984.

[39] D.A. Dunavant, "High degree efficient symmetrical gaussian quadrature rules for the triangle," *International journal for numerical methods in engineering*, vol. 21, pp. 1129–1148, 1985.

[40] R.E. Hodges and Y. Rahmat-Samii, "The evaluation of MFIE integrals with the use of vector triangle basis functions," *Microwave and Optical Technology Letters*, vol. 14, no. 1, pp. 9–14, Jan. 1997.

[41] K. Umashankar, A. Taflove, and S.M. Rao, "Electromagnetic scattering by arbitrary shaped three-dimensional homogeneous lossy dielectric objects," *IEEE Trans. on Antennas and Propagation*, vol. AP-34, no. 6, pp. 758–766, June 1986.

[42] P.P. Silvester and R.L. Ferrari, *Finite elements for electrical engineers*, Cambridge University Press, 3rd edition, 1996.

[43] P.C. Hammer, O.P. Marlowe, and A.H. Stroud, "Numerical integration over simplexes and cones," *Math. Tables Aids Comp.*, vol. 10, no. 55, pp. 130–137, 1956.

[44] F. Alonso-Montferrer, A.A. Kishk, and A.W. Glisson, "Green's functions analysis of planar circuits in a two-layer grounded medium," *IEEE Trans. on Antennas and Propagation*, vol. 40, no. 6, pp. 690–696, June 1992.

[45] C.P. Hartwig, D. Masse, and R.A. Pucel, "Frequency dependent behavior of microstrip," *IEEE Group on Microwave Theory Tech. Microwave Symp. Dig.*, pp. 110–116, 1968.

[46] M. Davidovitz and Y.T. Lo, "Rigorous analysis of a circular patch antenna excited by a microstrip transmission line," *IEEE Trans. on Antennas and Propagation*, vol. 37, no. 8, pp. 949–958, Aug. 1989.

[47] R.K. Hoffmann, *Handbook of Microwave Integrated Circuits*, Artech House, 1987.

[48] G.J. Burke, E.K. Miller, and S. Chakrabarti, "Using model-based parameter estimation to increase the efficiency of computing electromagnetic transfer functions," *IEEE Trans. on Magnetics*, vol. 25, no. 4, pp. 2807–2809, July 1989.

[49] J. Chen, A.A. Kishk, and A.W. Glisson, "A 3D interpolation model for the calculation of the Sommerfeld integrals to analyze dielectric resonators in a multilayered medium," *Electromagnetics*, vol. 20, pp. 1–15, 2000.

[50] A. Papoulis, *Signal Analysis*, McGraw-Hill Book Company, 1977.

[51] I.P. Theron, "The accuracy of electromagnetic equivalence theorem models of microstip patch antennas," Study project presented in partial fulfillment of the requirements for the degree of Master of Engineering, University of Stellenbosch, 1991.

[52] D.M. Pozar, *Analysis and Design Considerations for Printed Phased-Array Antennas*, chapter 12, Handbook of Microstrip Antennas (J.R. James and P.S. Hall, Eds). Peter Peregrinus, 1989.